

**Spatially Resolved Equalization:
A New Concept in Intermodal Dispersion Compensation for
Multimode Fiber**

A Thesis
Presented to
The Academic Faculty

by

Ketan M. Patel

In Partial Fulfillment
of the Requirements for the Degree
Doctor of Philosophy

School of Electrical and Computer Engineering
Georgia Institute of Technology
July 2004

**Spatially Resolved Equalization:
A New Concept in Intermodal Dispersion Compensation for
Multimode Fiber**

Approved by:

Professor Stephen E. Ralph, Advisor
School Electrical and Computer Engineering

Professor Steven W. McLaughlin
School Electrical and Computer Engineering

Professor John A. Buck
School Electrical and Computer Engineering

Professor Joy Laskar
School Electrical and Computer Engineering

Professor Chandra Raman
School of Physics

Date Approved: 23 July 2004

ACKNOWLEDGEMENTS

The author would like to acknowledge contribution of several people, upon whose assistance much of this dissertation is dependent on. First, the student members of the Ultrafast Optical Communications Laboratory must be recognized: Brian R. Washburn, Todd Ulmer, Michael C. Gross, Jeffrey J. Lillie, J. Scott Rodgers, Marc Hanna, William Astar and Arup Polley. In addition to the years of merriment, these people have provided general insight and feedback with development of this work.

With regards to device fabrications, the author would like to greatly thanks Brian R. Washburn, Demetris Geddis, Sang-Woo Seo, Zhaoran Huang, Mikkel Thomas, Jeffrey J. Lillie, and Shannon M. Madison. These people directly contributed to the fabrication of the devices. Without their assistance, this author may still be in the cleanroom. Support from the staff at TriQuint Semiconductor is also acknowledged, in providing MMIC processing and prototype amplifiers as well as providing raw materials necessary for the receiver testing. The author would like to thank Eli Reese, Chuck Campbell, Steve Brown, and Lisa Howard for their assistance and expertise.

For moral support, much thanks goes to Kristen A. Nelson, upon whose encouragement and support the author was able to being this journey. Acknowledgement also goes to the support and inspiration of family and friends, including the parents of this author, Sarla M. Patel and Mukund R. Patel, Ph.D., both of whom have been excellent role models in life and career.

Finally, the author would like to thank Dr. Stephen E. Ralph. Besides the guidance and support for the work that is presented, Dr. Ralph has provided a foundation of critical thinking and a perspective on engineering research from which, hopefully, great works will come forth.

TABLE OF CONTENTS

ACKNOWLEDGEMENTS	iii
LIST OF TABLES	vii
LIST OF FIGURES	viii
SUMMARY	xiv
CHAPTER 1 INTRODUCTION	1
1.1 Motivation for the use of multimode fiber	3
1.2 Datacom standards	6
1.3 Problem statement	6
1.4 Thesis	10
1.5 Other art	13
1.5.1 Wireless RF multipath environment	13
1.5.2 Electronic equalization	15
1.5.3 Restricted mode launch	17
CHAPTER 2 THEORY AND NUMERICAL MODELLING	19
2.1 Implementation of theory	20
2.1.1 Wave propagation in the optical fiber	20
2.1.2 Modelling of the optical source	26
2.1.3 Modelling of the segmented photodetector	27
2.1.4 Modelling of the system link	28
2.1.5 Useful spatial diversity	34
2.2 Simulation results	36
2.2.1 Nominal fiber bandwidth	36
2.2.2 Equalized fiber bandwidth	37
2.2.3 Optimizing SRE	40
2.2.4 Advantage of the two-segment photodetection	42
2.2.5 Use of SRE in the near-field	43
2.2.6 Monte Carlo link simulations	43

2.2.7	Compatibility of SRE with other MMF design	47
2.2.8	Robustness of SRE over wavelength	51
2.2.9	Alignment tolerance of SRE	53
2.2.10	Equalization with restricted launch conditions	54
CHAPTER 3 CHARACTERISTICS OF FABRICATED DETECTORS		57
3.1	Basic photodetection	57
3.2	Characteristics of fabricated detectors	60
3.2.1	MSD biasing	62
3.2.2	MSD I-V curve	63
3.2.3	MSD device capacitance	63
3.2.4	MSD impulse response	65
3.3	Noise analysis	65
3.3.1	Shot noise	67
3.3.2	Relative intensity noise	67
3.3.3	Johnson noise	68
3.3.4	Modal noise	69
CHAPTER 4 EXPERIMENTAL RESULTS		77
4.1	Measurement of spatial diversity in MMF	77
4.2	Measurement of MMF link with equalization	80
4.2.1	Nominal MMF link bandwidth measurement	81
4.2.2	Verification of SRE detectors scalability	84
4.2.3	Enhanced MMF link at telecom wavelengths	86
4.2.4	Experimental verification of alignment tolerance	90
4.2.5	Measured equalization with restricted launch condition	90
4.3	Bandwidth improvement by SRE variations	93
4.3.1	Single-segment mode filtering	93
4.3.2	Mode retiming	94
4.4	Full SRE receiver test with transmitted data	95
4.4.1	Hybrid SRE receiver	95
4.4.2	Eye diagram measurements	95

4.4.3	Bit error rate measurements	98
CHAPTER 5	OTHER SRE RELATED WORK	103
5.1	DFE with spatially resolved equalization	103
5.2	Forward error correction	107
5.3	Improved diversity combining	109
5.4	Summary	110
CHAPTER 6	CONCLUSION	112
CHAPTER 7	SUGGESTED FUTURE WORK	114
7.1	Device fabrication	114
7.1.1	Improvements to bandwidth and quantum efficiency	114
7.1.2	Implementation of SRE with a <i>p-i-n</i> diode	115
7.2	Improved diversity combination	115
APPENDIX A	— FINITE DIFFERENCE METHOD FOR MODE SOLVING	117
APPENDIX B	— SIMULATION CODE	119
APPENDIX C	— FABRICATION PROCEDURE	127
VITA	135

LIST OF TABLES

Table 1.1	Digitized video requirements [10].	4
Table 1.2	Datacom standards on requirements for operating distances and power budget with MMF.	7
Table 1.3	Types of fibers typical bandwidths.	8
Table 2.1	Parameters of standard graded-index multimode fiber [49].	33
Table 2.2	Statistics of simulated VCSEL parameters.	44

LIST OF FIGURES

Figure 1.1	Network topology for high-speed connectivity and distribution of network services. Data rate in customer network ranges from 100 Mb/s to 10 Gb/s.	4
Figure 1.2	(a) Raytrace pictorial of step-index multimode fiber. (b) Raytrace pictorial of graded-index multimode fiber.	8
Figure 1.3	Pulse broadening in 50- μm MMF due to differential modal delay only. As a function of radius r , refractive index in fiber core follows r^α [8].	9
Figure 1.4	Multimode optical fiber cable survey conducted by IEEE802.3ae cabling survey ad hoc group in June 1999. [14].	9
Figure 1.5	Two segment photodetector used with graded-index multimode fiber. Spatial diversity is exploited to enhance fiber link bandwidth.	11
Figure 1.6	In this simplified representation, cancellation of ISI energy in high-ordered modes by sampling with annular PD and subtracting from inner PD. The remaining signal is primarily of low-ordered modes.	11
Figure 1.7	Exploiting spatial diversity in wireless RF links.	14
Figure 1.8	Spectrum of multipath fading with respect to the frequency band of interest for both optical and RF links.	14
Figure 1.9	Spectrum of bandwidth limited channel with and without equalization.	16
Figure 1.10	Block diagram of electronic equalizer. Decision feedback equalization implemented with threshold device at output for signal adder. Copies of the signal, delayed by an integer multiple of the data rate $1/\tau$, are combined with optimized scaling a_n and b_m	16
Figure 1.11	Restricted mode launch for minimizing the excitation of fiber modes [34].	18
Figure 2.1	Flow diagram for numerical modelling of multimode fiber link.	21
Figure 2.2	Index profile of graded-index profile for communication links. Parabolic index $n(r) \propto r^\alpha$, where $\alpha \approx 2$	23
Figure 2.3	Profile dispersion of 13.5% GeO ₂ -doped fused-silica multimode fiber [41].	25
Figure 2.4	Use of concentric, multisegment photodetection to exploit spatial diversity of optical modes.	27
Figure 2.5	Computed radial profile of diffracted mode-field profile $ R(r) $ for 50- μm graded-index MMF.	29

Figure 2.6	(a) System model of back-to-back optical link using square-law transmitter and receiver. (b) System model of fiber link with conventional photodetection.	30
Figure 2.7	System model MMF link model, with spatially resolved equalization.	31
Figure 2.8	Circuit model of parallel PD segment with opposite polarity.	32
Figure 2.9	(a) Radial mode profile computed of mode LP_{24} in $50\text{-}\mu\text{m}$ GI-MMF. Inset plot shows full irradiance profile. (b) Computed encircled-flux.	35
Figure 2.10	(a) group delay and 50% encircled-flux radius for fiber modes at 850 nm, in a $50\text{-}\mu\text{m}$ core MMF. (b) Correlation plot between group delay and encircled-flux	35
Figure 2.11	In this simplified representation, cancellation of ISI energy in high-ordered modes by sampling with annular PD and subtracting from inner PD. The remaining signal is primarily of low-ordered modes.	36
Figure 2.12	Relative modal power a $50\text{-}\mu\text{m}$ graded-index multimode fiber illuminated by a 5-mode, 850-nm VCSEL source. (a) Sorted according to mode number m . (b) Sorted according to relative group delay.	37
Figure 2.13	(a) Fiber impulse response with VCSEL-like optical source. (b) Frequency response.	38
Figure 2.14	(a) Impulse response of equalized MMF link with $55\text{-}\mu\text{m}$ MSD. (b) Frequency response in comparison to non-equalized MMF.	38
Figure 2.15	External quantum efficiency of fiber modes versus relative group delay for (a) inner PD and (b) outer PD.	39
Figure 2.16	Representative of two modes (meridional and azimuthal modes) with near identical group delay and HWHM_{EF} , but disparate encircled-flux $\text{EF}(r)$	39
Figure 2.17	(a) Bandwidth gain versus radius of MSD placed at $400\ \mu\text{m}$ from fiber output. (b) Bandwidth gain versus fiber-MSD gap for $55\text{-}\mu\text{m}$ MSD.	41
Figure 2.18	(a) Improvement in MMF bandwidth with SRE versus optical loss (in Watts/Watts). (b) Frequency domain response of equalized link for MSD at various distances from fiber: 300, 400 and $500\ \mu\text{m}$	41
Figure 2.19	Comparison of bandwidth gain with high-ordered mode suppression due to partial detection (Inner PD) versus SRE with subtraction of the outer PD photocurrent (Full SRE). (a) Measured bandwidth gain versus MSD radius. (b) Correlation between optical SNR penalty and bandwidth gain.	42
Figure 2.20	Use of multisegment PD in near-field with $15\text{-}\mu\text{m}$ MSD.	43
Figure 2.21	Histogram of fiber bandwidth with varying optical launch condition (5000 trials). Launch condition influenced by varying tilt and transverse position of VCSEL relative to MMF.	45

Figure 2.22	Histogram of link bandwidth with spatially resolved equalization.	45
Figure 2.23	Histogram of optical penalty with spatially resolved equalization.	46
Figure 2.24	Correlation between optical penalty and equalized fiber bandwidth.	46
Figure 2.25	(a) Impulse response of 62.5- μm core MMF, with VCSEL-like optical source. (b) Frequency response.	48
Figure 2.26	(a) Impulse response of equalized 62.5- μm MMF. (b) Frequency response.	48
Figure 2.27	(a) Mode-field size in the near-field versus modal group delay for step-index fiber modes. (b) Mode-field size in far-field.	49
Figure 2.28	(a) Equalization gain for various α profiles. (b) Inherent fiber bandwidth with conventional detection.	50
Figure 2.29	Modal group delay for fiber near optimal core profile. Mode number is normalized to total mode number. group delay is normalized by maximum relative delay.	50
Figure 2.30	Mode-field size in the far-field—400 μm from fiber—for 1550-nm propagation in 50- μm MMF.	52
Figure 2.31	Frequency response of MMF equalized with 55- μm MSD in the far-field. Wave propagation at 1550 nm.	52
Figure 2.32	(a) Bandwidth gain and (b) optical power penalty of equalized fiber with transverse offset between fiber axis and 55- μm MSD.	53
Figure 2.33	Bandwidth gain by SRE for various launch conditions: Gaussian source illumination with uniform phase front. Bandwidth compared on a launch-by-launch basis.	55
Figure 2.34	Bandwidth gain by SRE for various launch conditions: Gaussian source illumination with uniform phase front. Bandwidth gain compare to standard multimode VCSEL launch.	55
Figure 3.1	Epitaxial $p-i-n$ photodiode structure.	58
Figure 3.2	Planar MSM photodiode structure.	58
Figure 3.3	InGaAs material system used for high-speed MSM photodetector. Photon absorption in 1- μm InGaAs layer. [51]	60
Figure 3.4	Microphotograph of fabricated multisegment detector	61
Figure 3.5	On-wafer biasing and probing using 50- Ω RF probes	61
Figure 3.6	Biasing of MSD device. (a) Bias of equal magnitude and polarity applied to MSM for conventional PD. (b) Bias of equal magnitude but opposite polarity applied to MSM to subtract outer PD photocurrent from that of the inner PD. (c) Required PD configuration and bias for SRE with $p-i-n$ diodes.	62

Figure 3.7	Current-voltage transfer curve of interdigitated MSM under various illumination power.	64
Figure 3.8	Device reactance computed from measured 1-port scattering parameter.	64
Figure 3.9	Measured impulse response and computed frequency response of 200- μm MSD at with 1-ps at 1550-nm. Main peak width of 35-ps, low-frequency tail width of 400 ps.	65
Figure 3.10	Circuit model for noise injected, either optically or electronically, prior to signal recombination.	66
Figure 3.11	Optical spectrum of DFB laser (Agilent 83430A) and computed autocorrelation envelope. Spectrum limited by finite resolution (0.01nm) optical spectrum analyzer. Underlying carrier oscillation in autocorrelation not shown.	73
Figure 3.12	Optical spectrum of FP (Agilent 8155A) laser and computed autocorrelation envelope. Underlying carrier oscillation in autocorrelation not shown.	74
Figure 3.13	Optical spectrum of VCSEL (E2O 10GHz module, EM1052) laser and computed autocorrelation envelope. Underlying carrier oscillation in autocorrelation not shown.	74
Figure 3.14	Speckle pattern of optical signal from 1.1-km fiber sample with various launch sources: (a) LED @ 850 nm, (b) DFB laser @ 1550 nm, (c) Fabry-Perot laser @ 1550 nm, (d) VCSEL @ 850 nm.	76
Figure 4.1	Measurement apparatus for spatial diversity measurement. Optical spot is spatially filtered with a 15- μm pin-hole placed in optical beam. Light transmitted through the pin-hole is received by high-speed photodetector through a 100- μm step-index MMF of high numerical aperture.	78
Figure 4.2	50- μm , high-NA, step-index fiber mode-scrambler. SI-MMF is meandered around 5-mm radius posts spaced with 10-mm pitch.	79
Figure 4.3	Diversity along optical spot diameter. Impulse response of 1.1-km, 50- μm core, graded-index multimode fiber, excited with a 1-ps, 1550-nm optical pulse launched through a mode scrambler.	80
Figure 4.4	Experimental apparatus for measurement of MMF link performance by impulse response measurement.	82
Figure 4.5	Probe station used for MSD-fiber alignment and on-wafer impulse response measurement.	82
Figure 4.6	(a) Impulse response of 1.1-km, 50- μm MMF with 10-ps optical pulse excitation at 810-nm with and without equalization via a 55- μm MSD, 415 μm from the fiber output. (b) Measured impulse response observed by inner and outer PD, $h_{inr}(t)$ and $h_{otr}(t)$ respectively.	83
Figure 4.7	Frequency response computed from measured impulse response of fiber link with and without SRE.	83

Figure 4.8	Impulse response of 1.1-km, 50- μm MMF link with MSD of various radii.	85
Figure 4.9	Correlation plot between optical penalty and bandwidth gain due to SRE for a sample of 1.1-km, 50- μm MMF with spatially resolved equalization via MSD of various sizes.	85
Figure 4.10	(a) Impulse response of 1.1-km, 50- μm MMF at 1550-nm. A 55- μm MSD is at 400- μm from fiber output. (b) Frequency response computed from measurement.	86
Figure 4.11	(a) Bandwidth gain versus optical loss via SRE enhancement for a 9 samples of 1.1-km, 50- μm core MMF tested at 1550-nm with 55- μm MSD at 400 μm from fiber. (b) Measured BW gain of 9 samples of 62.5- μm core MMF with 55- μm MSD 310 μm from fiber output. . . .	87
Figure 4.12	(a) Bandwidth gain versus optical loss via SRE enhancement for a 9 samples of 1.1-km, 50- μm core MMF tested at 1550-nm. Identical MSD configuration with no fiber specific optimization.	87
Figure 4.13	Measured link bandwidth gain and loss for 9 samples of 1.1-km, 50- μm MMF at 1550 nm. Measurements made with MSD at various distances from flat-cleaved fiber facet.	88
Figure 4.14	Correlation plot between optical penalty and bandwidth gain for 9 samples of 1.1-km, 50- μm MMF, measured at 1550-nm. $\langle\rho_{BW,loss}\rangle$ is the average of the correlation coefficient of individual curves; $\rho_{BW,loss}$ is the correlation coefficient of the average curve.	88
Figure 4.15	Bandwidth gain versus transverse misalignment	90
Figure 4.16	Method of controlling launch condition.	91
Figure 4.17	Enhancement of fiber bandwidth compared to standard detection for given launch condition.	92
Figure 4.18	Enhancement of fiber bandwidth compared to standard detection with overfill launch condition (worst-case bandwidth).	92
Figure 4.19	Comparison of bandwidth gain with high-ordered mode suppression with subtraction of the outer PD photocurrent (Full SRE) versus partial detection of optical power with a small PD segment (Inner PD). (a) Bandwidth gain versus fiber-PD gap.(b) Correlation between optical SNR penalty and bandwidth gain.	94
Figure 4.20	Computed bandwidth gain by addition of the two-segment photocurrents with adjustment of group delay for outer PD signal.	95
Figure 4.21	Fabricated hybrid SRE receiver with transimpedance pre-amplifier . .	96
Figure 4.22	Eye diagram for 50- μm core, 1.1-km MMF link. FP laser, externally modulated FP laser at 1.25 Gb/s is coupled into fiber via step-index mode-scrambler(a) and (b) Measured eye diagram without and with SRE respectively. (c) and (d) Simulated eye diagram without and with SRE respectively, using measured impulse response of fiber	97

Figure 4.23	Eye diagram for 50- μm core, 1.1-km MMF link. Directly modulated VCSEL laser at 1.25 Gb/s coupled directly into MMF. Measured eye diagram (a) without and (b) with SRE.	97
Figure 4.24	(a) Block diagram of SRE receiver with 1-GHz noise filter and limiting amplifier. (b) Output eye diagram of back-to-back (no fiber) link.	99
Figure 4.25	Measured bit error rate of four link configurations: two tests with the 1.1-km MMF and two without(back-to-back). For each link condition, two states of equalization: with and without equalization by SRE. Simulated BER experiments on the equalized channel are also plotted. Noise limit curve is the minimum achievable BER over ideal channel.	99
Figure 4.26	Impulse response of SRE receiver with 1-GHz noise filter.	101
Figure 4.27	Spurious RF signal measured at the output of SRE receiver.	101
Figure 5.1	Correlation between minimum DFE taps and channel bandwidth.	105
Figure 5.2	BER versus optical SNR at 2.5 Gb/s with different equalization [72].	105
Figure 5.3	ISI penalty versus number of DFE taps (forward taps NF, and backward tap NB) for three samples of 300-m MMF [73].	106
Figure 5.4	BER vs. optical SNR at 1.25 Gb/s (STAND denotes standard detection) [74].	108
Figure 5.5	Required receiver sensitivity for 10^{-9} BER [74].	108
Figure 5.6	Block diagram of Viterbi-optimized, MSD-enhanced MMF link. [75]	111
Figure 5.7	Bit error rate versus electrical SNR for various receiver configurations. [75]	111
Figure C.1	Spatially resolved equalization MSM mask layout pattern. All structure on a single metal layer.	128

SUMMARY

The use of optical fiber is of great interest in developing extensive, high-speed networking infrastructures. Optical fiber provide many advantages over traditional copper cables and wireless links. Among these advantages are high security, low electromagnetic interference, extremely low loss, very high bandwidths, and highly manageable cabling. However, the very small wavelengths associated with optical radiation requires very small waveguide dimensions. Waveguide dimension of single mode fiber (SMF) are $< 10\mu m$, resulting in relatively poor yield in device manufacturing. For residential and other last-mile networks topologies, cost constraints limit the appeal of SMF. Large core fibers allow for less restrictive manufacturing tolerances; however, they also results in multimode propagation that exhibit distortion from the dispersion in propagation among the many modes. The distortion can be prohibitively large for data rates approaching and exceeding 1 Gb/s.

To improve the deployability of these multimode fibers (MMF), a method of dispersion compensation that maintains the ease-of-use characteristic of MMF is required. This dissertation demonstrates an opto-electronic method of dispersion compensation, *i.e.* spatially resolved equalization, by the use of a multisegment photodetector. It is shown the modes of the fiber can be separated, such that when the individual photodetector signals are combined, the resulting temporal response of the fiber link is improved from that of a conventional fiber link. This method is extremely robust to system variation and is independent of data rate and transmission format, allowing it to be employed in a wide variety of optical links. More importantly, the implementation demonstrated in this dissertation is comparable, in simplicity and alignment tolerance, to a conventional photodetector. System performance is shown using both temporal and frequency response as well as real bit error rate and eye diagram measurements.

CHAPTER 1

INTRODUCTION

“If you build it, they will come.”

— “Shoeless” Joe Jackson in *Field of Dreams* by W.P. Kinsella

The use of optical waveguides has a history far longer than what is suggested by its widespread in the late part of the 20th century. As far back as the mid 1840s, the common public was entertained with the display of light guided in fountains of water. Jacques Babinet demonstrate the rudimentary of light guided by glass but for the next century, the practical use of optical fiber was limited to illumination and remote viewing. It wasn't until the convergence of semiconductor technology and improved fiber glass manufacturing, in the late 1960s, that the optical waveguide could be exploited for ultra high-speed communications, exceeding 1 terabits per second. And not until the deployment of optical fiber, was there a need for such bandwidths.

At the beginning of the 1970s, the potential of optical fiber was just becoming realizable. Optical losses in the fiber started to approach a few dB per kilometer, compared to thousands of dB/km previously achieved. But packaging and laser technology was limited. The potential of singlemode fiber (SMF) was well understood, but so were the difficulties in its use. The narrow core of SMF required the use a laser source over a simple light emitting diode. Semiconductor laser diodes were invented in the 1962, but their reliability was still in question. Moreover, laser diodes were limited to $<850\text{-nm}$ meaning SMF were restricted to only a few microns in diameter. Not only would manufacturing long lengths of fiber be difficult, but so would coupling light into them. Multimode fiber (MMF) was much easier to work with, especially since light emitting diodes (LED) were assumed to

be the transmitter of choice for its perceived reliability; fiber core sizes up to 100- μm was thought to be required. However, the multipath environment of MMF meant signal distortion from the disparate group velocity among the fiber modes. As early as the mid 1960s, engineers at Bell Telephone Laboratories had started to consider multimode propagation in dielectric waveguide [1]–[6]. Even before mastery over fiber losses was achieved, it was well understood that graded-index core profile could be used to minimize intermodal dispersion [7], [8]. Of course, performance of singlemode fiber would still be better, but cost and reliability considerations made it impractical. Moreover, envisioned optical networks would cover urban and suburban areas: a few kilometers in lengths daisy-chained together, with a multiple channels aggregated up to 100s of Mb/s. Each channel was expected to use tens of kHz, the bandwidth of a single voice channel.

By the late 1970s, however, significant advances, namely improved lifetime and new wavelengths, in laser diode obviated the need for multimode fiber. With development of 1550-nm laser, the core diameter of SMF would approach a more manageable 10 μm . Equally important, fiber losses as low as 0.16 dB/km were discovered at 1550 nm. A single fiber link would now be able to connect larger network hubs, separated by longer distance, allowing a single fiber to service 100s thousands of customers. With less optical terminations per user, the overhead in time and cost of aligning fiber to opto-electronic components was less critical since the cost could be shared by more users. By the mid 1990s, the push in optical networking was to connect major urban centers with enormous amounts of bandwidth through singlemode fiber. The core and access networks would be linked by SMF, while the last mile and customer premise networks would remain copper-based, *i.e.* twisted-pair and coaxial cables. Meanwhile, servers within local area networks (LAN) would be linked with graded-index fiber but was installed to support 155 Mb/s data rates with the use of LED.

1.1 Motivation for the use of multimode fiber

Recent advances in computer hardware and software allow for new and advanced networking service for both productivity and entertainment. Improvements in the microprocessor allow more and more media, once relegated to processing by hardware, to be digitized and processed by software with ease. The bandwidth of a single channel has increased by as much as 4 order-of-magnitude since the early 1970s. And as this progresses, new services, with even high bandwidth needs, will be offered; currently, desktop computers are capable of networking at 1 Gb/s. New network appliances, such as telephones and televisions, will be added to the same data infrastructure. Already voice over Internet Protocol (VoIP) and video on demand (VOD) are being offered to consumers, over a single data network, obviating the need for application specific networks, such as cable TV or telephone. But these communication solutions will require high quality-of-service (QoS) that comes only with increase network capacity.

While the technology exists to provide these services, its deployment is limited by the low bandwidth last-mile network. As a result, much of the ultra high-capacity fiber links between major urban center lay unused [9]. There remains a significant bottle neck in delivering the bandwidth to the consumer. As of the mid 2000s, the last-mile customer networks have burst rates of 1 Mb/s and of 100s kb/s data rate. While this is adequate for buffered media, full-duplex, video and voice streams require much greater throughput, Table 1.1. Even with video compression—around 70:1 for high-quality MPEG2—an average data rate of 20 Mb/s must be maintained for the latest in high-definition digital video stream. The need for high QoS, multimedia services will easily absorb the capacity of today's data, residential and access network infrastructure. Burst rates exceeding 100 Mb/s, approaching 1 Gb/s, will be required, shown in Fig. 1.1.

Equally as important as the need of residential networks are those of local area network (LAN) and storage area networks (SAN). With improvement in digitized media, growths in data storage is expected: medical records, financial market, news, weather, government records, etc. New microprocessor capabilities will push the boundaries of parallel computing: simulation of weather patterns, biological and chemical processes, traffic, artificial

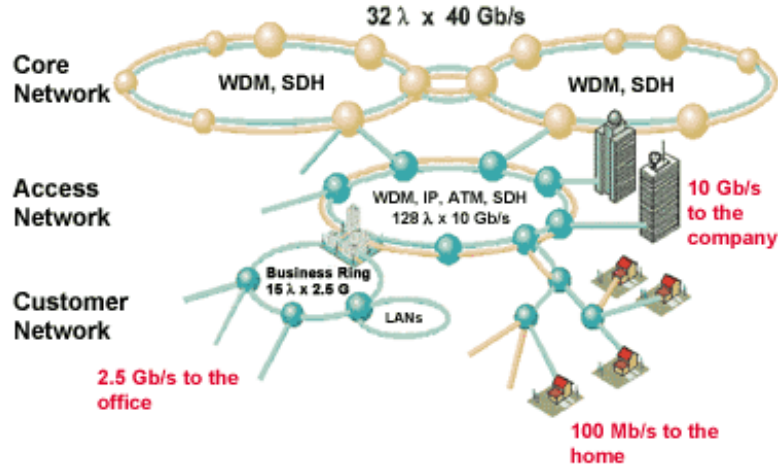


Figure 1.1: Network topology for high-speed connectivity and distribution of network services. Data rate in customer network ranges from 100 Mb/s to 10 Gb/s.

intelligence, complex behavior, etc. Problems of limited real estate in already cramped server rooms can be solved only with aggregation of streams onto links of higher and higher data rates. Within a LAN, backbone are connecting workgroup switches with 100 Mb/s and 1 Gb/s interfaces; similarly, 10 Gb/s links serves as an aggregator for connecting to and from server farms. These require high speed networking solution over a wide range of distances 100–1000 m and must be deployable in large volumes with little or not specialized labor.

At such data rates, standard copper coaxial cables exhibit extremely high losses, 15–20 dB per 100 meter. Singlemode fiber has the both the bandwidth and low-loss, but

Table 1.1: Digitized video requirements [10].

Format	Raw data rate (Mb/s)
NTSC	143.18
PAL (4 fsc)	177
SMPTE 259M	270
CCIR656	270
EU95 (HDTV)	1440
SMPTE 292M (HDTV)	1485

provide such performance with at prices exceeding \$1000 for optoelectronic (OE) units, due to the high level of labor involved. This can be can be exhortibant for residential and LAN networks where the user not only bears a significant burden of ownership, but in many cases, also installs such hardware without the benefit of training. To bring optical networking to mass market, cost-effectiveness and simplicity must be of the highest priority. Typical price points for high-volume, last-mile network hardware are <\$200, [11]. Consider that in other consumer electronics market costs are measured in pennies. To that end, there has been a significant resurgence towards MMF networks because of its low-alignment tolerance and ease-of-use.

In addition to its alignment tolerance, recent development of vertical-cavity surface-emitting lasers (VCSEL) have made MMF important. Compared to the edge-emitting laser, VCSELs have improved manufacturablity [12], [13]. The surface-normal emission of VCSELs allow the fabrication and testing of lasers to be performed completely on-wafer. In turn, this leads to not only to reduction in time and cost of device testing, but also reduced waste in packaging of bad lasers. Other factors such as lower power dissipation and improved reliability over edge-emitting lasers make VCSELs highly cost-effective. Yet today's VCSELs are still restricted in emission quality. Many commercial VCSELs lase with 5–10 transverse cavity modes. As was the case with LED, power coupling to SMF can be extremely difficult. However, by virtue of its plurality of modes, MMF is well-suited for efficient coupling of VCSEL emission.

The synergy of low-cost manufacturing, high product yield of VCSEL and the ease-of-use of MMF will play a significant role in removing the communications bottleneck that exists between the high-speed optical network infrastructure and the consumer premises. Such high-capacity networks will be the enabler for services yet to be conceived and even greater demand for bandwidth.

1.2 Datacom standards

The development of standards is crucial to the adoption of a new performance point. Thus, the recent ratification of the 10 Gigabit Ethernet standards (10GbE) is a key step forward in the implementation of 10 Gb/s fiber optic technology. A 10Gb/s Fibre Channel (ANSI) standards proposal is also in the process of ratification. The 10GbE is designed to facilitate communication all the way from the LAN to the metropolitan area network (MAN) and even the wide area network (WAN). The use of 10GbE will allow seamless interoperability. Links based upon standard MMF of the type currently within the installed base are specified for distances up to 65 meters. Newer, higher bandwidth MMF will support 10G data rates over distances up to 300 meters, which covers the vast majority of distances found within a LAN or SAN, Table 1.2.

Another factor expected to drive enterprise level network bandwidths to the 10Gb/s level is the rapid adoption of on-motherboard, Gigabit Ethernet transceivers in personal computers. Desktop computers are already being shipped with 10/100/1000Base T-ports. As users begin to take advantage of these data rates, the need for higher speed connections within the network will become apparent. With the release of the standard, products supporting 10 Gb/s are appearing more frequently. Twenty-four companies collaborated at the SUPERCMM conference in Atlanta, Georgia in June 2002 to demonstrate the interoperability of multiple 10G Ethernet components and systems in various configurations.

1.3 Problem statement

While the plurality of modes in MMF eases requirement on optoelectronic components and fiber alignment, it also leads to distortion of the transmitted signal. The guided-modes of MMF exhibit unique group velocity. In stepped-index multimode fiber (SI-MMF), modes of increasing order (*i.e.* complexity in transverse mode profile) also propagates along an increased path length. In a homogenous medium, signal transmitted along more the high-ordered modes (HOM) will have a longer effective path length and will arrive at the fiber output significantly later than signal in low-ordered modes (LOM). This intermodal

Table 1.2: Datacom standards on requirements for operating distances and power budget with MMF.

Protocol	Operating Distance		
	50 μm	62.5 μm	Power Budget
Gigabit Ethernet			
serial @ 850 nm	550	275	4.9
serial @ 1300 nm	550	550	5.1
1G Fibre Channel			
serial @ 850 nm	550	275	5.1
serial @ 1300 nm	550	550	4.9
2G Fibre Channel			
serial @ 850 nm	250	250	5.1
serial @ 1300 nm	250	250	4.7
4G Fibre Channel			
serial @ 850 nm	150	150	5.1
serial @ 1300 nm	150	150	4.7
0 Gigabit Ethernet			
serial @ 850 nm	33	82	5
4 \times @ 1300 nm	300	300	5.5
10G Fibre Channel			
4 \times @ 850nm	550	120	5.1
4 \times @ 1300nm	300	300	5.1
serial @ 850nm	300	33	4.7

dispersion, or differential modal delay (DMD), can cause severe intersymbol interference (ISI), shown in Fig. 1.2. The core of graded-index multimode fiber (GI-MMF), however, is designed to minimize this DMD among modes. Besides exhibiting a shorter path length than HOM, LOM are confined to smaller regions, near the center of the fiber core; as a results, LOM experience a higher refractive index, Fig. 1.2b. A properly designed core profile achieves a balance in effective path-length and group velocity, reducing the intermodal dispersion by orders-of-magnitude, shown in Fig. 1.3. Despite the improved design feature of GI-MMF, manufacturing limitations restrict fiber bandwidths. Performance of typical GI-MMF is summarized in Table 1.3.

With the upgrading of LAN from 155 Mb/s to 10 Gb/s, the installed-base of multimode fiber no long satisfies the current needs of information technology. The worst-case bandwidth of 99% of the installed optical infrastructure is <1 GHz, Fig. 1.4. While, improvement

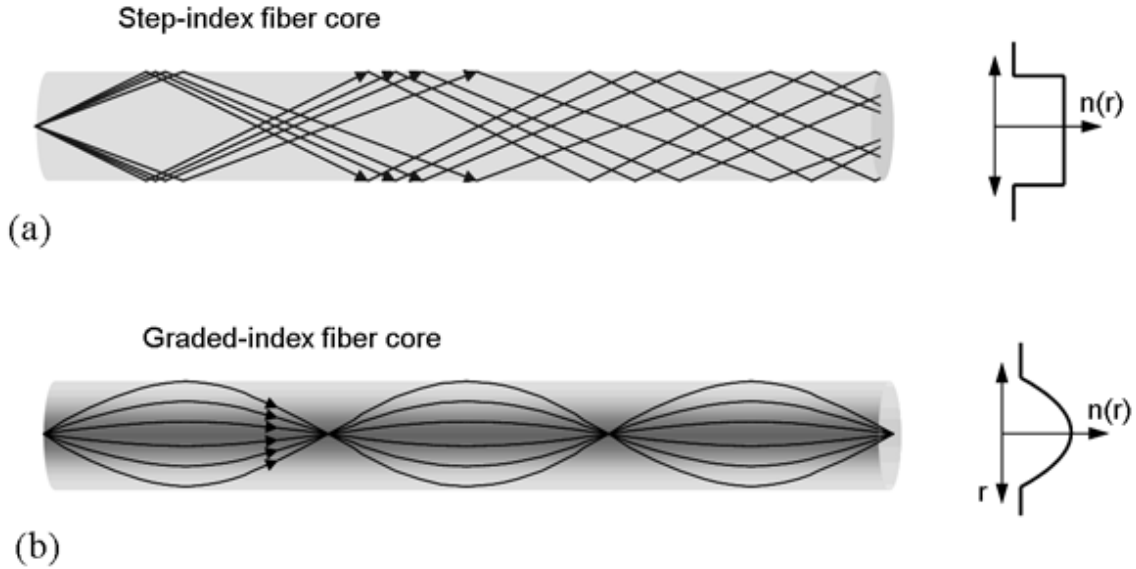


Figure 1.2: (a) Raytrace pictorial of step-index multimode fiber. (b) Raytrace pictorial of graded-index multimode fiber.

in manufacturing are allowing newer fibers to support the capacity demands, it is the cost of labor that dominates. To minimize overall cost, a number of solutions are being considered to “push” 10 Gb/s signal through the installed-MMF infrastructure rather than replace the fiber.

Even still, optimized fibers like OFS’s Lazerwave and Corning Infinicore that have 2–3× better bandwidth than the older MMF but are designed specifically for use at 850 nm. As data rates increase, so does spectral content and the effects of chromatic dispersion; future

Table 1.3: Types of fibers typical bandwidths.

Core/Cladding	Bandwidth	Applications/Notes
<i>Multimode Graded-Index</i>		<i>@850/1300 nm</i>
50/125 μm	500/500 MHz-km	Laser-rated for GbE LANs
50/125 μm	2000/500 MHz-km	Optimized for 850 nm VCSELs
62.5/125 μm	160/500 MHz-km	Most common LAN fiber
100/140 μm	150/300 MHz-km	Obsolete
<i>Singlemode</i>		<i>@1310/1550 nm</i>
8-9/125 μm	100 Terahertz	Telco/CATV/long high speed LANs

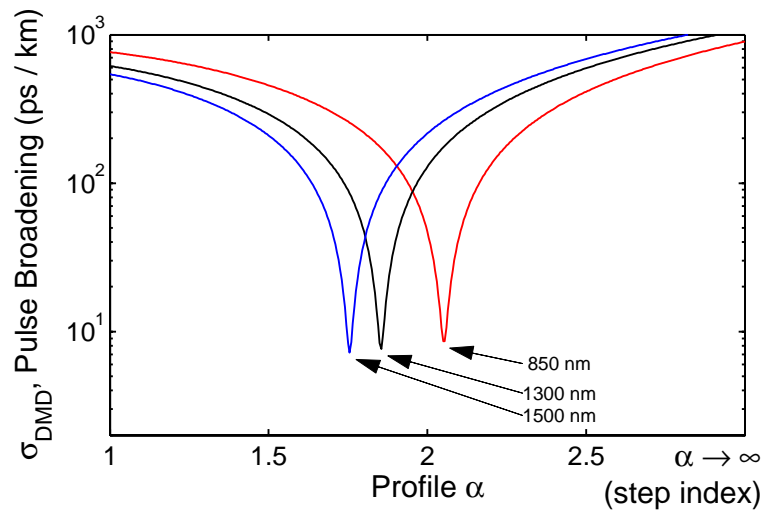


Figure 1.3: Pulse broadening in 50- μm MMF due to differential modal delay only. As a function of radius r , refractive index in fiber core follows r^α [8].

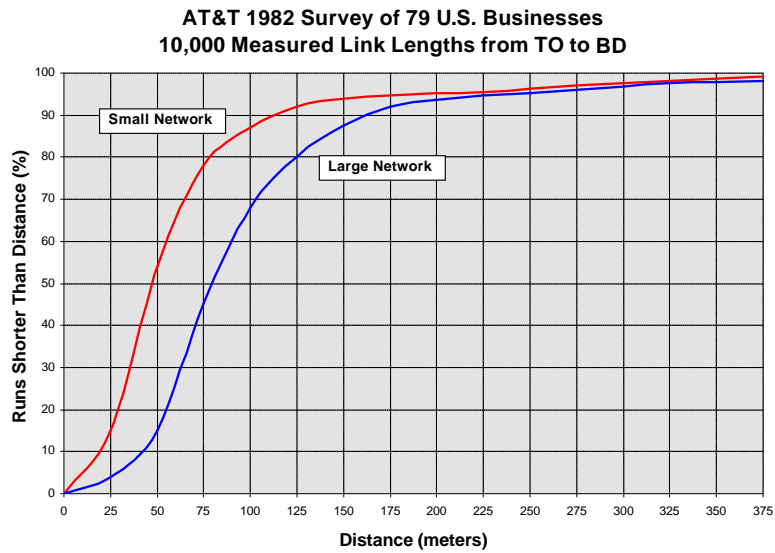


Figure 1.4: Multimode optical fiber cable survey conducted by IEEE802.3ae cabling survey ad hoc group in June 1999. [14].

implementation of MMF networks will move to 1300 and 1550 nm wavelength. Moreover, considering the opportunities of fabricating more inexpensive VCSELs at other wavelengths such as 630 or 980 nm, the optimization of multimode fiber bandwidth does not necessarily future-proof the network for all applications [15].

It is a matter of history that seemingly infinite supplies will eventually be exhausted. Whether it is new or old fiber, it is inevitable that the demands placed on multimode fiber will grow, whether for longer spans, higher data rates or newer wavelength. Indeed, even as solutions are being sought for exceeding MMF capacity at 10 Gb/s, transmission at 40 Gb/s over the same fiber is being considered. Regardless, as long as multimode fiber maintains its cost effectiveness over SMF, there will be a need to mitigate the effects of intermodal dispersion. But it is not by bandwidth that the solutions will be judged, but rather by the cost and complexity.

1.4 Thesis

A method of photodetection for compensation of differential modal delay with segmented photodetector is proposed. There exists, at in the output signal of the graded-index multimode fiber, a spatial diversity that can be easily exploited by a multisegment photodetector (MSD). Whereas a conventional photodetector blindly combines the emitted optical power in all fiber modes into a single electrical signal, the MSD can be used to separate the optical signal into groups of modes. Though this separation is not orthogonal, fundamentally the multisegment photodetector provides more information about the transmitted signal than permitted with a conventional photodetector. This information can be used to gain some knowledge of the intermodal dispersion and to compensate for ISI in a simple manner without limitation to data rate or transmission format.

More specifically, a two segment photodetector (PD) is used to detect the optical signal, shown in Fig. 1.5. Since the fiber modes exhibit differing size as well as group velocity, the emitted optical signal will experience a diversity in the temporal response in the signal across the optical beam. A concentric arrangement of photodetector is used to exploit

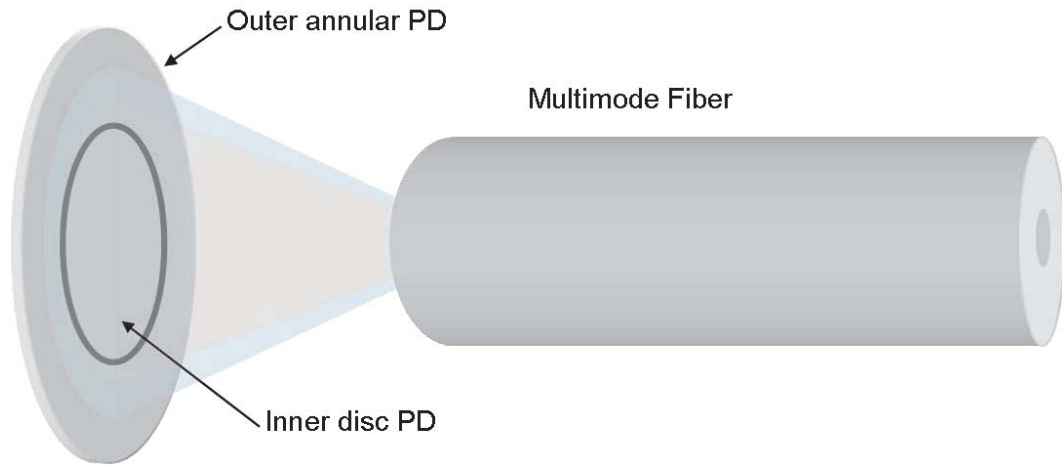


Figure 1.5: Two segment photodetector used with graded-index multimode fiber. Spatial diversity is exploited to enhance fiber link bandwidth.

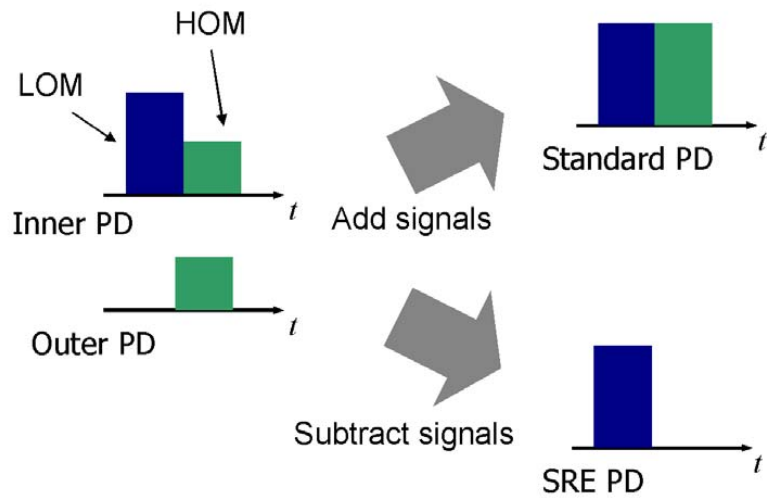


Figure 1.6: In this simplified representation, cancellation of ISI energy in high-ordered modes by sampling with annular PD and subtracting from inner PD. The remaining signal is primarily of low-ordered modes.

this *a priori* knowledge. With two PD segments, a circular PD adjoined by an concentric annular PD, partially separates the fiber modes by their respective size, shown in Fig. 1.6. The inner PD segment detects a majority of the power in the lower-ordered modes and, unavoidably, also some power in the high-ordered modes. The outer PD, however, detects power almost exclusively in the high-ordered modes. This selectivity between PD segments occurs strictly based on the size of the irradiance pattern. Subtraction of the photocurrents results in suppression of the ISI carried by the HOM. However, since the modal delay is monotonic with mode order, this results an improvement in the temporal width of channel impulse response, *i.e.* spatially resolved equalization (SRE) of the fiber response. Consequently, the fiber channel bandwidth improves significantly. More importantly, this use of a multisegment photodetector is fully compatible with standard optical receiver manufacturing.

Haas and Santoro have previously shown that useful improvement in link bandwidth is possible with mode-filtering via singlemode fiber at the MMF output [16]. However, the SMF acts as a "soft" aperture, where mode filtering occurs according to the overlap in their respective *electric field* profile. In contrast, the segmented photodetector provides a "hard" aperture, where, the spatial filtering acts upon the *irradiance* profile. Since perfect mode separation cannot be assured in the latter case, this mode-filtering is enhanced by subtraction of the residual power that is incident on the secondary, outer detector.

In this dissertation, the useful spatial diversity that exists in multimode fiber will first be demonstrated. A theoretical justification through numerical simulations, will be presented using well-known models of the graded-index multimode fiber. A number of permutation of the MSD and fiber will be considered to understand the limitations of SRE. The numerical modelling will also be used to demonstrate performance for conditions impossible to replicate in empirically. Finally, empirical data with fabricated photodetectors will be presented. The results will show that detection with SRE significantly improves the bandwidth of a fiber link with conventional detection. But equally important, SRE will be shown to be robust to variation in fiber parameters, launch condition, and even MSD geometry without the need for optimization on a link-by-link basis. Finally, improvements in channel response

will be verified by eye diagram and bit error rate measurements.

1.5 Other art

1.5.1 Wireless RF multipath environment

Similar to intermodal dispersion in MMF, a common phenomena in wireless RF links is multipath fading. A passband RF signal propagates in free-space between two antenna. However, with an omnidirectional transmission, the path taken from transmitter to receiver may include reflection off randomly located scatterers. The convergence of the multiple signals of differing phase at the receiving antenna will result in an interference, or multipath fading, in the frequency band of interest. The transmission link in the wireless case differs in two significant manner compared to an multimode fiber optical link. First, the output signal of the “receiver” in the wireless case is still the modulated RF signal, the spectral bandwidth of which is small with respect to the carrier frequency. In contrast, the receiver signal in the optical link is unavoidably down-converted from a modulated carrier wave to the baseband signal, with a spectrum spanning from DC to multi-GHz. Second, in omnidirectional wireless link, the receiver receives only a small portion of the transmitted power due to a limited receiver aperture. In a typical optical link, however, the receiver collects all the power that had not been lost to entropy.

A common method of combatting this multipath fading is the use of multiple antennae to exploit spatial diversity of the multipath environment [17]–[20]. The signal received by multiple antennae, sufficiently separated, are combined with an arbitrary weight shown in Fig. 1.7. Through adaptive algorithms, signal-to-noise ratio (SNR) of the receiver signal is maximized, [21], [22]. As a result, the receiving antennae system becomes a directional antenna, pointing in the direction of least interference.

Likewise, the use of a multisegment photodetector is similar to this. It preferentially detects only the low-ordered modes, disregarding the power all other signals. However, it should be noted that this can only be achieved by redistribution of the limited optical power. Filtering out portion of the available power will naturally result in penalty of the SNR. In

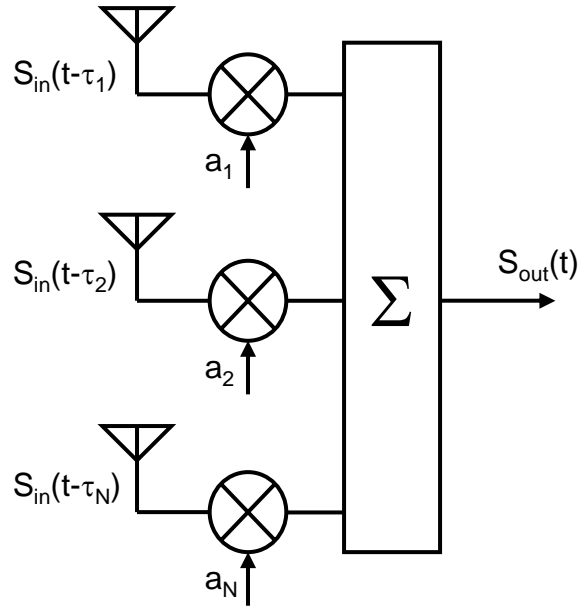


Figure 1.7: Exploiting spatial diversity in wireless RF links.

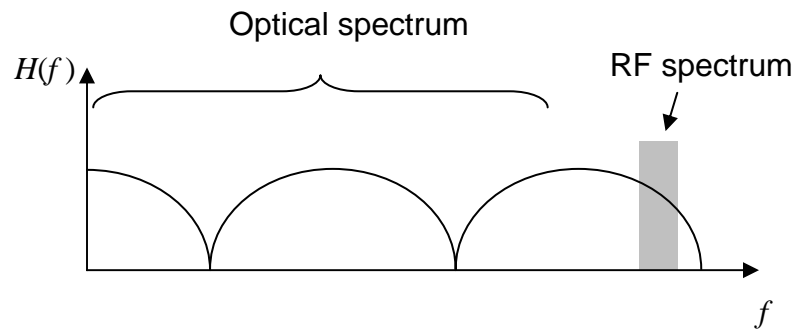


Figure 1.8: Spectrum of multipath fading with respect to the frequency band of interest for both optical and RF links.

contrast, the use of additional antenna in the wireless link will increase the received power; SNR can be maintain even by limiting the available signal paths. Equally significant, the diversity combination of in the wireless like is achieved with signal of narrow bandwidths. Electronically tunable component for such signal are readily available for a wide range of operating frequencies. Moreover, with the available mobility of mode wireless system, the need for adaptation is required. In contrast, the broadband nature of the received signal in a optical like makes tunability of phase or amplitude difficult. Fig. 1.8. Fortunately, *a priori* knowledge of the multiple signals is available. The modal profile does not change significantly from fiber-to-fiber; therefore, simplified approach to diversity combination can be used with multimode fiber.

1.5.2 Electronic equalization

In any bandwidth limited channel, the cutoff frequency may be improved by the flattening the frequency response with an equalizer circuit [18], [23]. Power is taken from the low-frequency regimen and moved to higher frequency band, shown in Fig. 1.9. Modern equalizers use a feedforward (FFE) and feedback (FBE) networks that add replicas of the received signal, scaled to achieve an improved impulse response shape. However, the magnitude of the impulse response typically diminishes. With quantized signals, electronic equalization decision based feedback network can be simplified with a decision feedback equalizer (DFE), shown in Fig. 1.10, [18]. *A priori* information of the intended signal levels and their resulting ISI on the following bits means knowledge of the current signals level can more effectively be used to reduce ISI from the subsequent samples.

DFE is a proven methodology that is used with limited bandwidth channels in a number of application: mobile phones, hard-drive and printed-circuit boards [24]–[27]. And, with the variety of dispersions present in both singlemode and multimode fiber, the DFE has gained much attention in optical communications as a general purpose, electronic dispersion compensation (EDC). Numerical simulation have shown that EDC can increase MMF channel bandwidth by 2–3×, [28]–[30]. However, these simulation, give little consideration to real issues such as clock recovery, timing jitter and limited accuracy available with 10-GHz

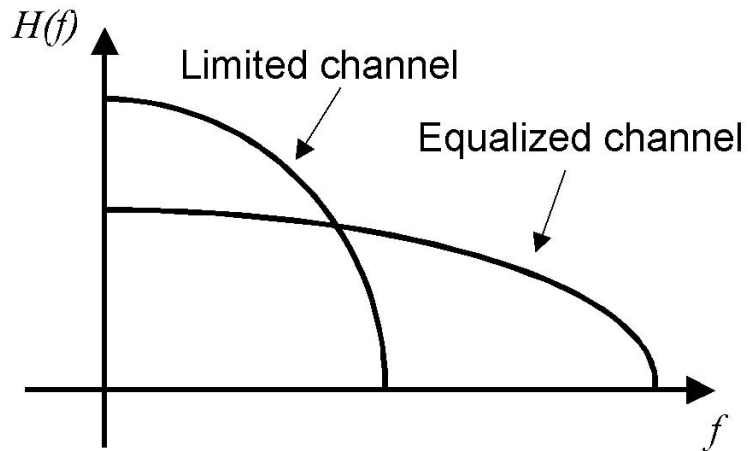


Figure 1.9: Spectrum of bandwidth limited channel with and without equalization.

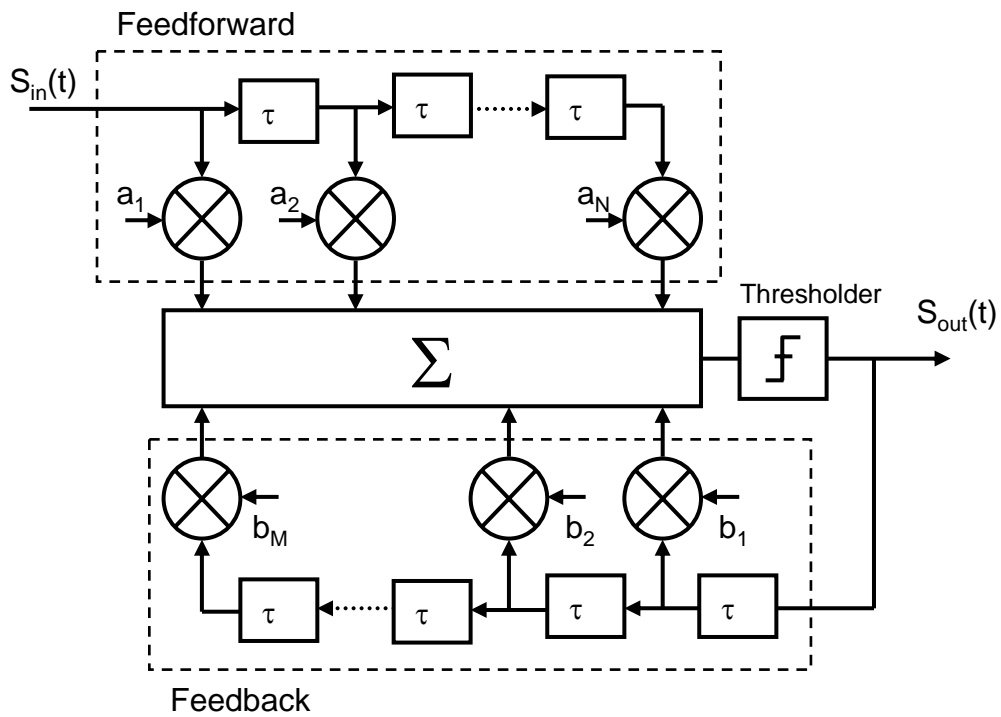


Figure 1.10: Block diagram of electronic equalizer. Decision feedback equalization implemented with thresholder device at output for signal adder. Copies of the signal, delayed by an integer multiple of the data rate $1/\tau$, are combined with optimized scaling a_n and b_m .

bandwidth hardware. Moreover, because of the high degree of variability in the impulse response of MMF links, wide-spread use of EDC will require monitoring of the signal quality over ultrawide bandwidths. To maximize the cost-effectiveness of using MMF, adaption of the EDC control must occur automatically, with manual intervention.

In this regard, DFE is justified only by the economy-of-scales demonstrated with silicon CMOS technology. State-of-the-art in CMOS technology have allowed demonstration of DFE structures with complex DFE to implement at 1 Gb/s [31], [32]. And, indeed, a number of companies have begun development of EDC for 10-Gb/s links. These chips have been developed for chromatic and polarization mode dispersion. Volume-pricing is expected to be in the \$50–100 range [33], well within the cost targets; however, it is yet unknown how widely applicable they are for the installed-base of MMF for which bandwidth must improve by 3 \times .

Equalization of multimode fiber link improves on the concept of FFE. By exploiting *a priori* knowledge of the spatial mode profiles, the ISI energy is sampled and directly removed from the from the main signal. No assumption is made on the data format or either the clock frequency or phase. Nor is there a requirement to tuning weighting coefficient, despite high variability of the fiber response. Of course, the lack of adaptiveness will certainly limit the maximum achievable channel improvement, but, it is this feature that make SRE highly robust and cost-effective. Moreover, while EDC is potent, currently state-of-the-art in electronics limits the extent to which DFE can be employed at 10 Gb/s data rates. The maximum data rate for which DFE-based EDC can operated is fundamentally limited by the propagation delay in CMOS transistors. The use of SRE can be used to simplify the implementation of DFE that may be used.

1.5.3 Restricted mode launch

A transmitter based solution for mitigation of DMD in multimode fiber exists in the form of restricted mode launch (RML). Here, the signal is allowed to transmit in only a subset of the fiber modes [35]–[37]. In this way, the impact of the disparate group delay among fiber modes is mitigate. Current methods of implementation is to first launch the optical

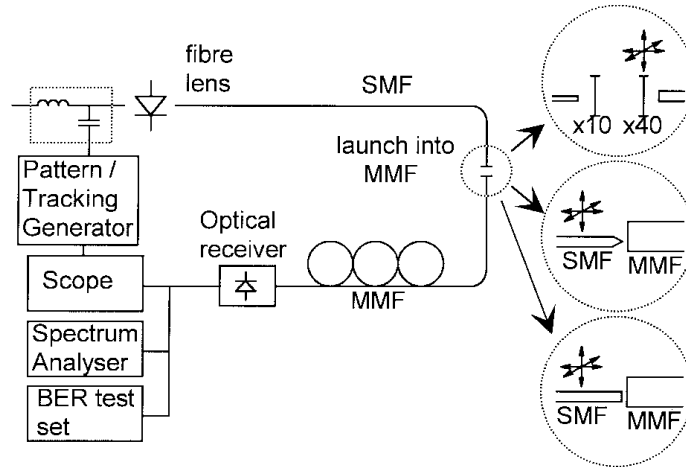


Figure 1.11: Restricted mode launch for minimizing the excitation of fiber modes [34].

signal into a singlemode fiber which can then be used to selectively couple the optical signal to a subset of MMF modes, shown in Fig. 1.11 [16], [34], [38]. While a doubling of link bandwidth has been shown to be possible, the advantage of MMF is obviated. Not only is strict control on the offset between the SMF and MMF fiber axes is required, but issues of coupling the optical signal to SMF is re-introduced. Thus, such solutions are limited to edge-emitting laser which are not as cost-effective as VCSELs. Provision in Gigabit Ethernet standard allow for the use RML [39], by the use of a mode-conditioning patchcord that optimally couples optical signal from a singlemode laser source to the MMF; however, the labor-intensive production of these patchcords keep the unit prices near \$300–400. Consequently, they have fallen out of favor with network service providers. Even with an increasing need for maximizing fiber bandwidth for 10 Gb/s transmission, the use of RML via mode-conditioning patch cords are being discontinued as datacom standards continue evolve.

CHAPTER 2

THEORY AND NUMERICAL MODELLING

“Don’t panic.”

— *The Hitchhiker’s Guide to the Galaxy* by Douglas Adams

This chapter delves into the theories pertaining to multimode fiber and spatially resolved equalization. Theoretical understanding of wave propagation in multimode fiber is implemented in a numerical model of the MMF link. Spatially resolved equalization is considered in the context of the fiber impulse response, altered by the use of a multisegment photodetector.

The underlying theory of wave propagation in optical waveguide is well described and widely accepted [34], [40]–[43]. With multimode fiber, however, the challenge is in accurately and precisely parameterizing the waveguide. The intractable properties of the fiber profile along the entire length make parameterizing MMF difficult. The response of the fiber to optical stimuli can vary significantly with minor variations in mode-quality of the source, micro or macrobending of the fiber, wavelength, etc. The entire multimode fiber link, *i.e.* source, fiber and detector, must be considered as a whole. Indeed, the measured response of one fiber link can rarely be used to accurately predict that of another seemingly identical link. For this reason, efforts to precisely parameterize MMF have been considered impractical. In this chapter, the results derived from simulation are presented for qualitative rather than quantitative analysis.

Issues regarding robustness of SRE to parameters such as source coupling, wavelength, core size, and core profile will be addressed. Nominal simulation parameters will be for transmission of 850-nm signal over 50- μm -core, graded-index, multimode fiber; however,

perturbation of various simulation parameters will be employed.

2.1 Implementation of theory

The multimode fiber is modelled as an ideal multipath environment. For each path of propagation the following parameters are computed: relative modal power, group delay, and detection efficiency. An impulse response of the fiber link is computed assuming an idealized multimode fiber. Neither core profile distortion nor the ensuing intermodal coupling are implemented in this model. Additionally, non-coherent modal interaction is assumed at detection. The flow diagram of this simulation routine is presented in Fig. 2.1.

2.1.1 Wave propagation in the optical fiber

The mathematical model of wave propagation in multimode fiber, begins with the well-known Helmholtz wave equation:

$$\nabla^2 \mathbf{E}(x, y, z, t) - \mu\epsilon \frac{\partial^2}{\partial t^2} \mathbf{E}(x, y, z, t) = 0, \quad (2.1)$$

where ∇^2 is the Laplacian operator. This is derived from Maxwell's equations [44]. Equation 2.1 describes the propagation of electric-field vector $\mathbf{E}(x, y, z, t)$ (V/m) in a charge free material described by the permeability μ (H/m) and permittivity ϵ (F/m). In the general case, either of material parameters μ or ϵ may vary with x , y or z ; however, variation in ϵ are assumed to be sufficiently small that $\nabla\epsilon/\epsilon$ is negligible.

The propagation of signal, with carrier oscillation frequency ω_o (radians/sec), along the z -axis in the MMF is the superposition of multiple time-harmonic, electric-field plane waves of mode m , described by the following phasor notation expression

$$\mathbf{E}(x, y, z, t) = \sum_m \hat{\mathbf{e}}_m E_m(t) \Psi_m(x, y) \exp[j(\omega_o t - \beta_m z)], \quad (2.2)$$

where $\hat{\mathbf{e}}_m$ is the unit vector in the direction of the electric field, $E_m(t)$ (V/m) is the magnitude, $\Psi_m(x, y)$ is the unitless, normalized transverse profile, ω_o (radians/s) is the wave oscillation frequency, and β_m (radians/m) is wave number. The constituent plane waves

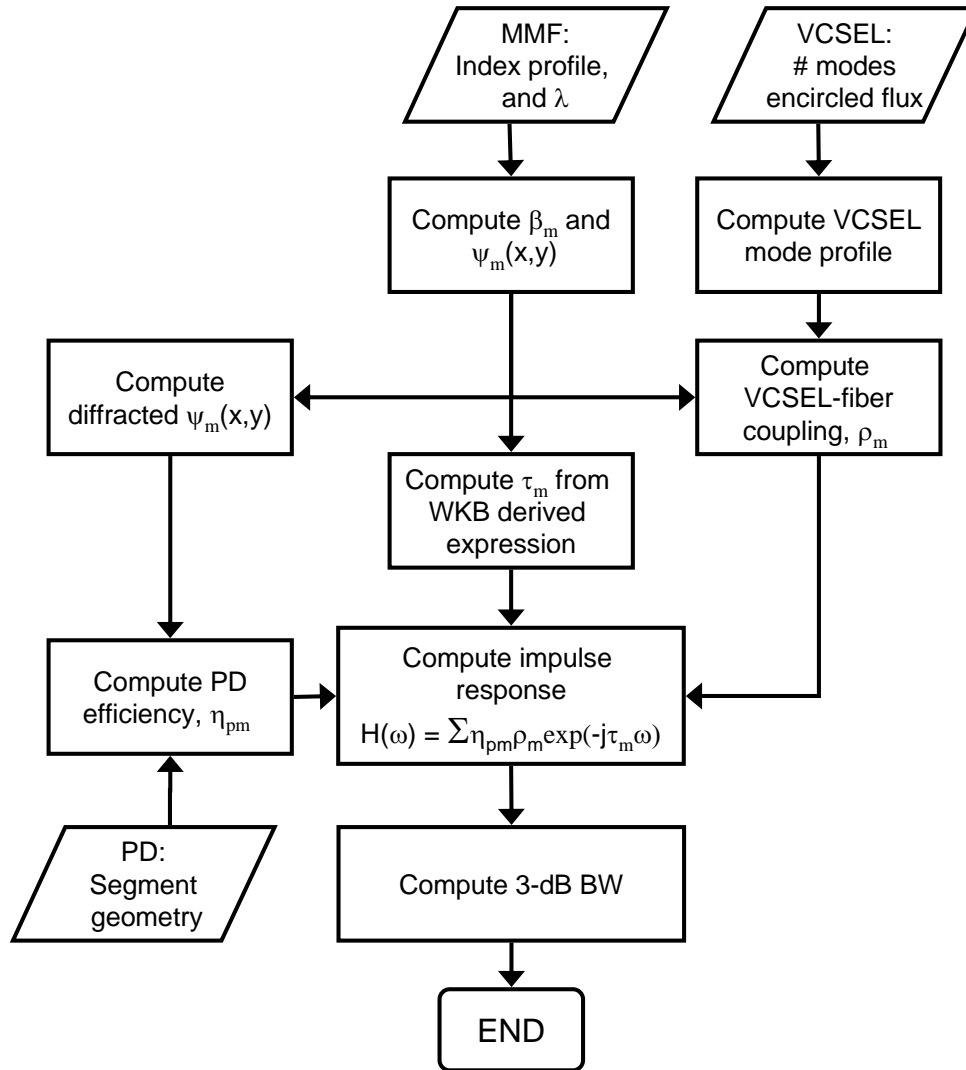


Figure 2.1: Flow diagram for numerical modelling of multimode fiber link.

that define $\mathbf{E}(x, y, z, t)$ are uniquely defined by wave number β_m and a corresponding orthonormal basis set $\Psi_m(x, y)$. The Helmholtz wave equation can be simplified to a scalar wave equation,

$$\nabla_{\perp}^2 \Psi_m + k_o^2 n^2 \Psi_m = \beta_m^2 \Psi_m. \quad (2.3)$$

∇_{\perp}^2 is the transverse Laplacian, k_o (radians/m) is the free-space wave number of the field, and the refractive index n is $\sqrt{\epsilon/\epsilon_o}$, where ϵ_o is the permittivity constant 8.85 pF/m [41]. Equation 2.3 is applicable for a time-varying envelope, *i.e.* $dE_m/dt \neq 0$, conditional on the variation be small with respect to ω [45]; for much of work presented here, $E_m(t)$ is assumed to vary at least 4 order of magnitude slower than ω .

Modes of propagation, in a multimode fiber that is represented by the dielectric profile $n(x, y)$, exhibit an effective wave number β_m and transverse profile $\Psi_m(x, y)$ that satisfies (2.3). For multimode fiber, $n(x, y)$ is assumed to be linear, *i.e.* independent of $E_m(t)$. Among the many possible solutions to (2.3), those that satisfy the following condition in some part of the medium are regards as the guided-modes:

$$\min[k_o n(x, y)] < \beta_m < \max[k_o n(x, y)].$$

Whereas singlemode fiber (SMF) has only one, multimode fiber possess two or more guided-mode solutions. A significant feature of $\Psi_m(x, y)$, for guided-modes, is that they exhibit an oscillatory behavior within the fiber core, but more importantly, each unique guided-mode possesses a mode profile $\Psi_m(x, y)$ that is orthogonal to all other guided-mode solutions [45];

$$\iint_{\infty} \Psi_m(x, y) \Psi_n^*(x, y) dx dy = 0 \quad (2.4)$$

when $m \neq n$.

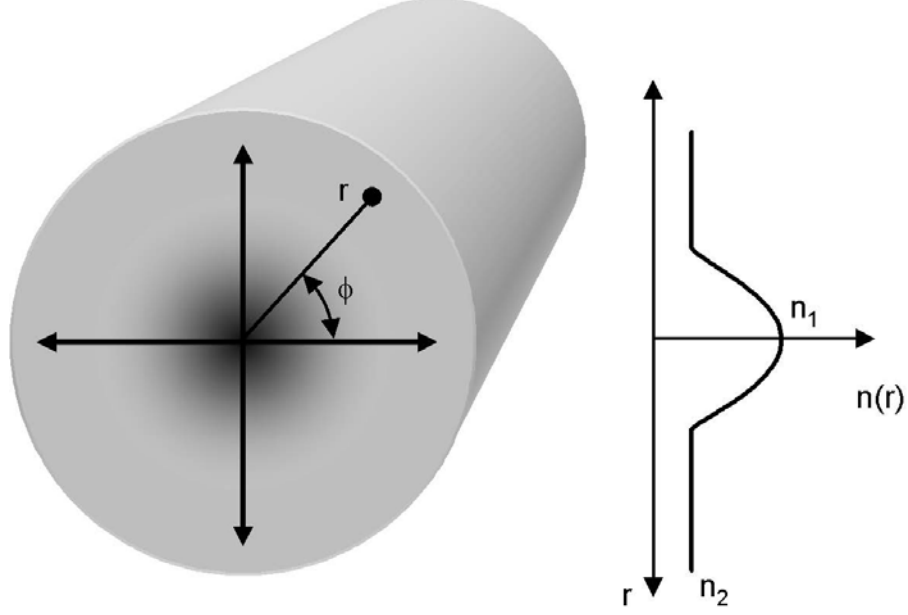


Figure 2.2: Index profile of graded-index profile for communication links. Parabolic index $n(r) \propto r^\alpha$, where $\alpha \approx 2$.

2.1.1.1 Implementing the wave-equation for graded-index MMF

The index profile of real graded-index multimode fiber is designed to closely match the following functional form, shown in Fig. 2.2:

$$n(r, \phi) = \begin{cases} n_1 \sqrt{1 - 2\Delta \left(\frac{r}{a}\right)^\alpha} & 0 \leq r \leq a \\ n_1 \sqrt{1 - 2\Delta} & r > a \end{cases}, \quad (2.5)$$

where r is the radius from the fiber axis. The parameter a is radius of core region; n_1 is the maximum refractive index of the core; n_2 is the index in the cladding; α is the index profile exponent very close to the value 2; Δ is the contrast ratio defined as

$$\Delta \equiv \frac{(n_1^2 - n_2^2)}{2n_1^2}. \quad (2.6)$$

Since $n(r, \phi)$ is ϕ -invariant, $\Psi_m(x, y)$ is assumed to be separable, in the cylindrical coordinate, into a radial function $R_m(r)$ and azimuthal function $\Phi(\phi)$ [41];

$$\Psi_m(r, \phi) = R_m(r)\Phi_m(\phi), \quad (2.7)$$

Thus, (2.3) is separated and simplified into the following two equations:

$$\frac{d^2 R_m(r)}{dr^2} + \frac{1}{r} \frac{dR_m(r)}{dr} + \left(n^2(r) - \beta_m^2 - \frac{\nu^2}{r^2} \right) R_m(r) = 0, \quad (2.8)$$

and

$$\frac{d^2 \Phi_m(\phi)}{d\phi^2} + \nu^2 \Phi_m(\phi) = 0. \quad (2.9)$$

The solution to (2.9) is readily arrived at;

$$\Phi(\phi) = A_o \exp(-j\nu\phi), \quad (2.10)$$

with integer values for the azimuthal mode number ν and amplitude A_o . We assume A_o is a complex number, but $|A_o| = 1$. On the other hand, in real multimode fiber the value of α is rarely an integer; therefore, a solution (2.8) cannot be reached analytically. To this end, Gloge [3], [46] approaches the radial mode profile from a ray-optics approach. By restating (2.8) as

$$R_m(r) = \exp(-jk_o s(r)), \quad (2.11)$$

where $s(r)$ is an unknown scalar function approximated by the power series, Gloge exploits the method of Wentzel, Krammers, Brillouin, and Jeffreys (WKBJ method) applied to cylindrical structures [5], [47], and arrives at a closed-form solution to β_m as a function of a mode number m [41];

$$\beta_m = n_1 k_o \left[1 - 2\Delta \left(\frac{m}{M} \right)^{\frac{\alpha}{\alpha+2}} \right]^{\frac{1}{2}}, \quad (2.12)$$

where M is the total number of non-degenerate modes given by

$$M = a^2 \Delta k_o^2 n_1^2 \left(\frac{\alpha}{\alpha+2} \right). \quad (2.13)$$

From this expression, the modal delay per unit length of fiber is computed:

$$\tau_m = \frac{d\beta_m}{d\omega}. \quad (2.14)$$

In this computation only m and α are assume to be independent of optical frequency ω_o , such that the following expression is arrived at [8]

$$\tau_m = \frac{N_1 L}{c} \left[1 + \Delta C_1 \left(\frac{m}{M} \right)^{\frac{\alpha}{\alpha+2}} + \Delta^2 C_2 \left(\frac{m}{M} \right)^{\frac{2\alpha}{\alpha+2}} + O(\Delta^3) \right], \quad (2.15)$$

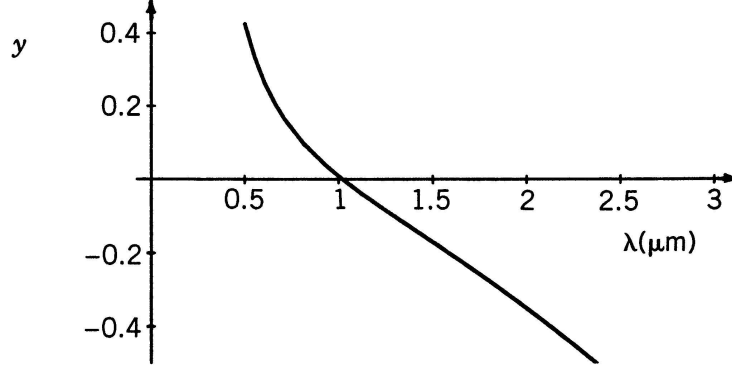


Figure 2.3: Profile dispersion of 13.5% GeO₂-doped fused-silica multimode fiber [41].

where

$$C_1 = \left(\frac{\alpha - 2 - y}{\alpha + 2} \right),$$

$$C_2 = \left(\frac{3\alpha - 2 - 2y}{2\alpha + 4} \right),$$

N_1 is the group index of the waveguide material, $c = \omega_o/k_o$, and y is the profile dispersion, shown in Fig. 2.3, given by

$$y \equiv -\frac{2n_1}{N_1} \frac{\lambda}{\Delta} \frac{d\Delta}{d\lambda}. \quad (2.16)$$

The derivation for τ_m from the closed-form expression for β_m has been shown to describe well the relative temporal behavior of graded-index multimode fiber. Indeed, it has become *de facto* in analyzing the behavior of multimode fiber, including recent works in developing Gigabit Ethernet and Fibre Channel standards [37].

We will use (2.15) to predict the group delay of modelled fiber; however, to incorporate the relationship of mode profile in the context of a multisegment photodetector, $\Psi_m(x, y)$ must be known. To attain the mode profile, the radial profile $R_m(r)$ is first solved by a finite difference approximation of the differential equation (2.8); the details of this approximation is presented in Appendix A. Using a numerical computation package such as MATLAB[©], all real solutions of $R_m(r)$ are found, from which the radial profile of the guided-modes are computed. With the analytical solution of $\Phi_m(\phi)$, the two-dimensional, transverse profile

of all fiber modes are computed:

$$\Psi_m(r, \phi) = R_m(r) \exp(j\nu\phi). \quad (2.17)$$

The use of a complex-valued Ψ_m maintains information on rotational degeneracy that is critical for computation of source-fiber coupling.

2.1.2 Modelling of the optical source

A commercial VCSEL source, Honeywell HFE4092, is used as the model of the MMF link laser source. The nominal performance specifications are used as the basis for the VCSEL parameters [48]. The VCSEL emission is emulated with as the sum of the 5 lowest-order mode for a weakly-guiding, circular, step-index waveguide. A waveguide with an numerical aperture of 0.2—corresponding to nominal beam divergence of 15° —is used as the basis for the mode profile of the VCSEL emissions. The center wavelength is 850 nm. The transverse dimension is scaled to satisfy the encircled-flux criteria established in IEEE 802.3ae standards (10-Gigabit Ethernet) for VCSEL illumination¹, assuming equal power in each VCSEL mode.

A source illumination pattern $\Psi_S(x, y)$ is computed from the combined field profile of the VCSEL model. The relative power coupled into each fiber mode with profile $\Psi_m(x, y)$ is computed by the overlap integral;

$$\rho_m = \Gamma_m^2 \frac{\left| \iint_{\infty} \Psi_m(x, y) \Psi_S^*(x, y) dx dy \right|^2}{\iint_{\infty} |\Psi_m(x, y)|^2 dx dy \iint_{\infty} |\Psi_S(x, y)|^2 dx dy}, \quad (2.18)$$

where Γ_m is the Fresnel reflection;

$$\Gamma_m = \frac{k_s - \beta_m}{k_s + \beta_m}, \quad (2.19)$$

where β_m is the wave number of the respective fiber mode and k_s is the wave number of the incident optical signal.

¹IEEE802.3ae requires less than 30% of the total VCSEL power to be within a $4.5\text{-}\mu\text{m}$ radius and greater than 86% total VCSEL power to be within a $19\text{-}\mu\text{m}$ radius.

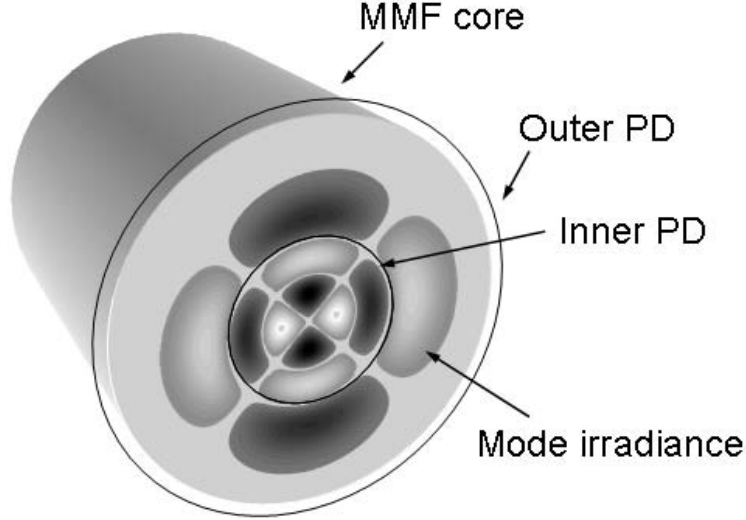


Figure 2.4: Use of concentric, multisegment photodetection to exploit spatial diversity of optical modes.

2.1.3 Modelling of the segmented photodetector

At the receiver end, the multisegment photodetector is simulated. The PD is divided into circular, concentric regions, shown in Fig. 2.4: an inner disc segment and an outer annular PD. Ideal photodetection is assumed such that all optical power is incident on either of segments, thus the salient parameter of the MSD is the radius of the inner PD segment. The quantum efficiency η_m of any mode m is determined by the overlap of the PD geometry, described by area A_p , and the impinging irradiance profile $|\Psi_m(x, y)|^2$;

$$\eta_{pm} = \frac{\iint_{A_p} |\Psi_m(x, y)|^2 dx dy}{\iint_{\infty} |\Psi_m(x, y)|^2 dx dy}, \quad (2.20)$$

where the subscript pm signifies the relation of fiber mode m to photodetector p .

For the two-segment PD, the detection efficiency is the combination of the two segment of area A_1 and A_2 . For the conventional detection,

$$\eta_m = \eta_{1m} + \eta_{2m}, \quad (2.21)$$

where η_{1m} and η_{2m} are the detection efficiencies of inner and outer PD segment respectively. Since *all* optical power is incident on either PD segment, i.e. $A_1 + A_2 \in \infty$, clearly $\eta_m = 1$.

For the embodied SRE, on the other hand, the net efficiency is

$$\eta_m = \eta_{1m} - \eta_{2m}. \quad (2.22)$$

Or more simply,

$$\eta_m = 2\eta_{1m} - 1. \quad (2.23)$$

It should be noted that in practice the PD will experience "shadowing" by the planar electrode structure of the detector, producing a localized finger shadowing effect that can be up to 40% of the total PD area. However for simplicity the effect of finger shadowing is assumed to be negligible relative to the minimum feature sizes of Ψ_m .

A finite gap between output facet of the fiber and the MSD is allowed for in simulation of the PD, Fig. 2.5; diffraction of the fiber modes is also included prior to computation of η_m . The mode-field profile is decomposed into a continuum of plane waves of transverse wave numbers k_x and k_y and amplitude $A(k_x, k_y)$;

$$A(k_x, k_y) = \iint_{\infty} \Psi_m(x, y) \exp\left[-j(k_x x + k_y y)\right] dx dy \quad (2.24)$$

and can readily be computed by the two-dimensional Fourier transform of $\Psi_m(x, y)$. The resultant field at some distance ℓ from the fiber end is the sum of the plane wave continuum with a shift in phase by $(k_x x + k_y y + k_z \ell)$, where $k_z = \sqrt{k_o^2 - k_x^2 - k_y^2}$;

$$\Psi_m(x, y, \ell) = \iint_{\infty} A(k_x, k_y) \exp(jk_z \ell) \exp\left[j(k_x x + k_y y)\right] dk_x dk_y. \quad (2.25)$$

The field $\Psi_m(x, y, \ell)$ is readily computed by the two-dimensional inverse-Fourier transform of term $A(k_x, k_y) \exp(jk_z \ell)$.

2.1.4 Modelling of the system link

We characterize the optical fiber by the impulse response responsible for the distortion, relative to the back-to-back optical link. This back-to-back link represents the response of the opto-electronic (OE) components—the laser and photodetector—to the electrical stimuli. Since the laser produces an optical irradiance proportional to input electrical signal and the photodetector produces an electrical signal proportional to the input irradiance,

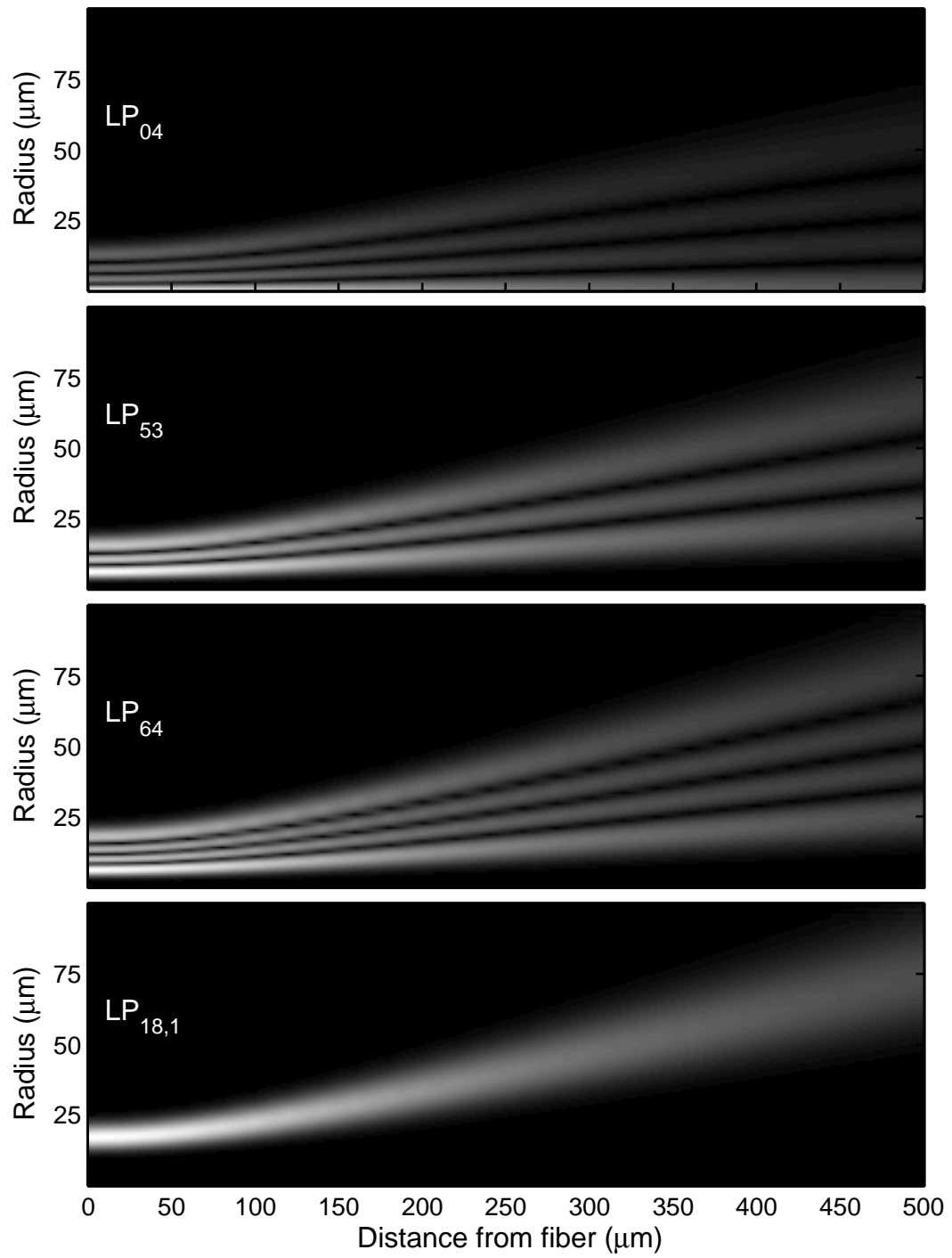


Figure 2.5: Computed radial profile of diffracted mode-field profile $|R(r)|$ for 50- μm graded-index MMF.

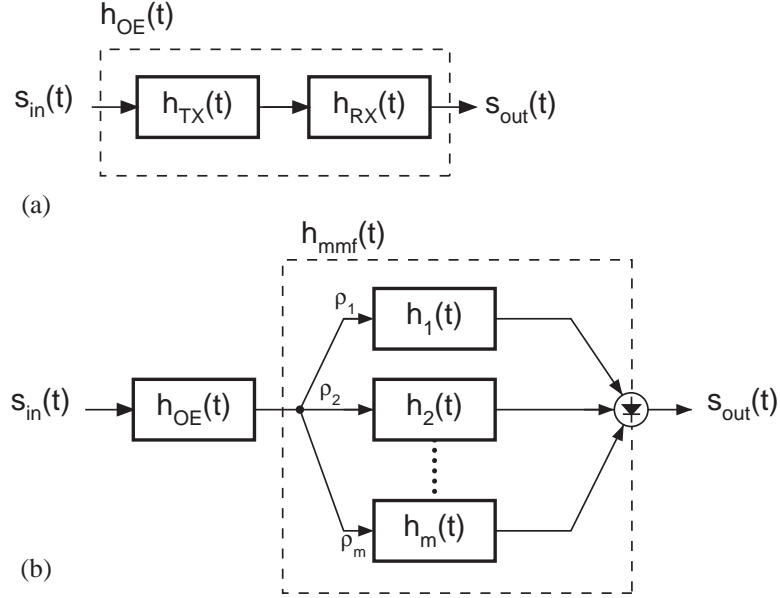


Figure 2.6: (a) System model of back-to-back optical link using square-law transmitter and receiver. (b) System model of fiber link with conventional photodetection.

$h_{OE}(t)$ is linear to the input signals, shown in Fig. 2.6(a). Incoherence among modes results in an irradiance at the fiber output is the sum of irradiance of each mode; therefore, the optoelectronic component response $h_{TX}(t)$ and $h_{RX}(t)$ can be lumped into one response $h_{OE}(t)$. Indeed, it will be shown in Chapter 3, that this incoherence is not only a convenient assumption but also a reasonable one. In the limit where the modal signal interact incoherently, the fiber impulse response $h_{mmf}(t)$ is thus the sum of parallel channels [23];

$$h_{mmf}(t) = \sum_m \rho_m \delta(t - \tau_m). \quad (2.26)$$

Here, the distortion by intermodal dispersion is assumed to be far greater than that due to light propagation with the mode itself, *i.e.* chromatic or polarization-mode dispersion.

While temporal response provides a intuition in the behavior of the fiber, quantitative information is more readily available in the frequency domain. Using the Fourier transform identity

$$\delta(t - \tau) \xleftrightarrow{\mathcal{F}} \exp(-j\omega\tau), \quad (2.27)$$

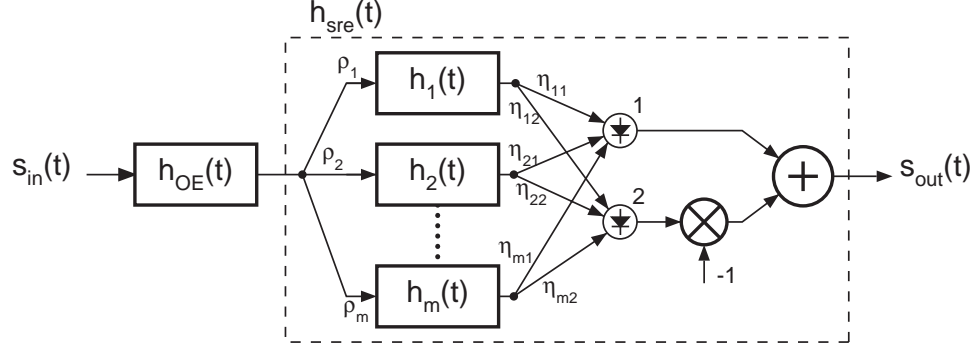


Figure 2.7: System model MMF link model, with spatially resolved equalization.

the frequency domain response can be computed straightforwardly:

$$H_{mmf}(\omega) = \sum_m \rho_m \exp(-j\omega\tau_m) \quad (2.28)$$

From this, the 3-dB cutoff frequency f_{3dB} can be inferred. This is the frequency at which the channel gain is 3-dB lower than that at DC. Since modal delay is computed per unit length of fiber, the resulting bandwidth will, in fact, be a bandwidth-distance product. Equation (2.26) describes the “response” of the fiber on communication link in two ways. Not only is τ_m a measure of the temporal effect on the input signal, but ρ_m is a measure of the a spatial ”filtering”. The VCSEL irradiance profile is the spatial embodiment of the transmitted signal.

As is typical done with analysis of MMF link, the equations (2.26) and (2.28) assume uniform detection of each fiber mode. This is not so necessarily so with the segmented PD. Indeed, it is for the specific purpose of modifying the MMF impulse response by some mode dependent detection, *i.e.* η_m , that an MSD is used. The equalized impulse response of the fiber, shown in Fig. 2.7, is given by

$$h_{sre}(t) = \sum_m \eta_m \rho_m \delta(t - \tau_m), \quad (2.29)$$

or equivalently,

$$H_{sre}(\omega) = \sum_m \rho_m \eta_m \exp(-j\omega\tau_m). \quad (2.30)$$

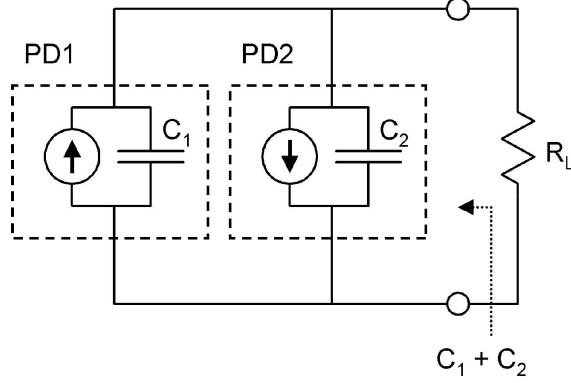


Figure 2.8: Circuit model of parallel PD segment with opposite polarity.

It should be pointed out that in (2.29), the impulse response of both MSD segments are assumed to be identical. However, it can be shown that this should be the case, for a properly designed MSD including effects of both transit time and device capacitance. Transit times of photo-generated carriers in a detectors are governed by device substrate material and the distance and applied voltage between electrodes. Since these factors need not change with detector periphery or segmentation, the same transit time is achieved for both PD segments of identical structure. On the other hand, capacitance of a detector is directly proportional to its area. Since the segmentation of a PD may result in detectors of unequal area, capacitance of each segment will vary also. However, if MSD segment are combined directly in parallel, as shown in Fig. 2.8, the photocurrent from either segment experiences the capacitance of both PD, thus the same impedance. Indeed, it will be shown in later discussion, that this condition is easily achievable.

A final note on the link simulation, the fiber model is incomplete in that mode-dependent attenuation and intermodal coupling are not included. These are the result of various factors include defects in the fiber, core-profile, macrobending, scattering, etc. Since the accuracy of the simulation is already limited by random variation in real fiber, the errors from these simplification is expected to be within the "noise" of real fiber links. That is, the variation between simulation and measured response will be within the range of variation among measured responses. We rely on experimental results to support conclusions drawn from

Table 2.1: Parameters of standard graded-index multimode fiber [49].

Parameter	Nominal	Units
Core Diameter	50	μm
n_1	1.47	
α	2	
Δ	0.01	
Length	1	km
y (@ 850 nm)	0.1	
y (@ 1300 nm)	-0.1	

simulation.

2.1.4.1 Link components parameter

The standard 50- μm core, graded-index MMF optical link is simulated with a simple, two-segment MSD. The nominal fiber parameters, based on typical manufacturer’s specifications² and are summarized in Table 2.1. The simulated source illumination pattern emulates that of a multimode VCSEL with a transverse modes 5-mode near 850 nm.

The resulting impulse response of the link, with and without the use of SRE, is parameterized by the 3-dB cutoff frequency f_{3dB} and optical loss η_{SRE} . To quantify the results of spatially resolved equalization, a bandwidth gain BWG is defined as the ratio of fiber bandwidth with and without equalization;

$$\text{BWG} \equiv \frac{f_{3dB,sre}}{f_{3dB,mmf}}, \tag{2.31}$$

where $f_{3dB,sre}$ and $f_{3dB,mmf}$ are the cutoff frequency of the impulse response with and without equalization, respectively. A change in optical loss, with the use of the MSD, is also computed. In actuality, the equalization results in a reduction of the electrical signal power; however, since such losses are typically compensated for with increased laser power,

²Specifications are common to both Corning and OFS 50- μm graded-index fiber. Due to limitation of fiber manufacturing technology, only approximate value of α is available

an equivalent optical penalty is computed instead:

$$\eta_{sre} = \frac{\sum_m \eta_m \rho_m}{\sum_m \rho_m}. \quad (2.32)$$

The optical penalty can be equivalently computed from the optical pulse energy [23];

$$\eta_{sre} = \frac{H_{sre}(0)}{H_{mmf}(0)}. \quad (2.33)$$

It is important to recognize, however, that in decibel units,

$$\eta_{sre} = \frac{1}{2} \left[H_{sre}(0) - H_{mmf}(0) \right] \quad (\text{dB}), \quad (2.34)$$

where the factor of 1/2 accounts for square-law photodetection.

2.1.5 Useful spatial diversity

It is by virtue of the different mode-field size that graded-index fiber reduces intermodal dispersion relative to step-index fiber. However, it is not obvious whether this diversity in size among the modes can be *easily* exploited with a multisegment photodetector. For this, it is necessary to understand the relationship of the size of a fiber mode to its respective group delay.

The encircled-flux $\text{EF}(r)$ is the relative power incident on surface of radius r , shown in Fig. 2.9;

$$\text{EF}(r) = \frac{\int_0^r \int_0^{2\pi} |E(\rho, \phi)|^2 \rho \, d\rho d\phi}{\int_0^\infty \int_0^{2\pi} |E(\rho, \phi)|^2 \rho \, d\rho d\phi}. \quad (2.35)$$

For the nominal MMF fiber, the half-width half-max of the encircled-flux HWHM_{EF} , *i.e.* the radius r_{EF} at which EF is 50%, is plotted versus modal delay of each mode. In Fig. 2.10(a), the expected behavior of increase mode size with increasing mode order is demonstrated. But more importantly, a near-monotonic relationship is clearly observed, in Fig. 2.10(b), between the size of a fiber modes and its modal delay. This indicates the modes impinging on the outer PD segment, based on similar mode size, also share a similar arrival time. Meaningful reduction in ISI is achieved for the inner PD signal by simply subtracting the two photocurrents, shown in Fig. 2.11.

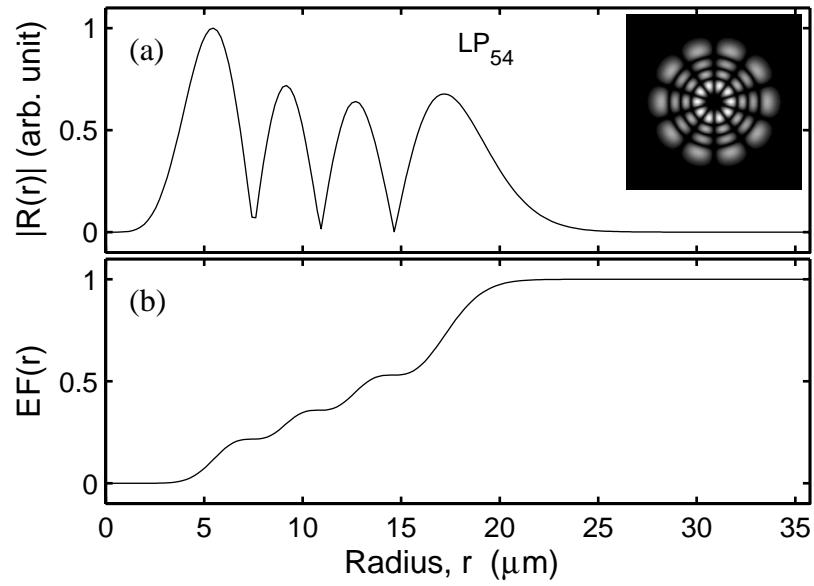


Figure 2.9: (a) Radial mode profile computed of mode LP_{24} in $50\text{-}\mu\text{m}$ GI-MMF. Inset plot shows full irradiance profile. (b) Computed encircled-flux.

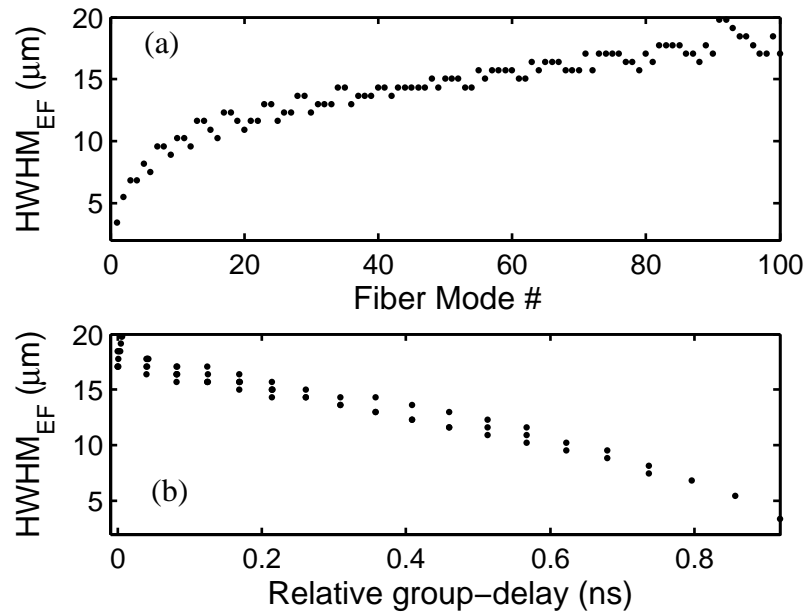


Figure 2.10: (a) group delay and 50% encircled-flux radius for fiber modes at 850 nm, in a $50\text{-}\mu\text{m}$ core MMF. (b) Correlation plot between group delay and encircled-flux

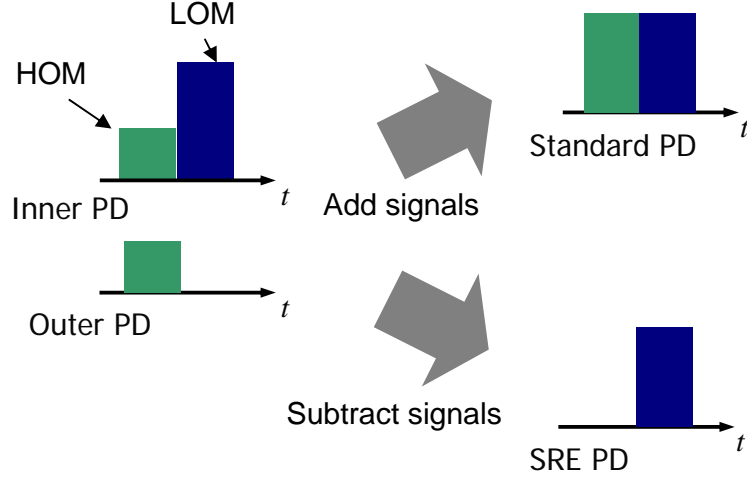


Figure 2.11: In this simplified representation, cancellation of ISI energy in high-ordered modes by sampling with annular PD and subtracting from inner PD. The remaining signal is primarily of low-ordered modes.

2.2 Simulation results

2.2.1 Nominal fiber bandwidth

With the nominal parameters of the multimode fiber and VCSEL, the impulse response of the fiber link with a conventional PD is computed, shown in Fig. 2.12. The relative power of each fiber mode is sorted according to the mode index m used in Gloge's closed-form expression for β_m , shown in (2.12). However, it is also common to group modes according to their respective group delay, shown in Fig. 2.12(b). Modes, which have unique transverse profile, are relate to each other by similar group delay but also a principal mode index q given by

$$q \equiv 2\mu + \nu - 1,$$

where ν reflects the number of oscillation full-cycles in the azimuthal while μ is the number of half-cycles in the radial directions, *e.g.* Fig. 2.9(a) inset. The frequency response, shown in Fig. 2.13(b), is computed by (2.28) with the group delay and modal power grouped by the mode index m ; however, temporal response is computed by combining the power belong to the mode index q and assigned a representative group delay, shown in Fig. 2.13(a). The

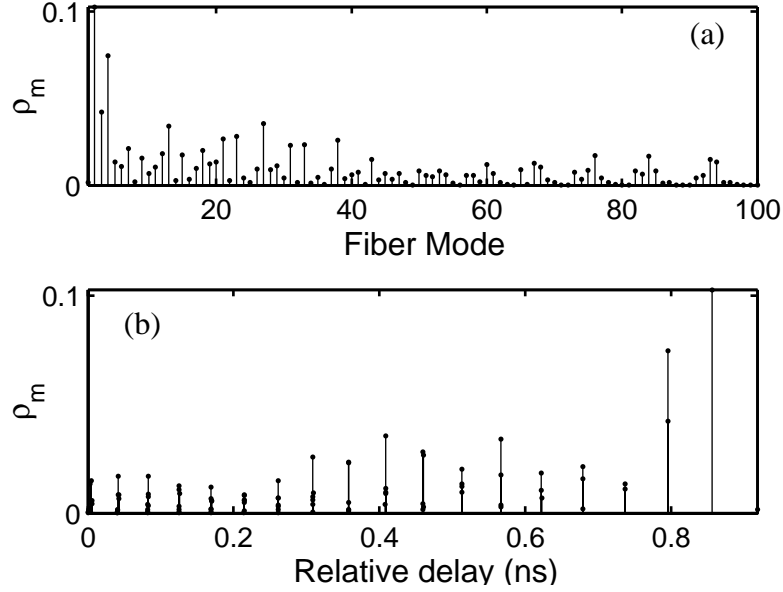


Figure 2.12: Relative modal power a 50- μm graded-index multimode fiber illuminated by a 5-mode, 850-nm VCSEL source. (a) Sorted according to mode number m . (b) Sorted according to relative group delay.

computed response shows a fiber bandwidth of 470 MHz-km, which is near to the nominal fiber bandwidth of 500 MHz-km.

2.2.2 Equalized fiber bandwidth

Under the same VCSEL launch condition, the response of the fiber equalized by the two-segment PD is computed. A MSD simulated to be 400 μm from the output facet of the fiber. To account for beam divergence, the simulated MSD has an inner PD radius of 55 μm .

The frequency domain of the electrical signal, shown in Fig. 2.14, shows an equalized fiber response that exhibits a f_{3dB} that is $2\times$ higher than that of $h_{mmf}(t)$, from 460 MHz-km to 920 MHz-km. This bandwidth improvement is the result of two effects. The ISI suppression clearly shifts the null frequency from 1 GHz, providing gain in this region. However, as is the case with any equalization, bandwidth gain also comes at a penalty in the low-frequency regime. In the electrical domain, this is a 6-dB loss in the DC regime,

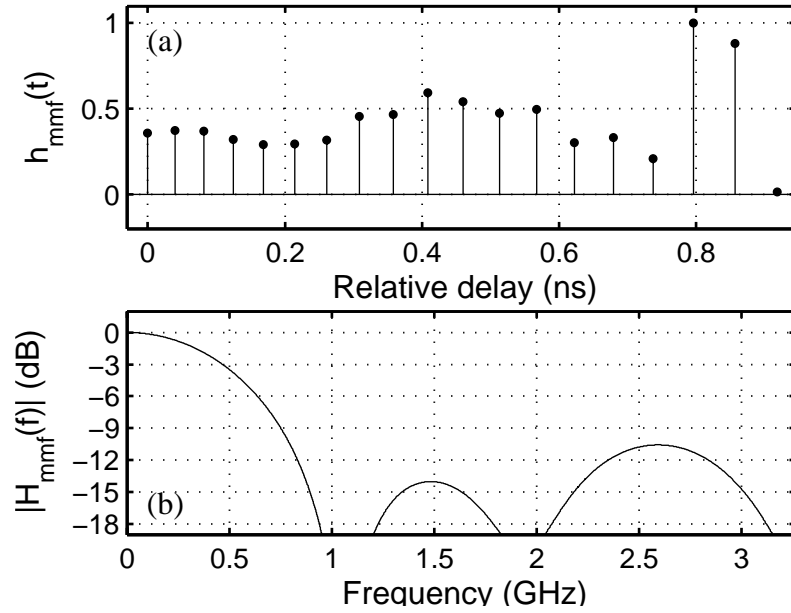


Figure 2.13: (a) Fiber impulse response with VCSEL-like optical source. (b) Frequency response.

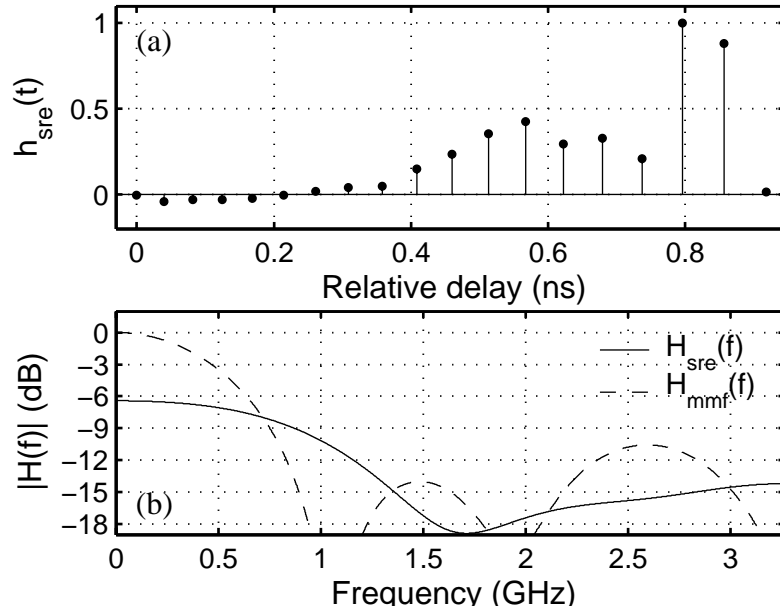


Figure 2.14: (a) Impulse response of equalized MMF link with 55- μm MSD. (b) Frequency response in comparison to non-equalized MMF.

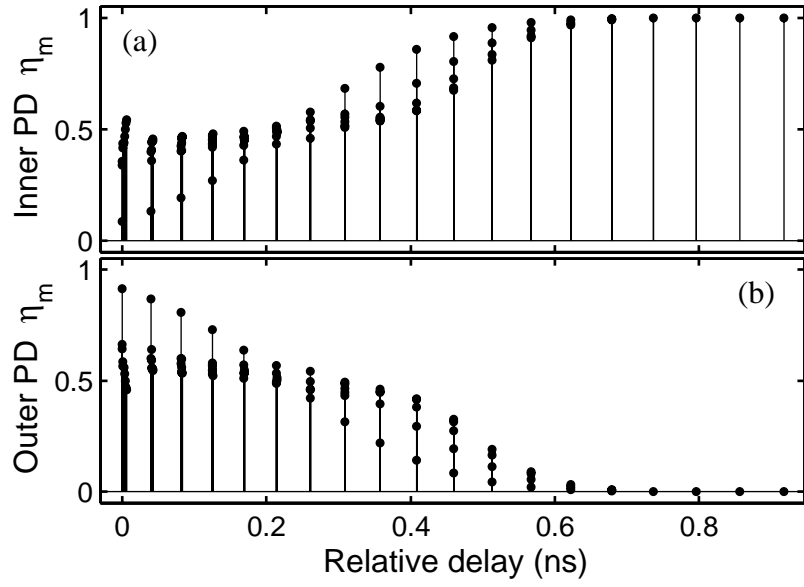


Figure 2.15: External quantum efficiency of fiber modes versus relative group delay for (a) inner PD and (b) outer PD.

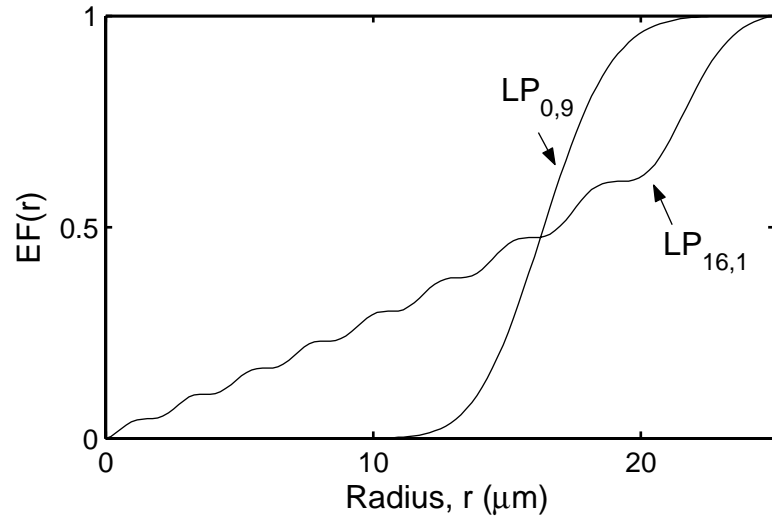


Figure 2.16: Representative of two modes (meridional and azimuthal modes) with near identical group delay and HWHM_{EF} , but disparate encircled-flux $\text{EF}(r)$.

which this can be compensated for with 3-dB increase in optical power.

Shown in Fig. 2.15 are the computed value of η_{pm} , for each mode and each segment of the MSD. A bimodal function of η_{pm} is observed that results from the difference in mode profile between meridional and azimuthal mode, shown in Fig. 2.16 of two representative modes. Nevertheless, the bimodal function has a small impact for the typical mode launch condition.

2.2.3 Optimizing SRE

The size and location of the MSD, with respect to the fiber, have been chosen according to practical limitation and necessary flexibility associated with experimental measurements. But more importantly, the combination of MSD size and fiber-MSD gap is chosen specifically to achieve a 2× improvement in bandwidth. Indeed, changing either of these parameters can result in more enhancement in bandwidth; however, this come at a penalty. In most MMF link standards, such as Fibre Channel and Gigabit Ethernet, allowances are made for losses in the optical signal of around 4–5 dB, including for fiber equalization. Exceeding these levels with SRE negates its applicability; therefore, to comply with these standards requirement, a limit of 3-dB optical penalty is chosen for SRE.

Shown in Fig. 2.17(a) is the gain in fiber bandwidth by MSD of various sizes located 400 μm from the fiber output. Clearly, bandwidth gains far exceeding 3–4× can be achieved. Likewise by locating a fixed 55- μm MSD at further distances from the fiber, thus exploiting the diverging beam, results in BWG larger than 2×, Fig. 2.17(b). However, with this embodiment of SRE with a subtraction of PD photocurrents, bandwidth gain is available only at a trade-off with η_{sre} , shown in Fig. 2.18(a). A near unity relationship exists between BWG and η_{sre} ; a bandwidth gain of 6× will results in $\eta_{sre} \approx 1/6$. However, after 2× BWG, additionally BWG comes exclusive at the cost of low-frequency power and little impact on the high-frequency signal. This results in an undesirable high-frequency "peaking" that produces ISI as well, shown in Fig. 2.18(b).

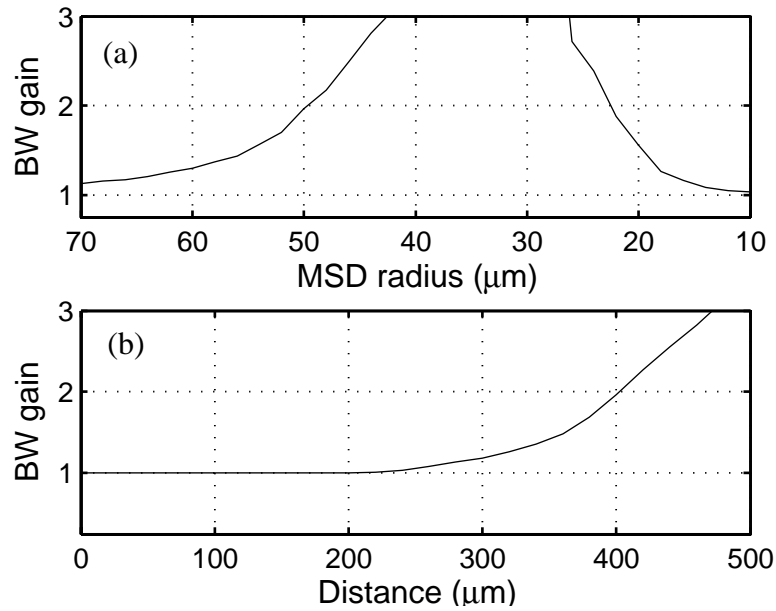


Figure 2.17: (a) Bandwidth gain versus radius of MSD placed at 400 μm from fiber output. (b) Bandwidth gain versus fiber-MSD gap for 55- μm MSD.

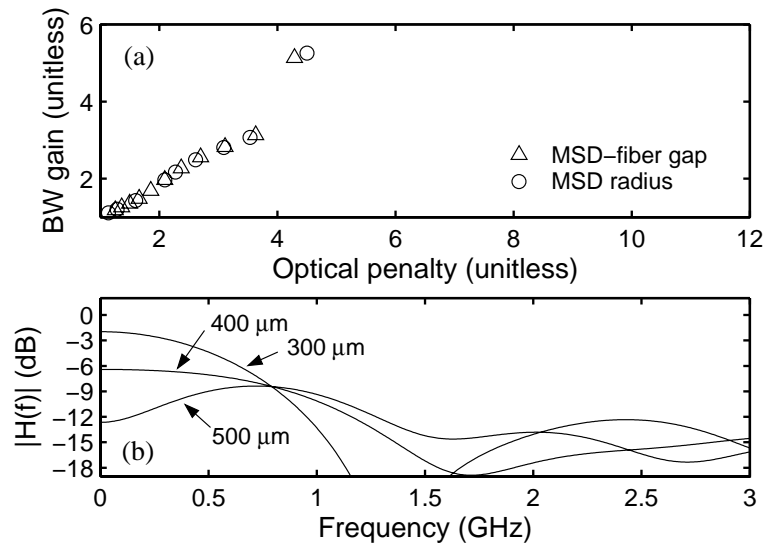


Figure 2.18: (a) Improvement in MMF bandwidth with SRE versus optical loss (in Watts/Watts). (b) Frequency domain response of equalized link for MSD at various distances from fiber: 300, 400 and 500 μm .

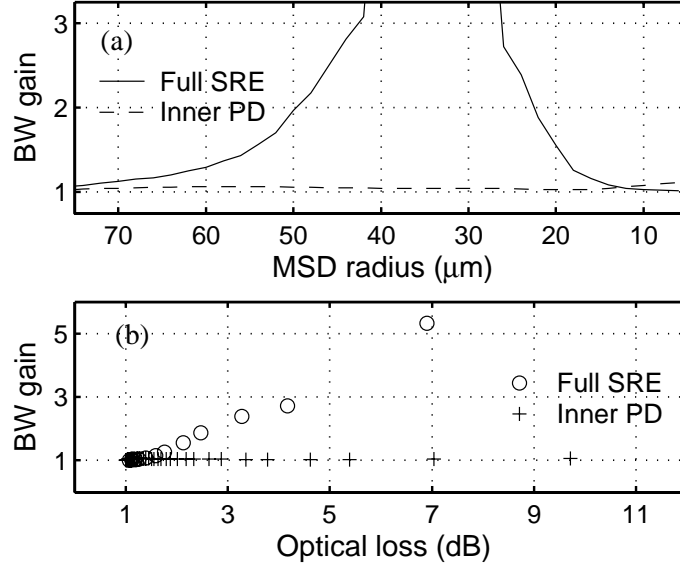


Figure 2.19: Comparison of bandwidth gain with high-ordered mode suppression due to partial detection (Inner PD) versus SRE with subtraction of the outer PD photocurrent (Full SRE). (a) Measured bandwidth gain versus MSD radius. (b) Correlation between optical SNR penalty and bandwidth gain.

2.2.4 Advantage of the two-segment photodetection

Suppression of the high-ordered mode by subtraction of the outer PD signal from that of the inner PD offers a simplicity that is synergistic with MMF. However, an even simpler method of suppressing high-ordered modes may be by the use of only the inner PD signal. With a range MSD sizes bandwidth enhancement via just the inner PD segment is compared to that of the full use of two-segments.

Shown in Fig. 2.19(a), only a limited improvement in bandwidth achieved with only the inner PD signal. This indicates that complete suppression of the HOM is achieved only with subtraction of the residual signal detected by the outer PD. This is supported by Fig. 2.19(b), where despite strong attenuation of the received signal, a limited $1.2\times$ gain in fiber bandwidth is achieved: as the inner PD becomes smaller, the selectivity between LOM and HOM becomes less and all modes become strongly attenuated.

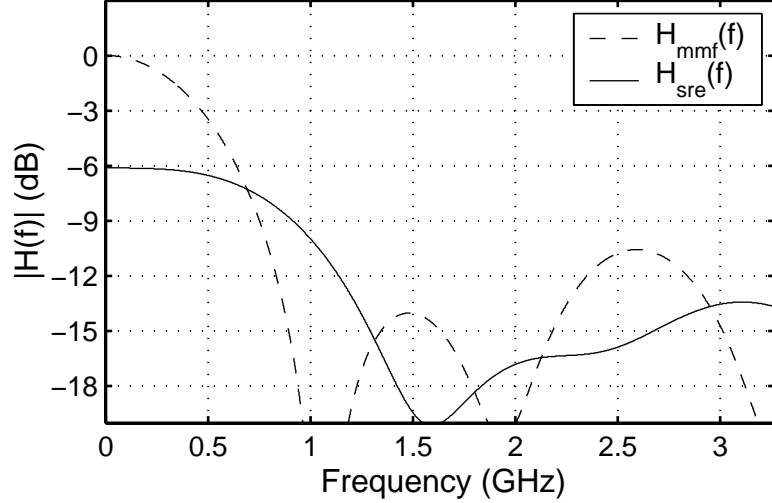


Figure 2.20: Use of multisegment PD in near-field with 15- μm MSD.

2.2.5 Use of SRE in the near-field

Simulation with 55- μm MSD is chosen to maintain compatibility with yet-to-be-presented experimental measurements. However, other factors, namely minimizing detector capacitance, may necessitate a smaller MSD. Moreover, it may be required for some applications that near-field detection, where the MSD may be in near-direct contact with output facet of the optical fiber, is required. In which case, the relative diffraction of the fiber modes may be of significant, Fig. 2.5.

Fortunately, modelling results, shown in Fig. 2.20, verifies that a smaller, 15- μm multisegment photodetector in the near-field performs as well as the 55- μm MSD does in the far-field. This suggests that SRE is not restricted by far or near-field consideration. Though because of the fiber core size, the overall PD size will be limited to 20–25 μm without the use of additional optics.

2.2.6 Monte Carlo link simulations

It is well-known that the impulse response of a MMF link is highly stochastic. These variations are due to not only the inherent variation in the fiber itself but variation in the

spatial relationship between fiber and transmitter. To evaluate the robustness of SRE to any randomness in the fiber link, a Monte Carlo analysis is performed. Maintaining the fiber parameters, the link bandwidth is computed for fluctuation in launch conditions that might incur due to the variability in OE packaging. Relative to the fiber, the VCSEL’s transverse position, tilt angle, modal power, and distance, are randomized, and the resulting coupling coefficients are computed. To restrict the perturbations to reasonable levels, only launch conditions that result in an aggregate power coupling, *i.e.* $\sum_{m=1}^M \rho_m$, better than 3-dB are used. For the chosen parameter variations, summarized in Table 2.2, 98% of the simulated fiber links meet this requirement.

A 5000-trial Monte Carlo simulation is performed on the fiber link; shown in Fig. 2.21 and 2.22 are the histogram of MMF fiber link bandwidth with and without SRE. The mean bandwidth of the fiber link is 577 MHz-km, higher than the single link case, however is still close to the nominal fiber bandwidth. The standard fiber link shows a worst-case bandwidth of 413 MHz-km—minimum bandwidth of 99% of the simulated link. With SRE, however, both mean and worst-case bandwidth improve by 2× with respect to their non-equalized counterparts. The robustness of SRE is demonstrated, in the context that no link-by-link adjustment is made to the equalization.

Regarding the optical penalty, the simulation results, shown in Fig. 2.23, clearly indicate an average optical penalty <3 dB; however, worst-case loss is approximately 9 dB. These cases are the link where majority of the power is coupled to the high-ordered modes. On the other hand, majority of these highly penalized links also exhibit very high enhanced bandwidth as well, shown in Fig. 2.24.

Table 2.2: Statistics of simulated VCSEL parameters.

Parameter	Nominal	Standard Dev	Units
X,Y transverse offset	0	5	μm
X,Y tilt angle	0	2	degrees
Fiber-VCSEL gap	100	10	μm
Modal power	1	0.1	

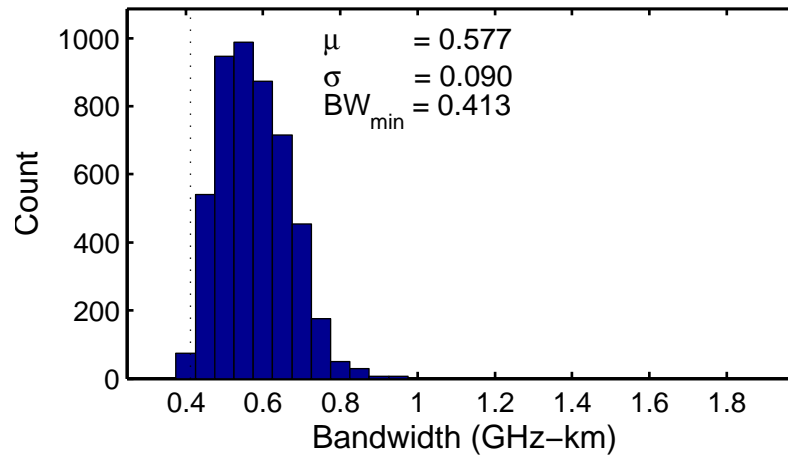


Figure 2.21: Histogram of fiber bandwidth with varying optical launch condition (5000 trials). Launch condition influenced by varying tilt and transverse position of VCSEL relative to MMF.

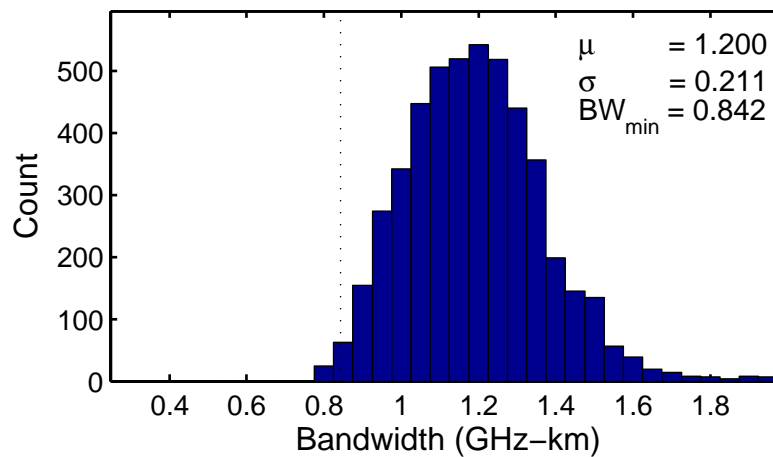


Figure 2.22: Histogram of link bandwidth with spatially resolved equalization.

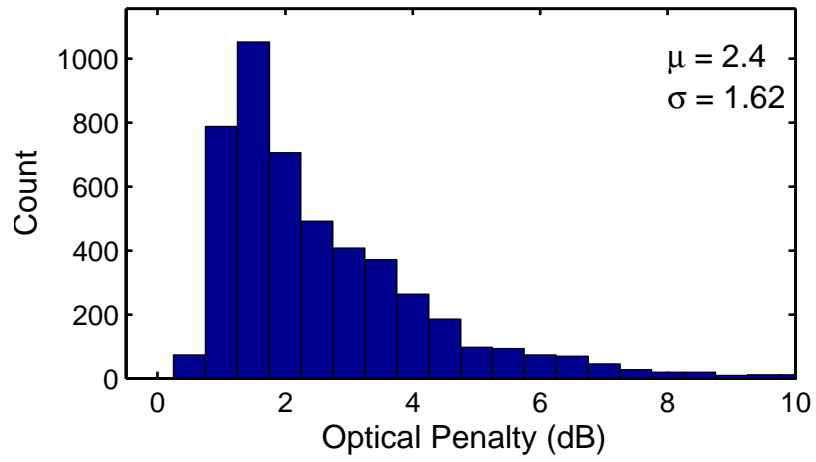


Figure 2.23: Histogram of optical penalty with spatially resolved equalization.

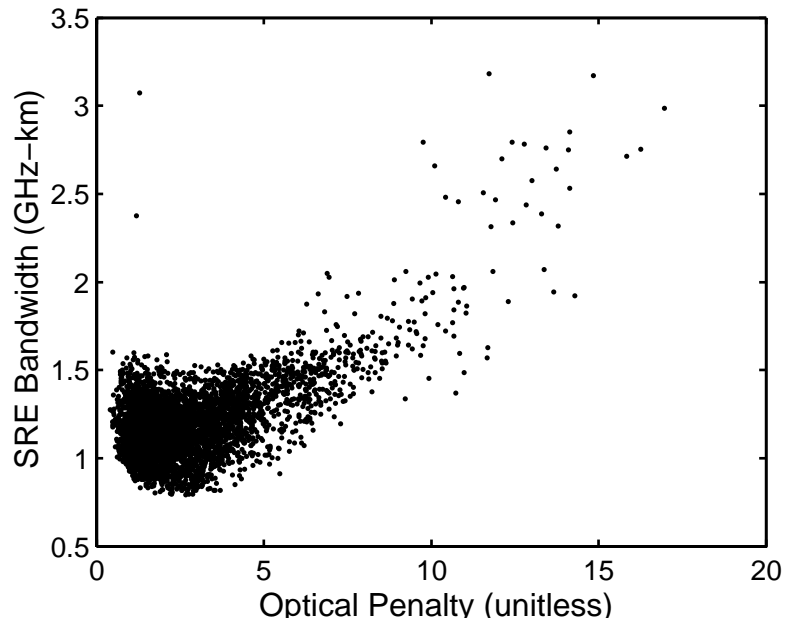


Figure 2.24: Correlation between optical penalty and equalized fiber bandwidth.

2.2.7 Compatibility of SRE with other MMF design

2.2.7.1 Legacy 62.5- μm core MMF

While 50- μm fiber is more common for new fiber installation, many legacy fiber networks utilize 62.5- μm MMF. In addition to the large core diameter, 62.5- μm MMF possesses a larger index contrast, *i.e.* $\Delta = 0.2$; therefore, a large dispersion should be expected. The expected bandwidth from the 62.5- μm MMF is 200 MHz-km. The same MSD geometry is used for the simulated 62.5- μm MMF link. However, to account for the change profile size a smaller diffraction length of 300- μm is used.

Clearly, the larger fiber core-size will result in a change in the number of modes, as well as the relative intermodal dispersion. Shown in Fig. 2.25 is the fiber impulse response showing a bandwidth of 298 MHz-km, nearly half of the 50- μm core fiber. However, as with the 50- μm core, the equalized response, a 2 \times gain in fiber bandwidth is achieved with SRE with a 3.2-dB loss to the optical power, shown in Fig. 2.26. As should be expected, no significant group delay related dependence is observed with spatially resolved equalization.

2.2.7.2 Step-index fiber

For data transmission rates exceeding 1 Gb/s over hundreds of meters of link lengths, the use of graded-index fiber is clear, shown in Fig. 1.3. However, compared to copper cable, optical fiber offers advantages other than bandwidth and low-loss. Issues such as size, weight, crosstalk, radiation hardness, and security may supersede bandwidth considerations. These applications may include integrated-circuit and computer backplane interconnect, lightweight communication equipment as in orbiting satellites, or communication in harsh conditions such as military environment, industrial reactors and automotive engines. For these applications where distances are short or data rates are low step-index fiber may be ideally suited. The use of SRE with a 50- μm step-index fiber is considered in simulation. Fiber parameters listed in Table 2.1 are used; however the step-index is modelled as a graded-index fiber with $\alpha = 10000$.

By virtue of the step-index core profile, the evanescent boundary of the mode profile is

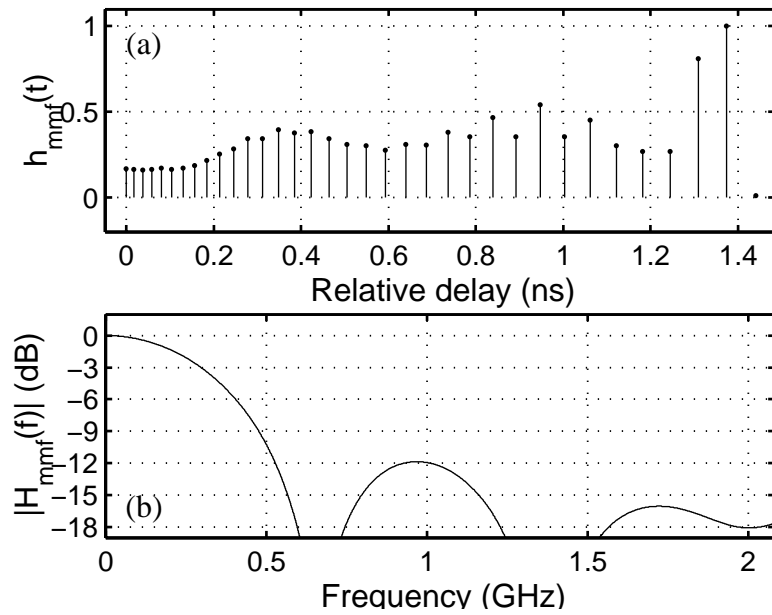


Figure 2.25: (a) Impulse response of 62.5- μm core MMF, with VCSEL-like optical source. (b) Frequency response.

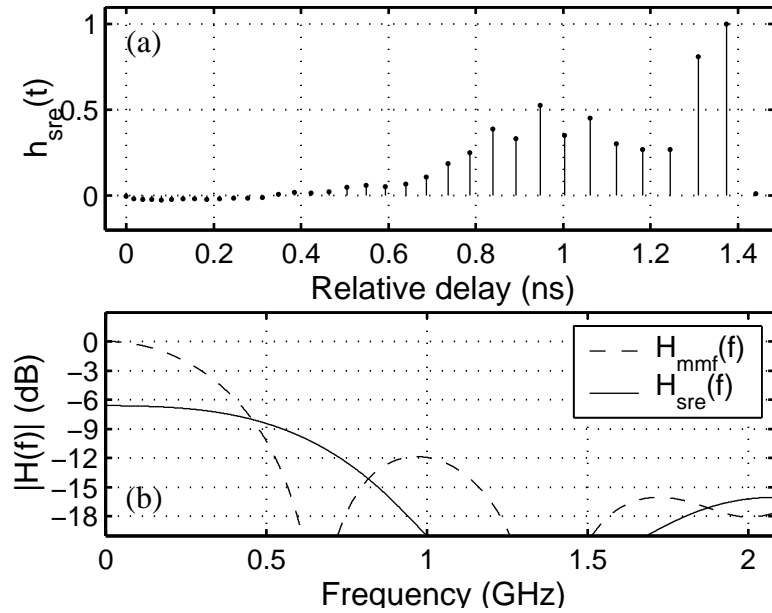


Figure 2.26: (a) Impulse response of equalized 62.5- μm MMF. (b) Frequency response.

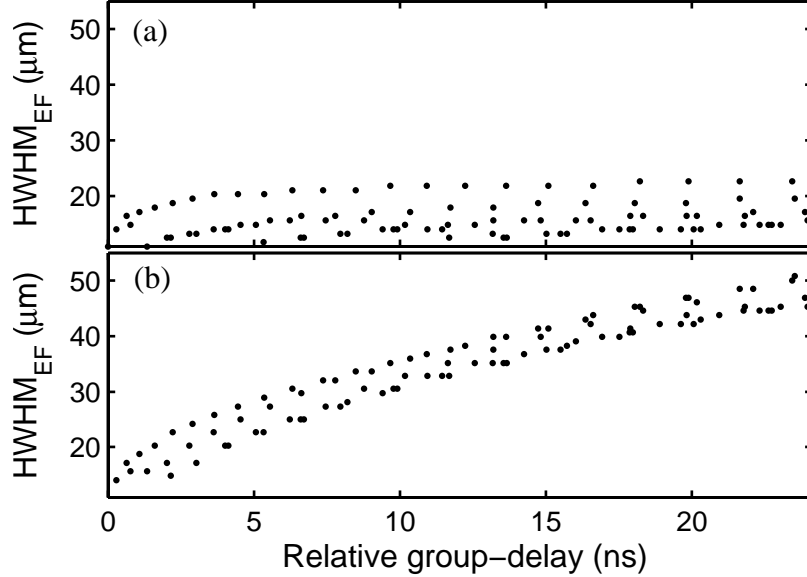


Figure 2.27: (a) Mode-field size in the near-field versus modal group delay for step-index fiber modes. (b) Mode-field size in far-field.

the same of all modes. And to first-order approximation, the mode-field radius is uniform for all modes. Indeed, the encircled-flux in the near-field reflects this, shown in Fig. 2.27(a). Consequently, the embodiment of SRE studied is unsuitable for use in the near-field of step-index fiber.

On the other hand, in step-index fiber, both the group velocity and diffraction angle are strongly coupled to the grazing angle of the mode waves with respect to the core-cladding interface; however, so is the diffraction angle of each fiber mode [50]. Computation of the diffracted mode profile, by the (2.24) and (2.25), shows that in the far-field the desired monotonic relationship between EF and group delay is present, shown in Fig. 2.27(b), indicating that spatially resolved equalization is, indeed, applicable to step-index fiber, under limited circumstances.

2.2.7.3 "Improved" fiber profile

Recall that the optimal profile parameter α minimizing intermodal dispersion by balancing the effective path length with group velocity among the fiber modes. As manufacturing

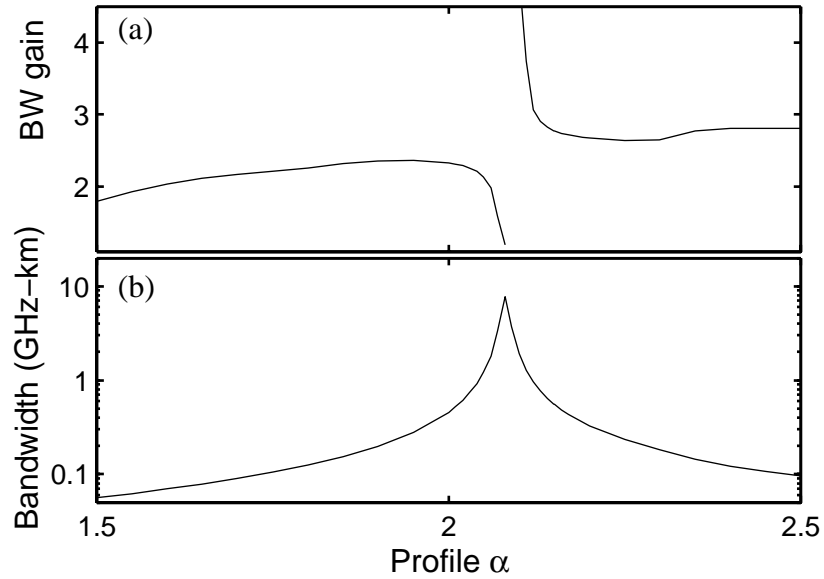


Figure 2.28: (a) Equalization gain for various α profiles. (b) Inherent fiber bandwidth with conventional detection.

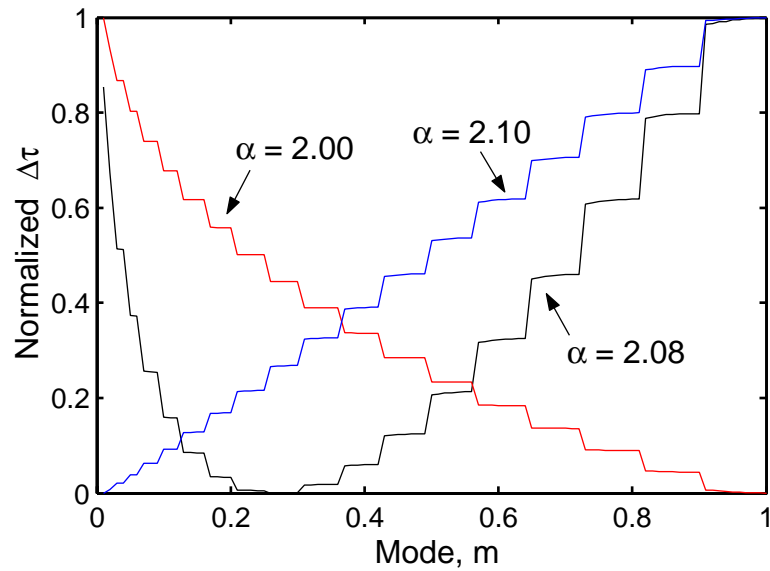


Figure 2.29: Modal group delay for fiber near optimal core profile. Mode number is normalized to total mode number. group delay is normalized by maximum relative delay.

technology matures, the fiber index profiles are being more tuned for optimal performance at specific wavelengths; however, this may restrict high-speed data communication at other wavelengths. The use of SRE with fibers of various index profile is considered. With a fixed link parameter, SRE enhancement on fiber bandwidth for a range of fiber α is computed and plotted in Fig. 2.28(a).

Over a significant range of α , spatially resolved equalization is relatively insensitive to core profile; the intended $2\times$ bandwidth gain is achieved regardless of the index profile. However in a narrow range, near optimal α for the laser wavelength, a sensitivity to α is observed. This results from the strongly non-monotonic, second-ordered effects of m on $\tau(m)$, shown in Fig. 2.29. Useful equalization is precluded by the use of a multisegment PD and simple photocurrent subtraction. However it should be noted, that because of the inherently low intermodal dispersion in this range, shown in Fig. 2.28(b), additional dispersive effects that were neglected in this simulation may dominate, obviating the need for any *intermodal dispersion* compensation.

2.2.8 Robustness of SRE over wavelength

It is the availability of VCSELs that makes this wavelength attractive. As VCSEL technology matures, however, MMF links at 1300 and 1550 nm may become common. Simulation of SRE enhancement over a range of α , shown in Fig. 2.28, implies wavelength independence; nevertheless, a 1550-nm based optical link is simulated.

With regards to the effect of wavelength on intermodal dispersion, a change in the total dispersion is observed. Whereas at the fiber bandwidth at 850-nm is nominally 500 MHz-km, at 1550-nm the fiber bandwidth is 170 MHz-km, a significant difference. Moreover an inversion in the relative arrival times in the modes occurs. Instead of the HOM leading the LOM, at 1550 nm, it is the LOM that lead. But, a monotonic relationship between group delay and mode-field size is still maintained, shown in Fig. 2.30. A change slight change in mode-field size and diffraction is expected as well; however, the simulation shows that the same 55- μm MSD placed at 400- μm from the fiber output results in similar SRE enhancement as at 850 nm, shown in Fig. 2.31. SRE improves the fiber bandwidth by

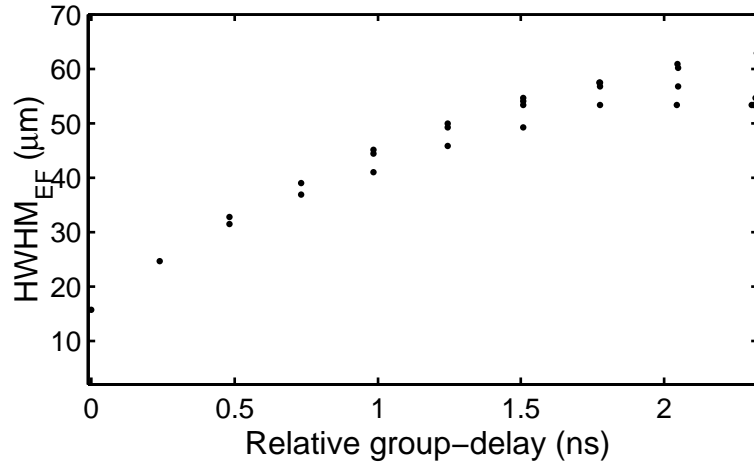


Figure 2.30: Mode-field size in the far-field—400 μm from fiber—for 1550-nm propagation in 50- μm MMF.

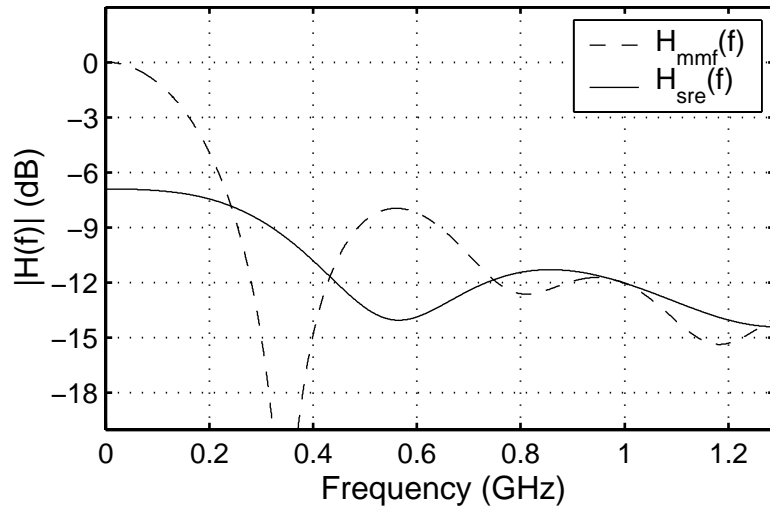


Figure 2.31: Frequency response of MMF equalized with 55- μm MSD in the far-field. Wave propagation at 1550 nm.

2.1 \times . It might be expected that a change in MSD or diffraction length is required for the new wavelength. However, it appears that a simultaneous increase in mode profile and wavelength requires that no significant change in MSD be made. This observation is also supported by the fact that numerical aperture, which is closely related to divergence angle, remains constant for both wavelength.

2.2.9 Alignment tolerance of SRE

By virtue of the plurality of modes, multimode fiber offer high tolerance to misalignment between optical source and fiber. This is the most significant feature of MMF in regards to cost-efficiency. In order to maintain this, the alignment tolerance of the MSD must be comparable.

Using the basic link simulation methodology, detection efficiency η_{pm} is computed with various transverse misalignment of the fiber axis with the far-field MSD. The resulting gain in bandwidth, over the standard fiber link, is computed. For all cases, the standard MMF link is assumed to be unaffected by the detector alignment.

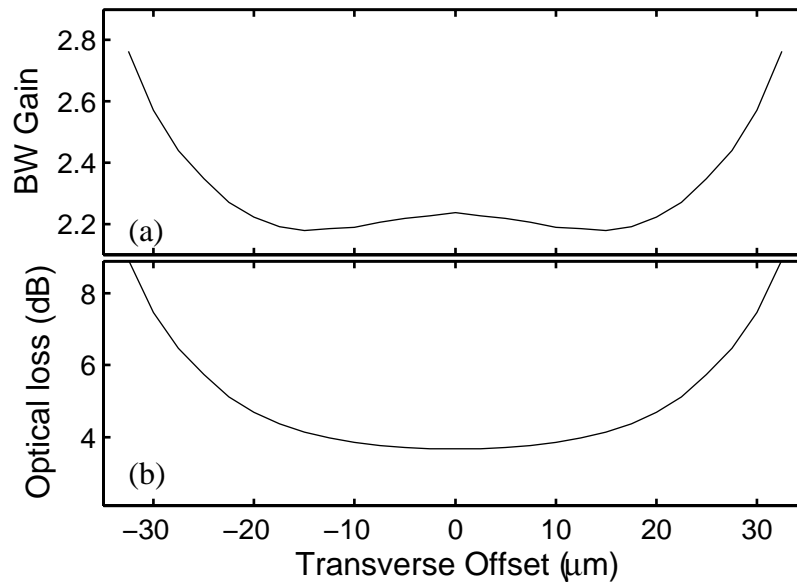


Figure 2.32: (a) Bandwidth gain and (b) optical power penalty of equalized fiber with transverse offset between fiber axis and 55- μm MSD.

The nominal bandwidth gain of $2\times$ is maintained over a $\pm 20\ \mu\text{m}$ offset, a range comparable to the fiber core radius, shown in Fig. 2.32(a). The bandwidth gain increases with further transverse offset; however, it does so with an increased optical penalty, shown in Fig. 2.32(b). Indeed, it is with a similar correlation between BWG and η_{SRE} as previously observed in Fig. 2.19(b).

2.2.10 Equalization with restricted launch conditions

Up to this point, the MMF link is assumed to operate with a large-area VCSEL that will excite majority of the fiber modes. However, it is possible that a more restrictive mode launch can be used where the optical signal is coupled into a few fiber modes, minimizing the impact of the avoiding multipath environment.

This restricted mode launch (RML) condition is typically used at 1300-nm where an edge-emitting laser is coupled to a singlemode fiber which is then optimally aligned with the MMF. Similarly, an encircled-flux specification is used for VCSELs at 850 nm to minimize the number of modes excited. With RML, a $2\times$ improvement in link bandwidth is has been demonstrated [35], but such improvement is not assured. A defect in the fiber core may result in strong intermodal coupling resulting in many modes excited with the optical signal, despite the input coupling condition. Moreover, bandwidth gain from this SMF-to-MMF coupling can be sensitivity to alignment. Experimental and simulation results show a narrow $\pm 5\ \mu\text{m}$ tolerance [35]. For optical links where RML is used, the additional use of SRE can provided cooperative benefits. By limiting mode excitation to low-ordered modes at the fiber input, and suppresses mode contribution of the high-ordered modes at the output, variation due to limited manufacturing tolerances can be minimized.

The optical source is modelled as a Gaussian irradiance profile with a uniform phase front and of varying spot size and offset relative to the fiber axis. Under each launch condition, the link impulse response is computed with and without SRE. The resulting link bandwidths are compared with the standard, VCSEL launch condition. Defects typically observed in real fiber, at the core center, are believed to be responsible for the experimental observation that optimal bandwidth is achieved with optical spot aligned offset from the

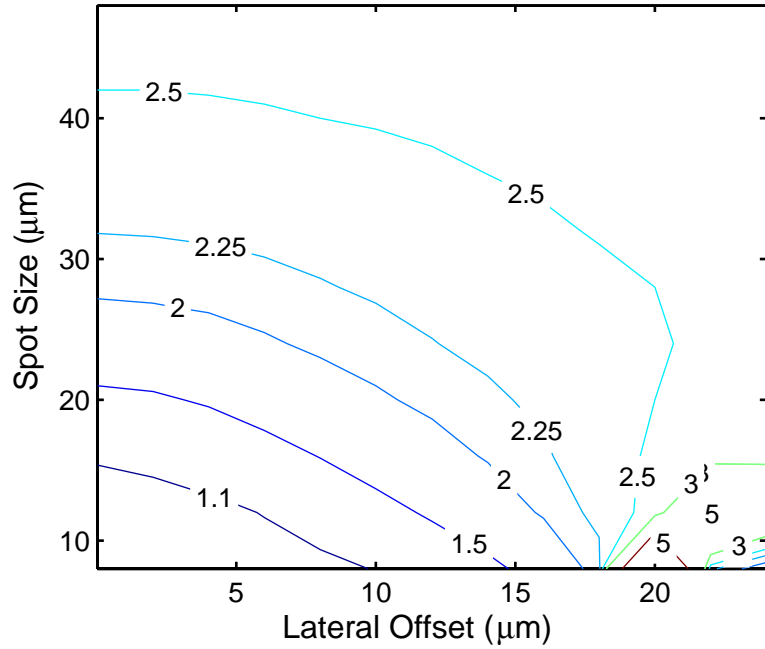


Figure 2.33: Bandwidth gain by SRE for various launch conditions: Gaussian source illumination with uniform phase front. Bandwidth compared on a launch-by-launch basis.

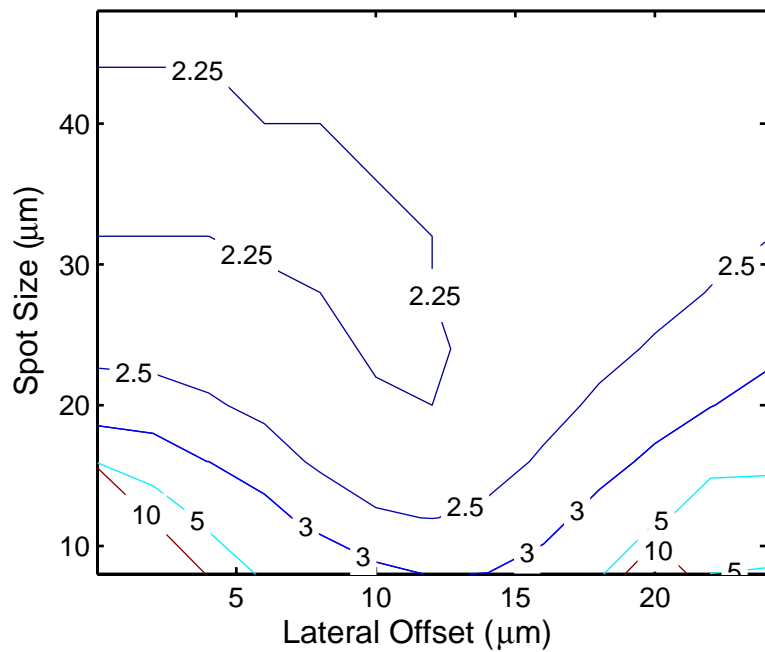


Figure 2.34: Bandwidth gain by SRE for various launch conditions: Gaussian source illumination with uniform phase front. Bandwidth gain compare to standard multimode VCSEL launch.

fiber axis [34]. Therefore, it should be noted that this "centerline dip" is not included in the simulation.

The results presented in Fig. 2.34 shows the combined bandwidth gain by the use of the multisegment PD and RML over that for the basic VCSEL launch MMF fiber. Computing SRE enhancement on a launch-by-launch basis, the results further demonstrates the robustness to SRE under various launch conditions. The SRE bandwidth gain is in addition to that achieved by the launch condition compared to standard multimode VCSEL launch. Only for a select group of launch conditions, where no power is coupled to the HOM, does SRE fail to enhance link bandwidth.

CHAPTER 3

CHARACTERISTICS OF FABRICATED DETECTORS

Multsegmented photodetectors are fabricated for experimental verification of spatially resolved equalization. This chapter discusses some of the mechanics of the photodetectors as well as the motivations for some choices made in the device fabrication. Indeed, SRE is not a photodetection process, but rather a method employing it; no restriction are placed on the photodetection process itself. We choose a metal-semiconductor-metal (MSM) photodetector, but any square-law detector may be used, including *p-i-n* type photodetectors. We present some of the critical characteristics of the fabricated photodetectors.

3.1 Basic photodetection

The standard method of photoreception in lightwave communication links is by the use of semiconductors that are capable of absorbing photons at the wavelength of interest. Incident photons, with energy exceeding the bandgap of the semiconductor, are absorbed by transferring its energy to the electrons in semiconductor lattice. The absorption results in generation of electron-hole pairs (EHP). By applying a electric field across the device, the EHPs are swept out of the semiconductor, resulting in a photocurrent that is directly proportional to the incident photon flux (optical power), shown in Fig. 3.1 and 3.2. To maximize the applied field and minimize dark-current, the semiconductor material is used as a reverse-biased diode. The large electric field applied in reverse bias, allows EHPs to be swept out of the maximum possible speed, thus faithfully replicating any modulation in the incident power.

To maximize performance, semiconductors with high carrier mobility and low bandgap

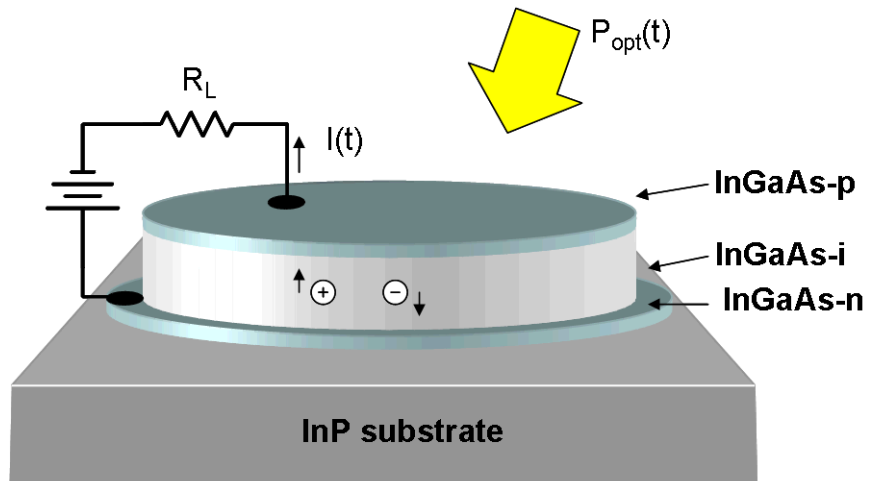


Figure 3.1: Epitaxial *p-i-n* photodiode structure.

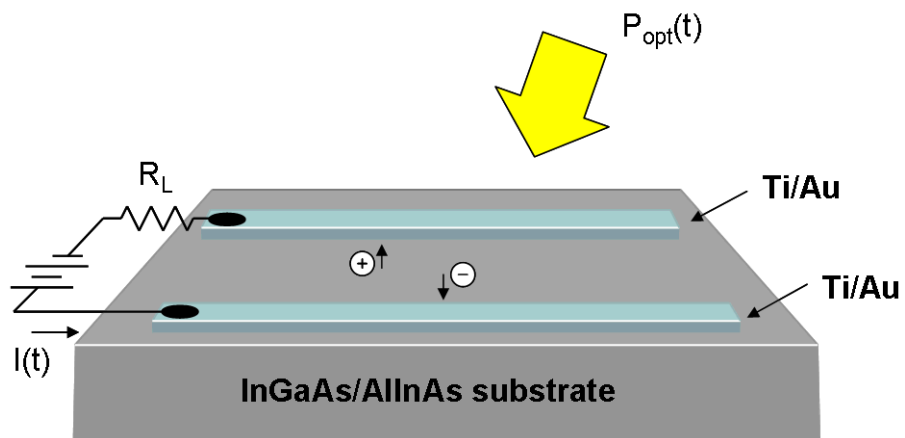


Figure 3.2: Planar MSM photodiode structure.

energy are chosen. For high-speed detection in the wavelength range of 800 through 1600 nm, an InGaAs material system is chosen [51]. While silicon is a less expensive material to use, InGaAs systems has much better carrier mobility and ideal bandgap for detection over the full wavelength band of interest and for data rates approaching 10 Gb/s [52].

Photodiodes are typically made of a stack of *p*-doped (*p*-type), intrinsic (*i*-type), and *n*-doped (*n*-type) layers of semiconductor, [53]. The use of an *i*-type region increases the thickness of the diode, thus reduces the capacitance and increases the volume in which photons are absorbed, shown in Fig. 3.1. To minimize capacitance and minimize carrier transit time, *i*-type region are typical 1–2 μm in thickness.

An alternative to *p-i-n* structure is a metal-semiconductor-metal (MSM) structure, [53]. Two Schottky junctions are created, by the metal-semiconductor contact, and separated by only a few microns spacing. EHP generation is permitted between the Schottky junctions and swept out of the semiconductor by the electric field applied between the Schottky junction, shown in Fig. 3.2. The MSM is readily fabricated on a InGaAs system, where a low-resistance Ti/Au metal layers is deposited to form the diode Schottky barrier. The advantage of MSMs is a simpler, planar fabrication process and significantly lower capacitance per unit area. The temporal response of the MSM is primarily dominated by the carrier transit time between the metal electrodes. Typical electrode spacing is 1–3 μm . The drawback of MSM, however, is the "shadowing" of the incident photons by the metal electrode structure.

An interesting feature of MSM, useful for spatially resolved equalization, is the device symmetry. The circuit model for this structure is two anti-directional diode in series; therefore, either one of the Schottky junctions will be in reverse-bias regardless of the applied voltage polarity. In this way, the polarity of the photocurrent can be manipulated without affecting the PD performance.

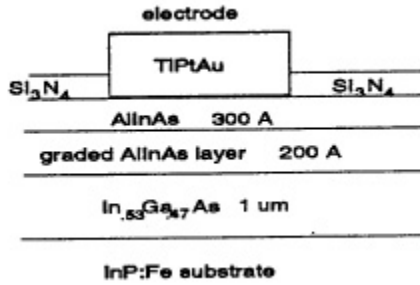


Figure 3.3: InGaAs material system used for high-speed MSM photodetector. Photon absorption in 1- μm InGaAs layer. [51]

3.2 Characteristics of fabricated detectors

For the ease of fabrication and maximum flexibility, MSM-based detectors are chosen for fabrication. Detectors are fabricated on semi-insulating InP substrate with a 1- μm InGaAs absorbing layer. A buried AlInAs layer is included to lower capacitance at the InP/InGaAs interface, and a top AlInAs layer as a Schottky contact layer, shown in Fig. 3.3 [54]. The interdigitated finger of the MSM are 2 μm in width, spaced by 3 μm . The electrodes used are opaque layers of metal, so up to 40% of the photons will be lost due to finger shadowing. In practice, solutions exist to minimize this loss including the use of transparent electrodes or an inverted-MSM which maximized collection efficiency by illuminating the detector from the back [55], [56]. However, for testing, standard top-illuminated MSMs are used.

An arrangement of concentric, circular PD segments are used. The basic structure of the two-segment MSM is shown in Fig. 3.4. The two-segment PD is an integrated device formed by a shared electrode structure. The salient feature of the MSD is the radius of the inner PD detector. A number of devices are fabricated of varying inner PD sizes—25 to 65 μm in radius. The interdigitated structure of the MSM limits the radius of the inner PD to $>10\mu\text{m}$, if circularity is to be maintained. The outer radius of all photodetector is 100 μm to ensure all optical power is collected. In this regard, all MSD will subsequently be parameterized by the radius of the inner PD segment.

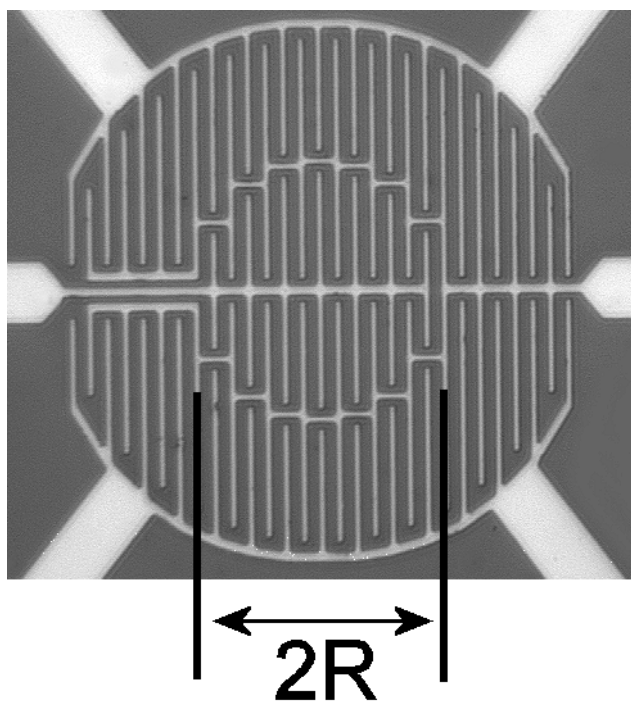


Figure 3.4: Microphotograph of fabricated multisegment detector

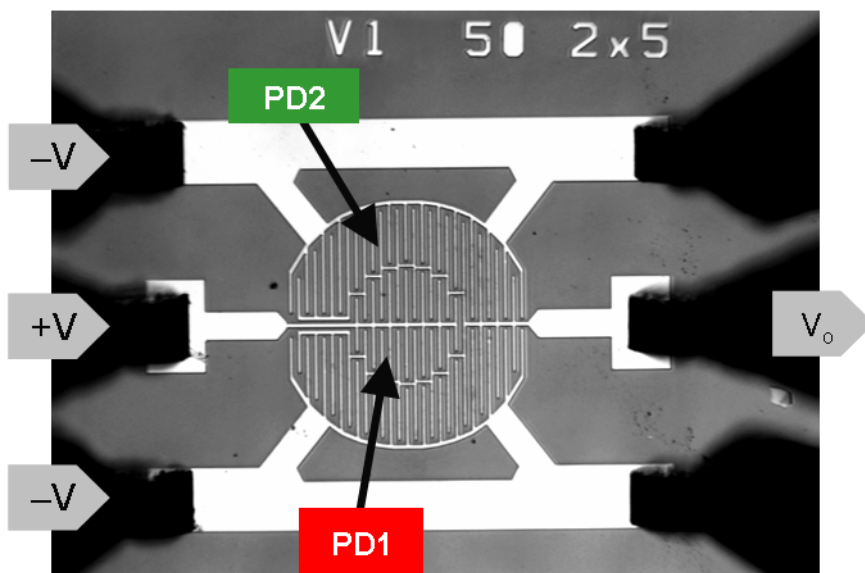


Figure 3.5: On-wafer biasing and probing using 50-Ω RF probes

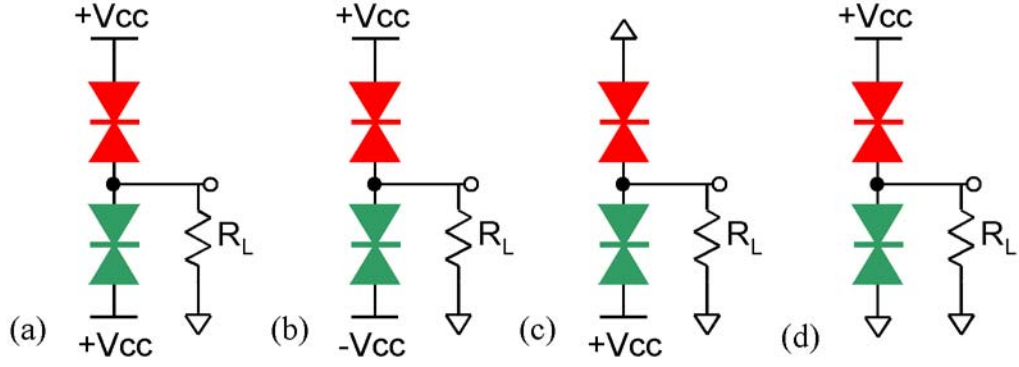


Figure 3.6: Biasing of MSD device. (a) Bias of equal magnitude and polarity applied to MSM for conventional PD. (b) Bias of equal magnitude but opposite polarity applied to MSM to subtract outer PD photocurrent from that of the inner PD. (c) Required PD configuration and bias for SRE with *p-i-n* diodes.

The devices are fabricated for on-wafer probing, shown in Fig. 3.5. The output photocurrent is collected at the shared electrode. Standard 40-GHz 50- Ω on-wafer probes are used to couple the photocurrent directly into 50- Ω terminated test instruments. To protect the instruments from unnecessary power dissipation, the signal is AC coupled to the instruments via a 30-MHz to 18-GHz bias-tee. Appropriate bias of the MSM segment can be applied through the 50- Ω probes in a number of ways, using a combination of independent, voltage sources.

3.2.1 MSD biasing

With the two-segment PD, spatially resolved equalization is achieved by subtraction of the two PD signals with unit magnitude scaling. Because polarity of photocurrent is related to the polarity of bias, subtraction of two PD signals is easily achieved by applying a bias of equal magnitude but opposite polarity, shown in Fig. 3.6(b). Moreover, the same device can be used as a conventional PD with identical bias applied to both segments, shown in Fig. 3.6(a). Finally, the photocurrent of each individual segments may be measured. By applying zero bias to one segment, the resulting photocurrent is that of the other, shown in Fig. 3.6(c) and (d).

3.2.2 MSD I-V curve

Current-voltage (I-V) transfer function is measured for the device under various illumination, shown in Fig. 3.7. With no illumination, a dark current of 40 nA is measured. For illumination at 1550-nm, increments in optical power of $50\mu\text{W}$ results in increments in photocurrent by $10\mu\text{A}$, corresponding to a responsivity of 0.2 A/W. This is $4\times$ less than the typical 0.8–0.9 A/W typically achieved with commercial *p-i-n* detectors. A reduction factor of $2.8\times$ can easily be attributed to finger shadowing and Fresnel reflection. The remaining reduction factor may be the result of the thin absorbing layer of the InGaAs structure.

Similar measurement made at 810-nm result in 0.15–0.18 A/W responsivity. Typical commercial devices exhibit 0.4 A/W responsivity. A reduction in responsivity, compared to operation at 1550-nm, is expected since only one EHP is generate per 850-nm-photons despite nearly $2\times$ energy compared to a 1550-nm photon. However, a near equivalent responsivity observed in measurement, between 1550-nm and 800-nm, suggest a wavelength dependent quantum efficiency. Since finger shadowing and Fresnel reflection are comparable at the two wavelength, a change in absorption of the InGaAs is indicated. Either an increase in the absorbtion coefficient or unintended absorbtion of other device layers, such as the AlInAs Schottky layers.

3.2.3 MSD device capacitance

Regardless of the polarity of bias between the PD segments, the PD capacitance is determined by the electrode spacing and PD area. While the individual PD segments may be of disparate sizes, the manner in which the photocurrents are combined, the total capacitance is the net sum of the PD segments areas. Since the total area remains the same, the final device capacitance is independent of inner PD sizes. Shown in Fig. 3.8 is result of 1-port scatter parameter measurements made on a sample MSD. A simple parallel resistor-capacitor model is used for the PD, and the parameters are optimized to match measurements. The corresponding device capacitance is 0.266 pF.

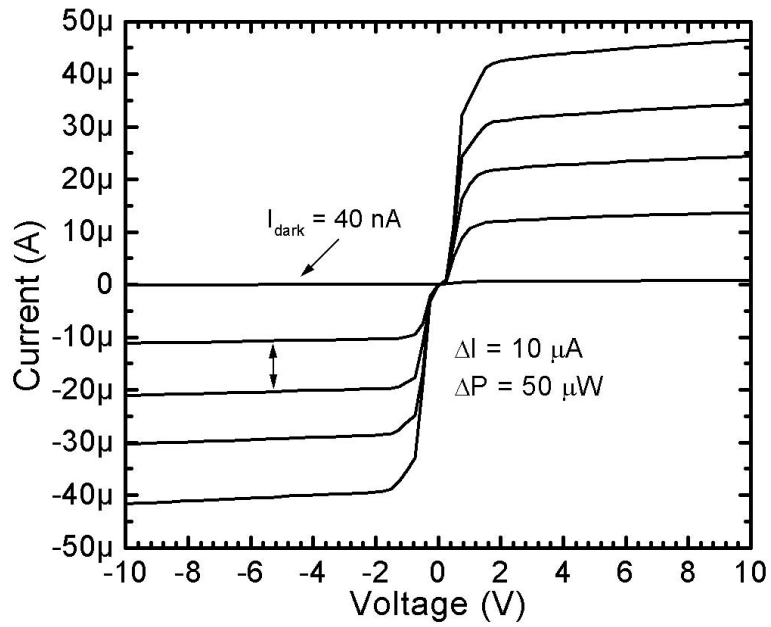


Figure 3.7: Current-voltage transfer curve of interdigitated MSM under various illumination power.

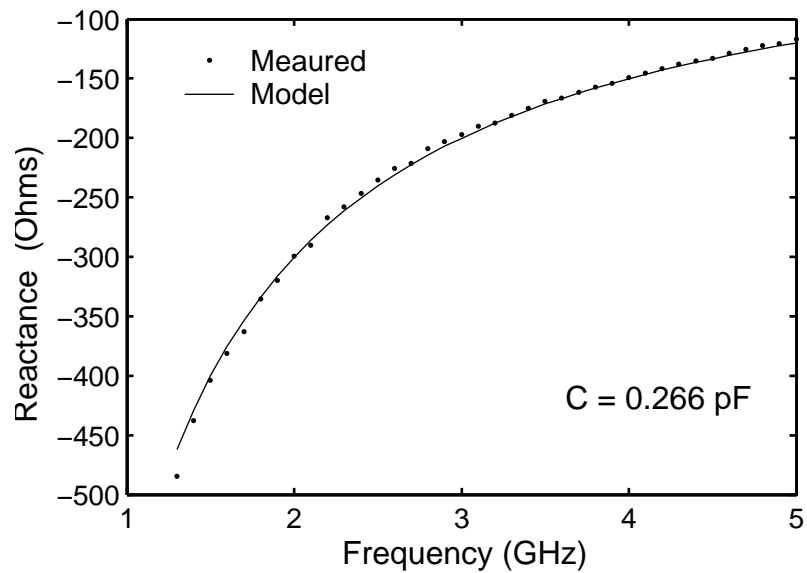


Figure 3.8: Device reactance computed from measured 1-port scattering parameter.

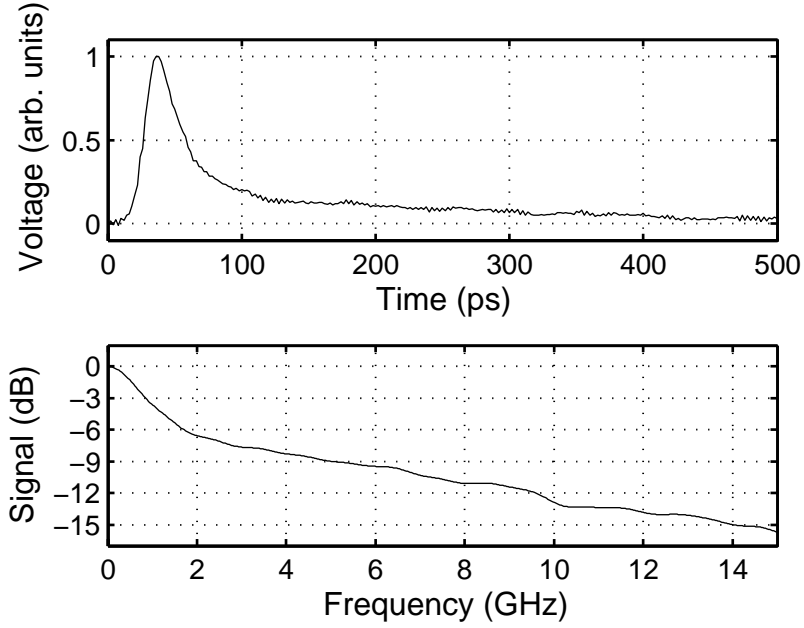


Figure 3.9: Measured impulse response and computed frequency response of 200- μm MSD at with 1-ps at 1550-nm. Main peak width of 35-ps, low-frequency tail width of 400 ps.

3.2.4 MSD impulse response

Impulse response is also measured. The response of the 200- μm photodetector to a 1-ps, 1550-nm optical pulse is recorded and shown in Fig. 3.9. The FWHM of the main peak is 35 ps. The frequency response is determined by computing the Fourier transformation of the temporal signal. The frequency response, however, shows a 3-dB cutoff frequency of 0.9 GHz, dominated by the low-frequency tail seen in the temporal response. For the main peak, however, the 3-dB cutoff frequency is approximately 7.1 GHz.

3.3 Noise analysis

Before proceeding to the analysis of spatially resolved equalization on the impulse response of multimode fiber, its impact on signal-to-noise ratio should be considered. In any system, the magnitude of the signal is only significant in the context of the underlying noise.

Four sources of noise are considered: *shot noise*, *Johnson or thermal noise*, *relative*

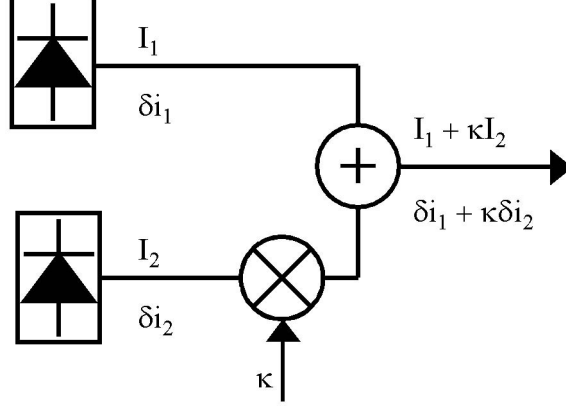


Figure 3.10: Circuit model for noise injected, either optically or electronically, prior to signal recombination.

intensity noise (RIN), and *modal noise*. Of these noise sources, it will be shown that neither shot noise nor RIN is affected by SRE in any significant way. On the other hand, it will be shown that modal noise and thermal noise can increase due to the use of a multisegmented photodetector. It will also be shown that under certain circumstance, there is no fundamentally higher limit on the noise compared to a conventional photodetector.

For the analysis, an ideal two-segment photodetector is assumed, where all optical power emitted by the fiber is incident either one of the segments. Moreover, all PD segments are assumed to have uniform photodetection efficiency. Without loss of generality, the noise power is assumed to be injected into the signal prior to combining photocurrents,

$$N = \int_T (\delta i_i + \kappa \delta i_2)^2 dt \quad (3.1)$$

where δi_1 and δi_2 is the noise current of the two PD segments respectively, and κ is the scaling factor prior to recombination, shown in Fig. 3.10. Regardless of noise source, we assume that δi_1 and δi_2 have a zero mean, *i.e.*

$$\int_T \delta i dt = 0, \quad (3.2)$$

and electrical power N given by

$$N = \frac{1}{T} \int_T \delta i^2 dt. \quad (3.3)$$

We restrict subsequent discussion to either the conventional detection, where $\kappa = 1$, or SRE, where $\kappa = -1$. Consequently, the total noise power N_o , of the combined signal, is given by

$$N_o = N_1 + N_2 + \frac{2\kappa}{T} \int \delta i_1 \delta i_2 dt, \quad (3.4)$$

Clearly, the relative noise between conventional and SRE detection will be related to the covariance of the noise, *i.e.* $\text{Cov}(\delta i_1, \delta i_2)$, between the two PD segments.

3.3.1 Shot noise

Shot noise is the fundamental noise associated with the stochastic arrival and optoelectronic conversion of photons. It exhibits the statistics of Poisson white noise and is given by

$$N_{shot} = 2e|I|. \quad (3.5)$$

where e is electron charge. It is a process acting independently on each photon, thus independently on δi_1 and δi_2 as well. For shot noise,

$$\text{Cov}(\delta i_1, \delta i_2) = 0 \quad (3.6)$$

and the total noise power for shot noise, regardless of the way photocurrents are combine, is given by $N_1 + N_2$.

3.3.2 Relative intensity noise

Relative intensity noise is random photon generation, resulting from the spontaneous emissions within the laser gain medium. This results in a fluctuation in power

$$P(t) = P_o(t) + \delta P(t). \quad (3.7)$$

Indeed, it is by definition that $\delta P(t)$ is the equivalent power fluctuation necessary to produced the observed photocurrent fluctuation, *i.e.* $\delta i \equiv \delta P(t)$. The variation in the transmitted power of the laser is the results of spontaneous emission in the laser gain, causing random modulation of the carrier phase and amplitude [53]. The resulting field profile in

the fiber will also fluctuate in amplitude. If we let γ be the fraction of the available power that is incident on PD1, the power incident on each PD segment will be given by

$$P_1(t) = \gamma P_o(t) + \gamma \delta P(t), \quad (3.8)$$

and

$$P_2(t) = (1 - \gamma) P_o(t) + (1 - \gamma) \delta P(t). \quad (3.9)$$

As a results, the electrical power of δi_1 and δi_2 will be

$$N_1 = \gamma^2 N_o, \quad (3.10)$$

and

$$N_2 = (1 - \gamma)^2 N_o, \quad (3.11)$$

respectively. Moreover, the covariance is given by

$$\frac{1}{T} \int \delta i_1 \delta i_2 dt = (1 - \gamma) \gamma N_o. \quad (3.12)$$

The combined noise power is thus

$$N_{RIN} = \left[\gamma^2 + 2\kappa(1 - \gamma)\gamma + (1 - \gamma)^2 \right] N_o. \quad (3.13)$$

For the conventional PD, this will result in noise power of N_o , which is self-consistent with the fact that δP is defined by the noise power measured with a conventional photodetector. For the SRE case, the noise power is $(2\gamma - 1)^2 N_o$. This implies noise power due to laser fluctuations can be reduced by the use of a multisegment photodetector; however, it should be kept in mind that with SRE, the signal power also reduces by $(2\gamma - 1)^2$. Consequently, there is no meaningful change in signal-to-noise ratio, regardless of detection, with respect to RIN.

3.3.3 Johnson noise

Johnson noise, or *thermal noise*, is additive Gaussian white noise from the Brownian motion of the electrons in any electronics. Thermal noise current is given by

$$\delta i = \sqrt{\frac{4kTB}{R}}, \quad (3.14)$$

where k is Boltzman's constant, T is device temperature, R is the device resistance, and B is the bandwidth. While the PD segment contribute to the noise, we disregard them in light of their large resistance. Instead, we consider only the noise in subsequent electronic components, specifically the use of amplification after photodetection.

Each electronic device produces noise irrespective of each other, therefore δi_1 and δi_2 are independent, and $\text{Cov}(\delta i_1, \delta i_2) = 0$. Assuming amplification before signal combination, the resulting noise power is $2N_1$, where N_1 is presumably the lowest available noise from electronic amplification. However, unlike the other noise source, thermal noise can be avoided prior to signal combination. For a noiseless signal combination process, the output noise power is limited to the noise of only one amplifier, N_1 . In fact, the use of bias based polarity control of the photocurrent permits noiseless signal combination. However, such is not the case with a resistive power combiner, as would be required with a broadband signal.

It is typically the case, in short-haul links such as with MMF, that system noise is strongly dominated by the receiver thermal noise [45]. In order to minimize noise, therefore, the latter case of amplification after noiseless signal combining is preferred, reducing the output noise power by 3 dB.

3.3.4 Modal noise

Specific to multimode fiber is *modal noise*. This noise results from the coherent interaction among the many fiber modes. An obvious manifestation of the coherent interaction is a speckle pattern in the output intensity profile, Fig. 3.14. Modal noise is of concern to all MMF links. However, it is of particular importance to SRE. Noise is generated by the presence of all the following factors: coherent interaction among fiber modes, spatial filtering, and drift in mode propagation due to environmental fluctuations; absence of either of these will prevent generation of modal noise. In a practical implementation, environmentally driven drifts are unavoidable, but in a well-designed MMF link, spatial filtering can be reduced by careful alignment fibers to other fiber and opto-electronic components. If such care is taken, modal noise can be eliminated. On the other hand, by virtue of the segmented photodetector, SRE spatially filters the optical signal; therefore, modal noise

must be managed by judicious choice of source.

Of any square-law detector, photocurrent is proportional to the time-average optical power incident on the PD;

$$P(t) = \frac{1}{2T} \int_T \iint_A \mathbf{E}(x, y, z, t - t') \times \mathbf{H}^*(x, y, z, t - t') \cdot \hat{\mathbf{n}} \, dx dy \, dt', \quad (3.15)$$

where $\mathbf{E}(x, y, z, t)$ and $\mathbf{H}(x, y, z, t)$ are the electric and magnetic fields of the incident wave, A is the surface of the PD, T is the time-average period, and $\hat{\mathbf{n}}$ is a unit vector normal to the PD surface. Assuming time-harmonic wave in a linear, isotropic medium, the relationship between electric and magnetic field is

$$\mathbf{k} \times \mathbf{E}(x, y, z, t) = \sqrt{\frac{\mu}{\epsilon}} \mathbf{H}(x, y, z, t), \quad (3.16)$$

where μ and ϵ are the permeability and permittivity of the medium respectively, and \mathbf{k} is the wave vector of the field. Assuming \mathbf{k} is parallel with $\hat{\mathbf{n}}$, (3.15) is equivalently given by

$$P(t) = \frac{1}{2} \sqrt{\frac{\epsilon}{\mu}} \int_T \iint_A \mathbf{E}(x, y, z, t') \cdot \mathbf{E}^*(x, y, z, t') \, dx dy \, dt'. \quad (3.17)$$

Note that for brevity, $(t - t')$ will be abbreviated as simply t' .

Recall that for the multimode waveguide, the electric field at the end of fiber, *i.e.* $z = L$, is the superposition of a number of fiber modes. For a fiber excited by a single optical source of carrier frequency ω_o and field envelope $\xi(t)$, the output field is given by

$$\mathbf{E}(x, y, z, t) = \sum_m \hat{\mathbf{e}}_m E_m \Psi_m(x, y) \xi(t - \tau_m) \exp(j\omega_o t - j\beta_m L) \quad (3.18)$$

where for each mode: $\hat{\mathbf{e}}_m$ is the field polarization, $\Psi_m(x, y)$ is the transverse profile, β_m and τ_m are the phase- and group velocity, respectively. Without loss of generality, the envelope function is separated into the electric field amplitude E_m and time-variant function $\xi(t)$, which includes signal modulation, noise and excess optical spectrum inherent to the laser. Moreover, only ideal modal group delay is included in (3.18); effects such as chromatic dispersion are disregarded.

The resulting time-average incident power is a sum of terms

$$\hat{\mathbf{e}}_m \cdot \hat{\mathbf{e}}_n \frac{E_m E_n^*}{T} \exp(-j\Delta\phi_{mn}) \int_T \xi(t' - \tau_m) \xi^*(t' - \tau_n) dt' \iint_A \Psi_m \Psi_n^* \, dx dy. \quad (3.19)$$

The relative phase delay between modes $\Delta\phi_{mn} \equiv (\beta_m - \beta_n)L$. Letting the total power incident on the photodetector be defined as

$$P(t) \equiv P_o(t) + \delta P(t) \quad (3.20)$$

The sum of like-terms, *i.e.* $m = n$, is the incoherent interaction among modes, $P_o(t)$;

$$P_o(t) = \frac{|E_m|^2}{T} \sum_m \int_T |\xi(t' - \tau_m)|^2 dt' \iint_A |\Psi_m(x, y)|^2 dx dy. \quad (3.21)$$

And the sum of cross-terms, *i.e.* $m \neq n$, is the coherent part of the modal interaction;

$$\delta P(t) = \hat{\mathbf{e}}_m \cdot \hat{\mathbf{e}}_n \frac{E_m E_n^*}{T} \exp(-j\Delta\phi_{mn}) \int_T \xi(t') \xi^*(t' + \Delta\tau_{mn}) dt' \iint_A \Psi_m \Psi_n^* dx dy, \quad (3.22)$$

where $\Delta\tau_{mn} \equiv \tau_m - \tau_n$. Note that RIN noise, which is not considered for this analysis, is found in the $P_o(t)$ and results comes about by noise in $\xi(t)$.

The presence of the phase term $\exp(-j\Delta\phi_{mn})$ in (3.22) means any drift in β_m with respect to β_n due to environmental conditions will result in a stochastic variant of $\delta P(t)$. Over a few hundred meters of fiber, this is very likely.

For most cases of photodetection, the incident power is assumed to be fully incident on the PD, effectively making $A = \infty$. Recall that the fiber modes are orthogonal to each other [45];

$$\iint_{\infty} \Psi_m \Psi_n^* dx dy = 0, \quad (3.23)$$

for $m \neq n$. Therefore, for the two-segment PD of areas A_1 and A_2 such that all power is incident on either of the PD segments, *i.e.* $A_1 + A_2 \in \infty$,

$$\iint_{A_1} \Psi_m \Psi_n^* dx dy + \iint_{A_2} \Psi_m \Psi_n^* dx dy = 0. \quad (3.24)$$

Consequently,

$$\delta P_1(t) = -\delta P_2(t). \quad (3.25)$$

Likewise, resulting photocurrents between the two PD segments will be perfectly anti-correlated; $\delta i_1 = -\delta i_2$. For the conventional photodetection, where the photocurrents add, the resulting output noise is nil. However, for SRE, where $\kappa = -1$,

$$N_o = N_1 + N_2 + \frac{2\kappa}{T} \int_T -\delta i_1^2 dt, \quad (3.26)$$

or equivalently $N_o = 4N_1$. Whereas for conventional photodetection $N_o = 0$, for SRE the modal power is not only non-zero but 4× bigger than that of either PD segments alone! Fortunately, as will be shown in the next section, there is no fundamental limit on N_1 .

3.3.4.1 Managing modal noise with source coherence

Modal noise can be a significant issue with spatially resolved equalization. However, with judicious choice of the optical source, it can be minimized.

A further examination of (3.22) shows that the cross terms are directly proportional to the estimate of the autocorrelation of $\xi(t)$, the envelope of the signal;

$$R_{\xi\xi}(\Delta\tau_{mn}) = \frac{1}{T} \int_T \xi(t)\xi^*(t + \Delta\tau_{mn})dt. \quad (3.27)$$

Clearly, the power fluctuation is related to the autocorrelation of the optical signal. Thus with an optical source of with coherence time T_c less than $\delta\tau_{mn}$, modal noise will be reduced.

Recognizing that the autocorrelation $R_{\xi\xi}(\Delta t)$ of a signal and its power spectral density $S_{\xi\xi}(\omega)$ are related by the Fourier transform $\mathcal{F}\{\cdot\}$ (Wiener-Khinchin theorem) [18]—

$$S_{\xi\xi}(\omega) = \mathcal{F}\{R_{\xi\xi}(\Delta t_{mn})\} \quad (3.28)$$

—it is clear that the use of optical source with large spectrum will result in low coherent action among modes.

Consider three different type of laser sources: distributed feedback laser (DFB), Fabry-Perot laser (FP) and vertical-cavity surface emitting laser (VCSEL). The distinction between each laser type is the manner in which the laser cavity is constructed. In all three cases, the lasing cavity constructed around a semiconductor gain medium [53].

Both DFB and FP are lasing cavity made of a long, singlemode waveguide [57]. For the DFB, the cavity is formed by Bragg grating structure with a "phase" defect in the center and typical produces a single longitudinal lasing mode of extremely narrow line width [57]. The optical spectrum of a sample DFB is shown in Fig. 3.11. For such narrow linewidth, the autocorrelation may have an extremely large width. Indeed, typical DFB have coherence times of $> 100\text{ns}$.

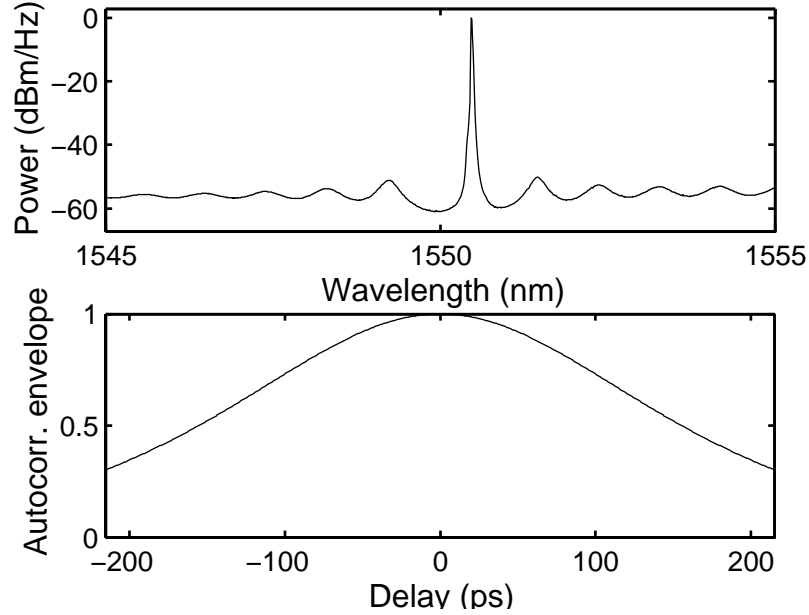


Figure 3.11: Optical spectrum of DFB laser (Agilent 83430A) and computed autocorrelation envelope. Spectrum limited by finite resolution (0.01nm) optical spectrum analyzer. Underlying carrier oscillation in autocorrelation not shown.

In contrast, the cavity of FP laser is formed by the flat cleaved surface at the end of the waveguide producing a Fresnel reflection interface; this wavelength independent reflection allows multiple longitudinal modes to lase [57]. The optical spectrum of a typical FP is shown in Fig. 3.12. The narrow linewidth of each lasing mode ensures coherent interaction for large values of Δt , up to ± 50 ps, but only in very narrow windows of $\Delta\tau_{mn}, < 1$ ps.

Finally, consider the VCSEL cavity. It is a short vertical cavity that is singlemode in the longitudinal direction, but often large enough in the transverse dimension to support multiple transverse lasing modes. Shown in Fig. 3.13 is the spectrum of a typical VCSEL transmitter. The corresponding autocorrelation width is very short, < 5 ps.

Clearly, temporal coherence is of importance, however, the matter of coherence is not limited to temporal. While Fig. 3.11, 3.12, and 3.13 show the autocorrelation, (3.22) is, in actuality, a cross-correlation of the electric field of two fiber modes. To that end, no assurance is yet given to relative polarization among modes: rotation in polarization among

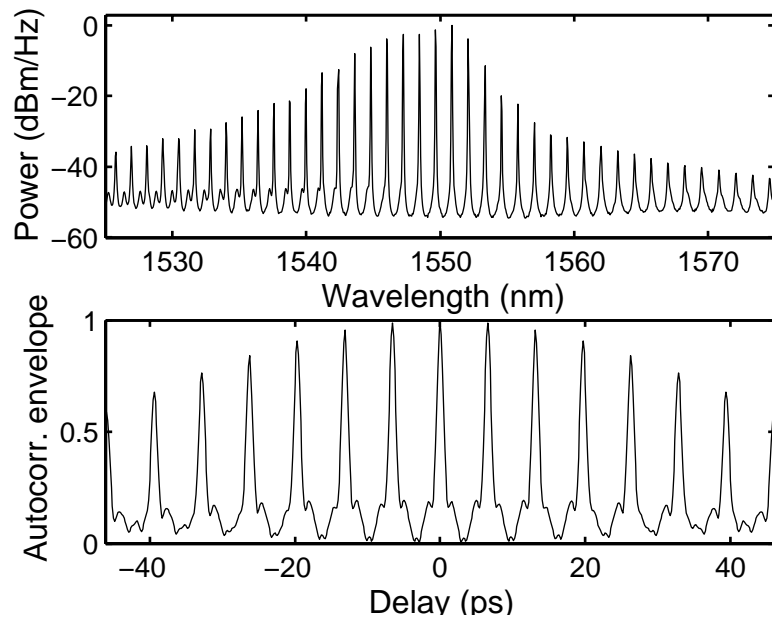


Figure 3.12: Optical spectrum of FP (Agilent 8155A) laser and computed autocorrelation envelope. Underlying carrier oscillation in autocorrelation not shown.

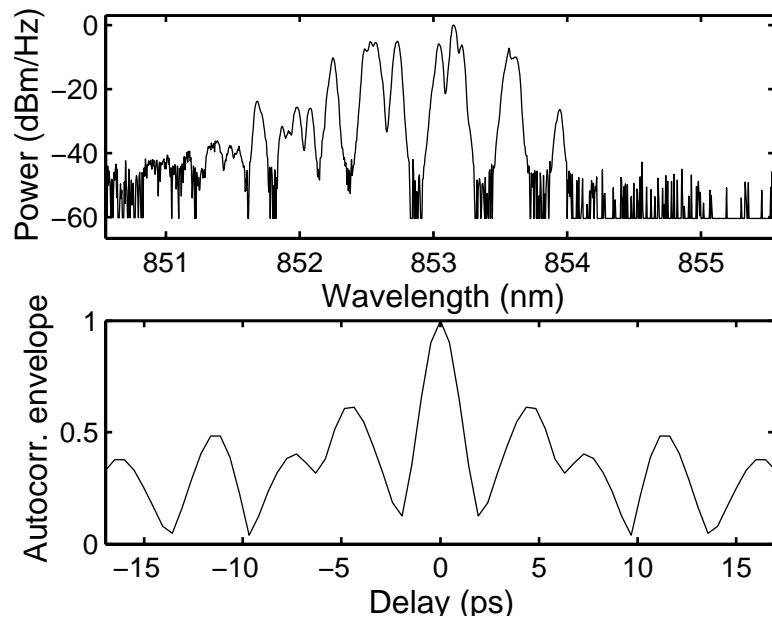


Figure 3.13: Optical spectrum of VCSEL (E2O 10GHz module, EM1052) laser and computed autocorrelation envelope. Underlying carrier oscillation in autocorrelation not shown.

modes will result from the twisting and bending of the fiber in conjunction with any non-circularity in the core profile. Moreover, with multimode VCSEL, often the emitted lasing modes may exhibit disparate polarization. With the $(\hat{\mathbf{e}}_m \cdot \hat{\mathbf{e}}_n)$ term,

$$\delta P(t) \propto \cos \theta_{pol}, \quad (3.29)$$

where θ_{pol} is the difference in linear polarization angle between two modes. Assuming a uniformly distributed random polarization state among modes, the variance in optical power is, therefore, reduced by $1/\sqrt{2}$ and the resulting electrical noise power is reduced by 1/2 [58]. This is, of course, with respect to modal noise inferred solely by the temporal coherence.

The consequences of source coherence can be most clearly observed in the speckle pattern at the output of the fiber. Shown in Fig. 3.14(a) is the speckle pattern of an incoherent LED source at 850 nm. The incoherent emission generates no speckle pattern and is used as a reference speckle due to low coherence. On the other hand, the single mode, extremely narrow spectral width emission of a DFB laser is used as a reference speckle pattern for extremely high coherence, shown in Fig. 3.14(b).

For the Fabry-Perot laser at 1550-nm and VCSEL laser at 850-nm, the contrast in speckle pattern at the output is clearly low. In the case of FP lasers, though the emission is singlemode in the transverse direction, multitude of longitudinal modes of identical polarization are present. Despite this, the aggregate interaction of the multiple laser modes with their unique polarization rotation at the fiber output produces low coherence mixing of optical signal among fiber modes, shown in Fig. 3.14(c). Likewise, VCSEL emission is singlemode longitudinally, but typically multimode transversely with independent polarization and carrier phase. Therefore, the resulting interaction among fiber modes is highly incoherent, shown in Fig. 3.14(d). Of course, complete incoherence, as with the LED, is not expected, but the contrast ratio is quite low for VCSEL and FP emission in comparison to the output with a DFB laser.

As was shown in (3.22), the modal noise is dependent on the source coherence. Of course modal noise will not be eliminate as completely as with the use of LED, but it can be minimized. The measured speckle pattern indicate that the plurality of modes in VCSEL

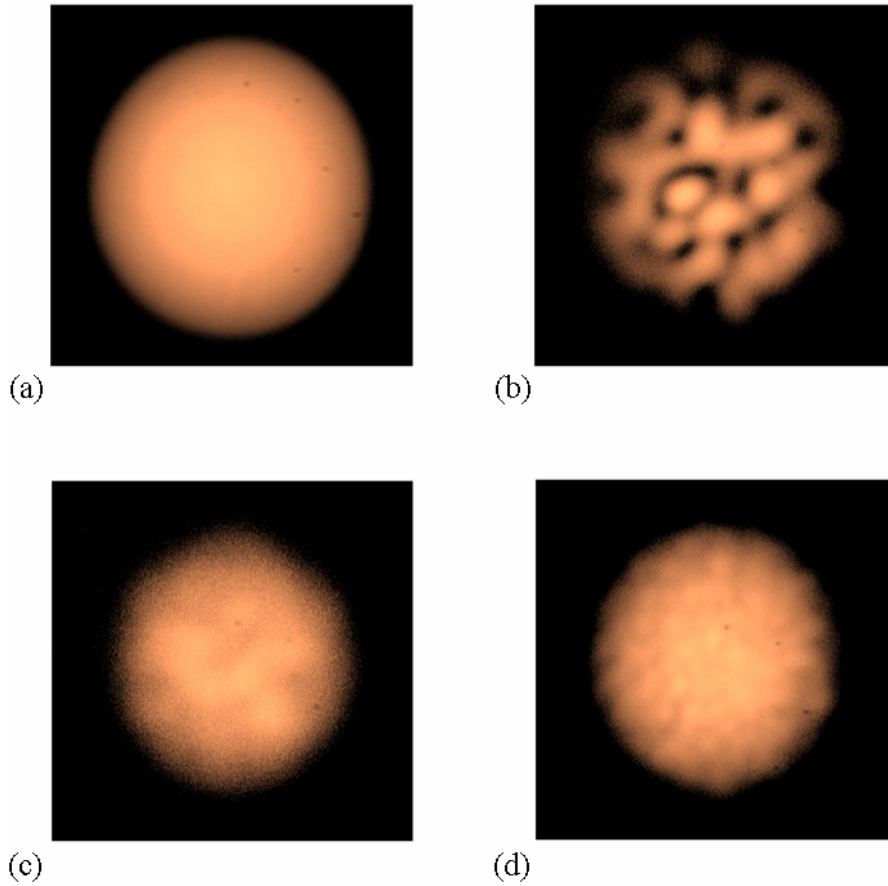


Figure 3.14: Speckle pattern of optical signal from 1.1-km fiber sample with various launch sources: (a) LED @ 850 nm, (b) DFB laser @ 1550 nm, (c) Fabry-Perot laser @ 1550 nm, (d) VCSEL @ 850 nm.

and FP laser can be used to manage these concerns. Other works, such as by Hahn *et al*, Cunningham *et al*, Dandliker, *et al*, and Kuchta, also support this conclusion by speckle contrast and bit error rate measurements [59], [60], [58], [61], [62]. These experiments shown significant reductions of coherent modal interaction and modal noise after a few hundred meters of fiber with the use of multimode laser sources. It should be kept in mind that even in a conventional MMF link, modal noise is of concern. Misalignment between fibers or fiber-PD will resulting in modal noise. For this reason, modal noise should be managed regardless of SRE. Fortunately, this is compatible with the synergy of MMF and VCSEL.

CHAPTER 4

EXPERIMENTAL RESULTS

“Always trust the simplest explanation that fits all the facts unless there’s a damn good reason not to do so.”

— Dr. Stuart Hay in *Incarnat* by Ramsey Campbell

In this chapter, measurements are made to demonstrate the viability spatially resolved equalization as well as the robustness of the two-segment PD employed. Link bandwidth with and without SRE is presented in the form of temporally measured impulse responses that show a robust 2× bandwidth gain. This includes measurements with variations in parameters such as wavelength, core size, fiber length and fiber alignment are investigated. Additionally, variation in launch conditions are tested to demonstrate the cooperative nature of SRE with restricted mode launch. The fiber link is modelled with the measured impulse response and eye diagram are computed. Finally, results of measured bit error rate experiments are presented.

4.1 Measurement of spatial diversity in MMF

To explore the spatial diversity upon which SRE is dependent, a straight forward test is conducted. A small pin-hole is used at the output of the fiber to mask all but a small portion of the optical irradiance, shown in Fig. 4.1. A short optical pulse is launched in the fiber, and the temporal response is measured and recorded. The optical beam is systematically scanned in the transverse directions as well as longitudinal direction.

The size of the pin-hole is chosen strictly based on availability. With a 15- μm pin-hole, resolution of the measured spatial diversity is maximized by allowing the optical signal to

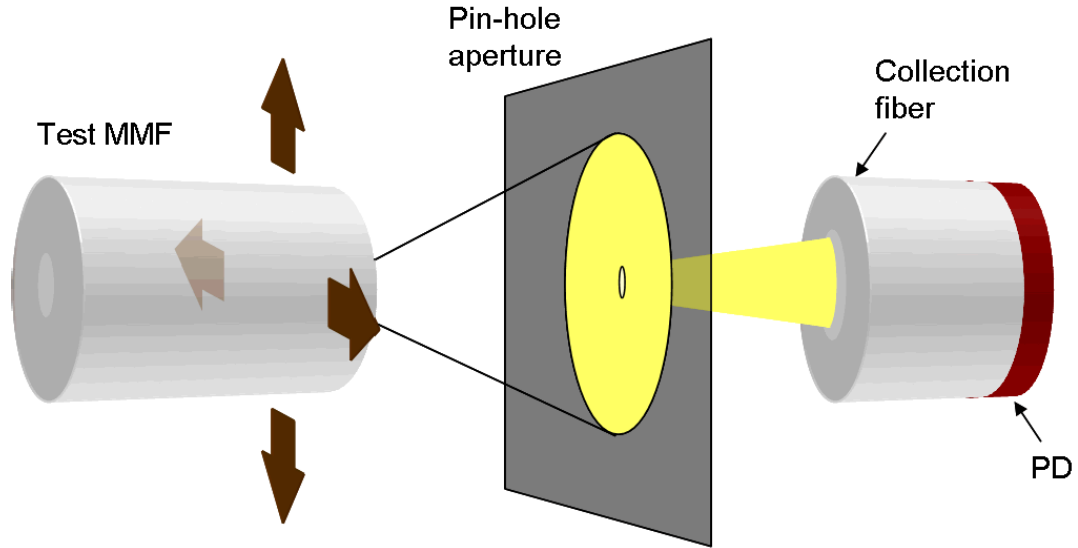


Figure 4.1: Measurement apparatus for spatial diversity measurement. Optical spot is spatially filtered with a $15\text{-}\mu\text{m}$ pin-hole placed in optical beam. Light transmitted through the pin-hole is received by high-speed photodetector through a $100\text{-}\mu\text{m}$ step-index MMF of high numerical aperture.

expand by diffraction: the pin-hole is placed in a range of $300\text{--}400\ \mu\text{m}$ from the output end of the fiber. The fiber end is flat-cleaved and no intervening optics other than the pin-hole is used. To maximize the signal-to-noise of the recorded photocurrent, a commercial 2-GHz photoreceiver, with an integrated pre-amplifier, is used to record the impulse response. The typical bandwidth of the 1.1-km samples of MMF tested is $200\text{--}800\ \text{MHz}$. For measuring this cutoff frequency, the 2-GHz receiver bandwidth is sufficient; however, some high frequency component, of less importance, of the impulse response is lost.

The fiber position is precisely controlled using a 3-axis, translation stage manipulated by a closed-loop motor controlled microactuator. The microactuator is driven by a motor controller via a LabView[©] program that synchronizes the position of the fiber and recording of the temporal response.

A mode-scrambler is used to ensure distributed mode coupling. The mode-scrambler is composed of a patch of large numerical aperture (NA), $50\text{-}\mu\text{m}$ step-index fused silica fiber is used. The fiber is tightly meandered with pitch of 10 mm and radius of curvature of

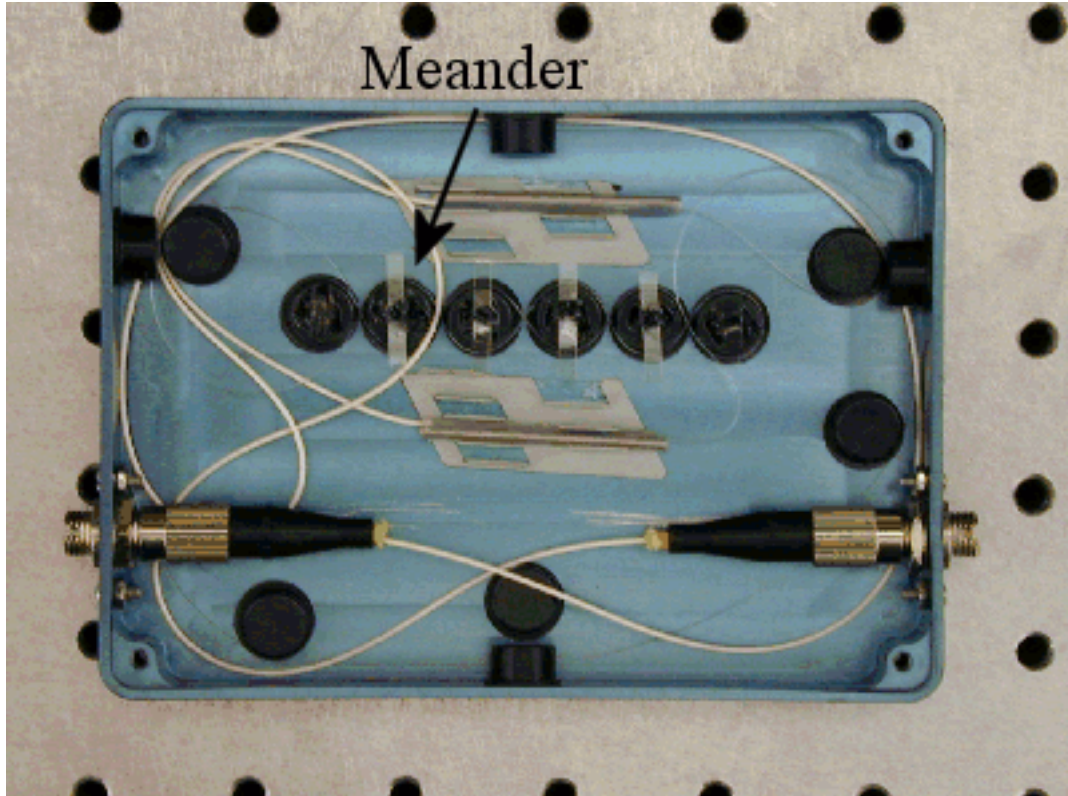


Figure 4.2: 50- μm , high-NA, step-index fiber mode-scrambler. SI-MMF is meandered around 5-mm radius posts spaced with 10-mm pitch.

5-mm, shown in Fig. 4.2. The use of a SI-MMF with a large NA ensures strong overlap between fiber and source mode profile. The meandering induces intermodal coupling in the SI-MMF by perturbation of the index profile [63]–[65]. A sufficient number of turns is used such that 1-dB of the optical power is coupled to the radiative modes. Assuming, strong nearest-neighbor coupling in the fiber, optical power is assumed through all the fiber modes from the fundamental mode couples to the radiative modes.

The measurements are made on samples of 1.1-km, 50- μm , graded-index multimode fiber excited with a 1-ps, 1550-nm optical pulse. The variation in impulse response as a function of position along the diameter of the optical spot is shown in Fig. 4.3 for a sample fiber. The presence of an optical signal, presumably the low-ordered modes with an early arrival time, is strongest at the center of the optical spot, while more slower modes, the

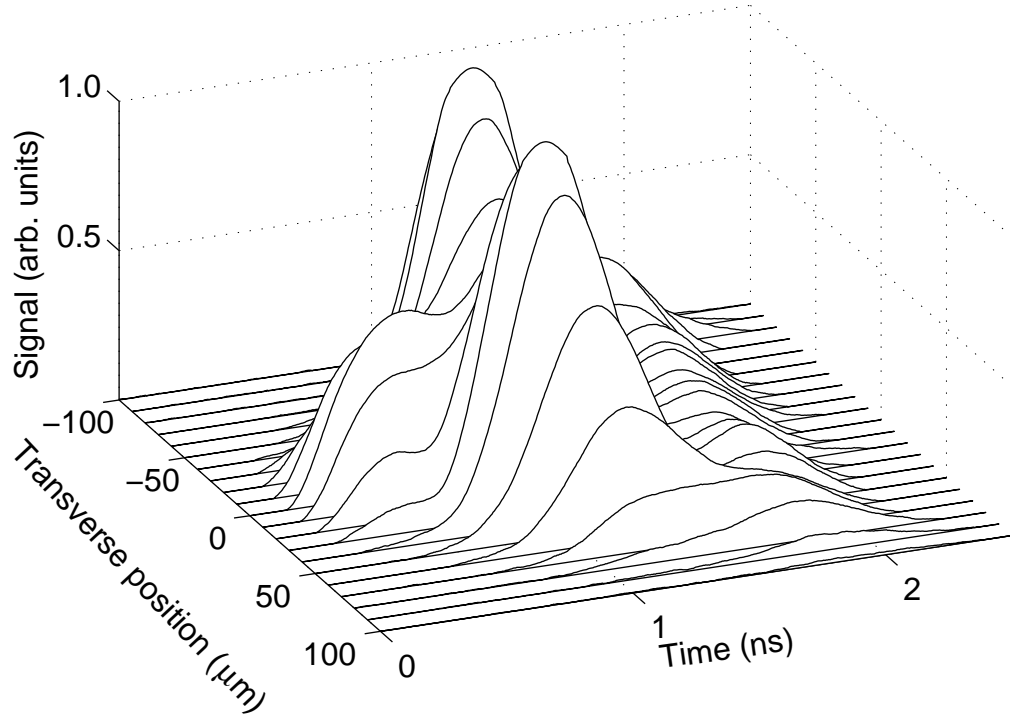


Figure 4.3: Diversity along optical spot diameter. Impulse response of 1.1-km, 50- μm core, graded-index multimode fiber, excited with a 1-ps, 1550-nm optical pulse launched through a mode scrambler.

high-ordered modes, are present throughout the entire optical spot.

4.2 Measurement of MMF link with equalization

Fiber bandwidth is determined by measurement of the temporal response to an optical impulse. This is possible, since MMF is dominated by intermodal dispersion and incoherent mixing of modes at photodetector [23], [58], [66]. But to maintain the dominance of DMD over chromatic dispersion, the spectrum of the optical impulse must be small. Pulse spreading due to chromatic dispersion can be estimated with the following expression,

$$\Delta\tau = \Delta\lambda D, \quad (4.1)$$

where $\Delta\lambda$ is the spectral width (in wavelength) of the optical pulse, and D is the dispersion parameter of the fiber. For intermodal dispersion of 500 ps/km, chromatic dispersion less

than 50 ps/km can be neglected. Since dispersion parameter in fused silica fiber at 850-nm is 100 ps/(nm-km), the spectral width of 850-nm probe pulse must be less than 0.5 nm. At 1550-nm, the dispersion parameter is 17 ps/(nm-km); the spectral width for a 1550-nm probe pulse must be less than 3 nm.

Shown in Fig. 4.4 is the basic testbench used for testing of the multisegment photodetector (MSD). To each end of the fiber under test (FUT), FC connectors are attached by fusion splicing on commercially available connectorized patchcords.

A similar 1-m patchcord is used to couple the optical signal to the MSD. The loose end of the pigtail is aligned with the MSD with a fiber positioner mounted on a 3-axis positioning stage, shown in Fig. 4.5.

4.2.1 Nominal MMF link bandwidth measurement

Using a fabricated MSD of 55- μm radius, the impulse response is a 1.1-km, 50- μm -core graded-index MMF is measured [67]–[69]. To match the approximate location at which the spatial diversity is measured, the 55- μm radius MSD is used. The fiber is excited with a 810-nm optical pulse generated with a Ti:sapphire laser. For testing at this wavelength, a 10-ps optical pulse with a spectral width <0.3 nm, generated by a Spectra-Physics actively mode-locked Ti:sapphire laser. The repetition rate for this laser is $\ll 40$ -MHz allowing for pulse broadening up to 25 ns. The source is coupled to the fiber under test (FUT) with the step-index fiber mode scrambler, shown in Fig. 4.2.

The impulse response is measured for two case, both with the same MSD, shown in Fig. 4.6(a). First, each segment is biased identically, producing a signal from the sum of the two photocurrents. This corresponds to the impulse response observed by a conventional PD. Second, the two segments are then biased with voltage of equal magnitude but opposite polarity so that the resulting signal is the difference of the two photocurrents.

The nominal fiber bandwidth is 280 MHz-km. Simulation of this type of fiber predicts 500-MHz-km bandwidth; however, for these particular test fibers, no assurance of minimum bandwidth is given by the manufacturer. Bandwidth measurement provided by manufacturer specifies 417 MHz-km. None the less, a $2\times$ bandwidth gain is achieved with the use

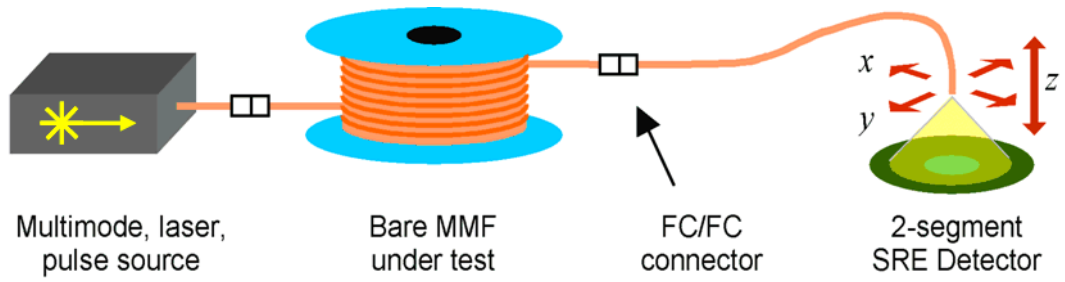


Figure 4.4: Experimental apparatus for measurement of MMF link performance by impulse response measurement.

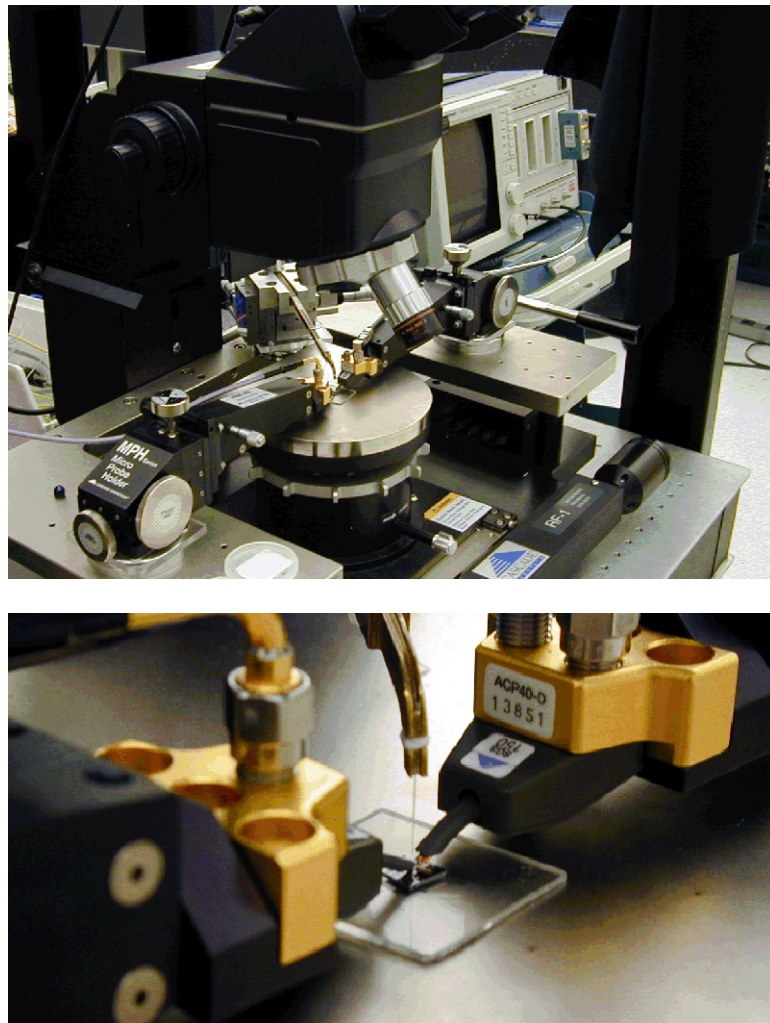


Figure 4.5: Probe station used for MSD-fiber alignment and on-wafer impulse response measurement.

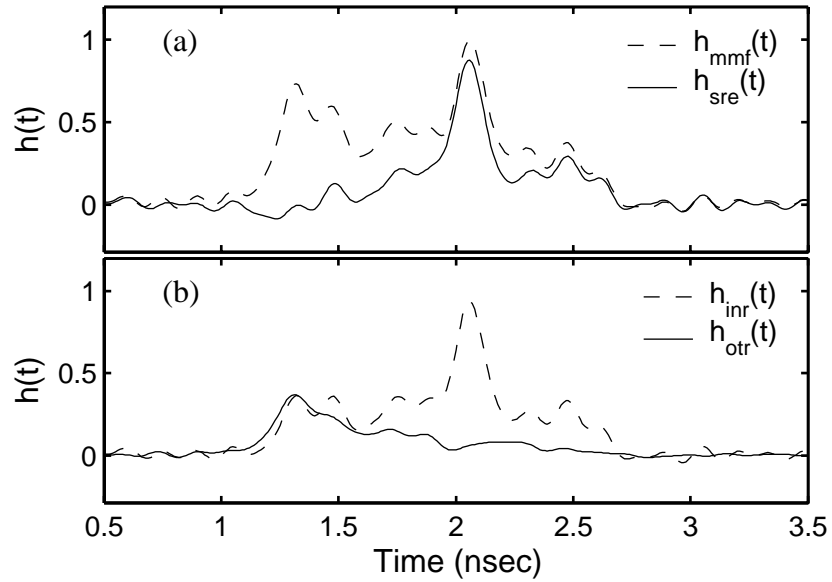


Figure 4.6: (a) Impulse response of 1.1-km, 50- μm MMF with 10-ps optical pulse excitation at 810-nm with and without equalization via a 55- μm MSD, 415 μm from the fiber output. (b) Measured impulse response observed by inner and outer PD, $h_{inr}(t)$ and $h_{otr}(t)$ respectively.

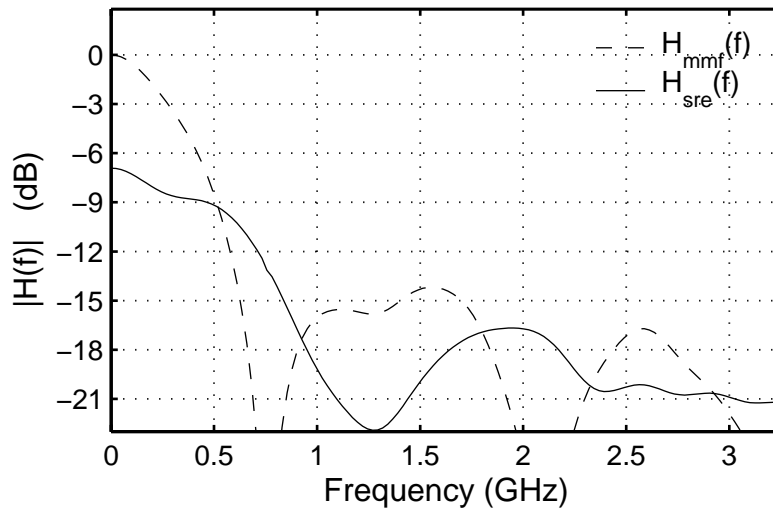


Figure 4.7: Frequency response computed from measured impulse response of fiber link with and without SRE.

of a two-segment photodetector when the fiber was set to a position of $415\ \mu\text{m}$ from the MSD. Recall that in the simulation, it was found that $400\ \mu\text{m}$ was the optimal distance. A 4% deviation in fiber-MSD gap between simulation and measurement could be considered within the "noise" of the system.

Finally, the MSD is biased with positive voltage one PD, with no bias on the other, so that photocurrent of the individual segment can be recorded, shown in Fig. 4.6(b). This is repeated such that the photocurrent of both inner and outer PD segments are recorded.

The frequency response reflects a optical loss of 3.4-dB induced by SRE. The higher than predicted loss can be attributed to the variation source coupling via the mode-scrambler as well as possibly coupling of optical power within the fiber modes, resulting a degradation in diversity of temporal response among the fiber modes.

4.2.2 Verification of SRE detectors scalability

The MSD size of $55\ \mu\text{m}$ is chosen for maximum flexibility in testing. However, other considerations, such as device capacitance, may require the use of a much smaller device. A device scalability test is performed. A near-field measurement is difficult, due to finite MSD size and on-wafer probe technique. MSD of decreasing sizes are used to equalize the fiber link. For each MSD size, the appropriate fiber-MSD gap is found to maintain comparable bandwidth gain.

Plotted in Fig. 4.8 is the measured impulse responses made at 810-nm with MSDs of four different radii—measured by size of inner PD—on a $50\text{-}\mu\text{m}$ core MMF. Adjusting the MSD-fiber distance appropriately, the measured impulse response matches each other within a tolerable difference; the frequency response matches as well. Also plotted, in Fig. 4.9, is the correlation between SNR penalty and bandwidth gain. The close overlap among the curves shows relatively little sensitivity to modal diffraction. It is unclear if there is any significance to the slight difference in the correlation curve for the $55\text{-}\mu\text{m}$ MSD, compared the MSD sizes.

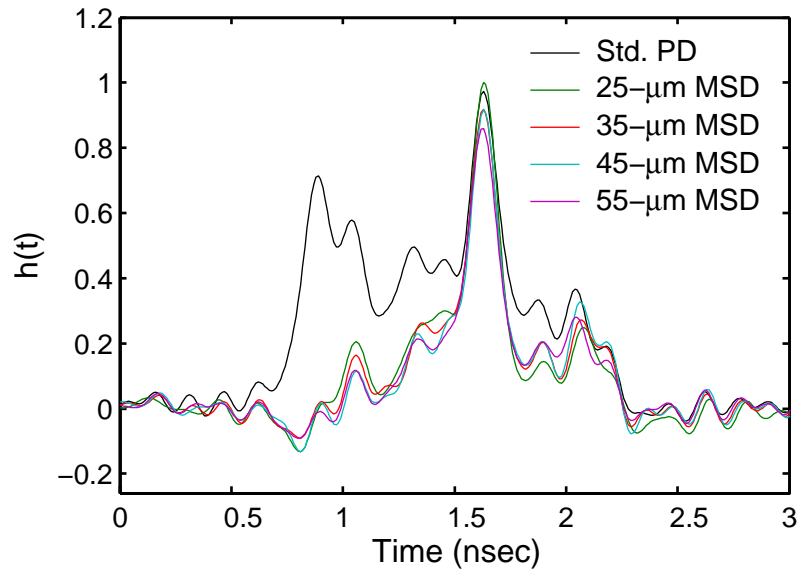


Figure 4.8: Impulse response of 1.1-km, 50- μm MMF link with MSD of various radii.

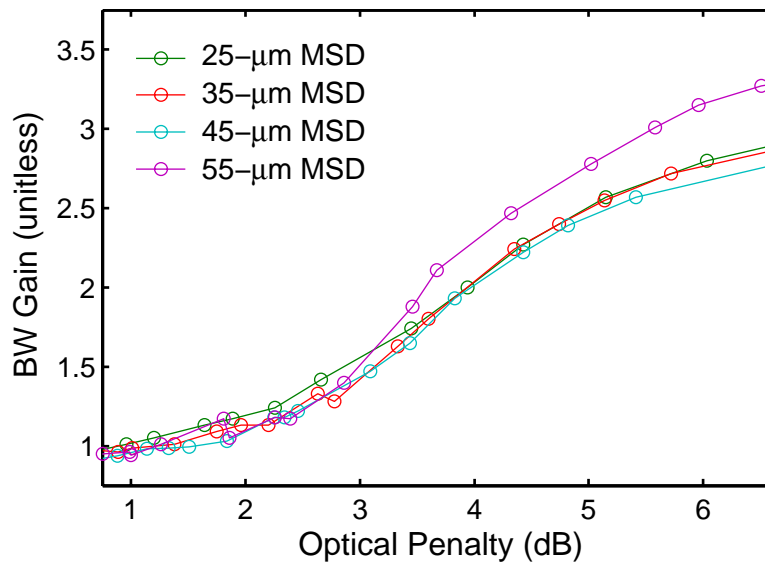


Figure 4.9: Correlation plot between optical penalty and bandwidth gain due to SRE for a sample of 1.1-km, 50- μm MMF with spatially resolved equalization via MSD of various sizes.

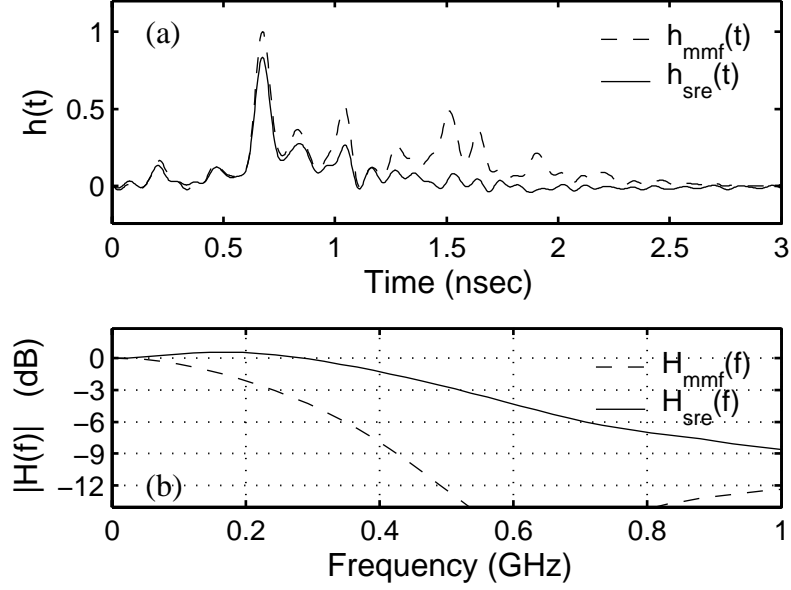


Figure 4.10: (a) Impulse response of 1.1-km, 50- μm MMF at 1550-nm. A 55- μm MSD is at 400- μm from fiber output. (b) Frequency response computed from measurement.

4.2.3 Enhanced MMF link at telecom wavelengths

Impulse response is measured on a 1.1-km, 50- μm fiber, with 1-ps 1550-nm optical pulse. For testing near 1550-nm, a 1-ps optical pulse generated with a passively mode-locked soliton fiber laser. The spectral width of 3-nm ensures that chromatic dispersion is less than $10\times$ less than intermodal dispersion. The optical source is coupled to the FUT with the step-index fiber mode scrambler. A 55- μm MSD is used for fiber equalization.

The measured impulse response and the computed frequency response, with and without SRE, is shown in Fig. 4.10. The observed fiber bandwidth is 250 MHz-km, which is close to the predicted bandwidth of 180 MHz-km. Interestingly, fiber bandwidth is similar to that at 810-nm. Importantly, however, a $2\times$ improvement in bandwidth is achieved with the MSD at 405- μm from fiber output. This matches well with the simulation and experimental measurement at 810-nm. Clearly, the divergence among the fiber modes does not vary significantly over wavelength.

This impulse response measurement is repeated on several fiber samples. A total of

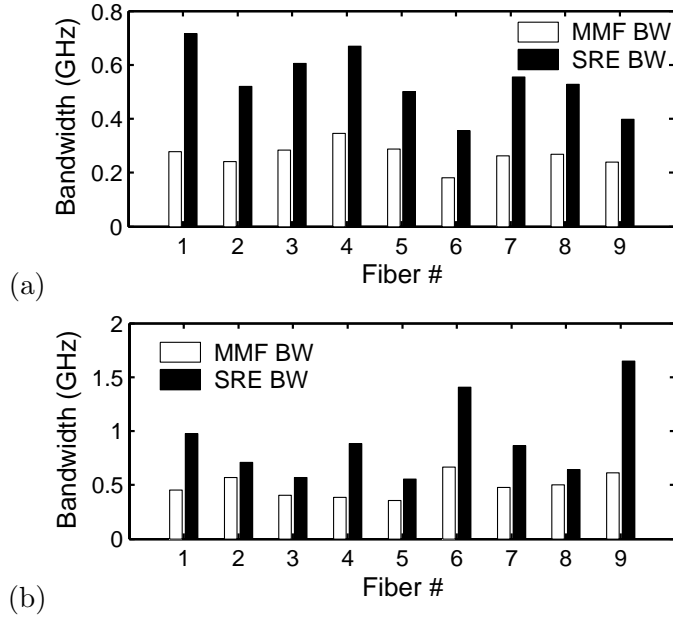


Figure 4.11: (a) Bandwidth gain versus optical loss via SRE enhancement for a 9 samples of 1.1-km, 50- μm core MMF tested at 1550-nm with 55- μm MSD at 400 μm from fiber. (b) Measured BW gain of 9 samples of 62.5- μm core MMF with 55- μm MSD 310 μm from fiber output.

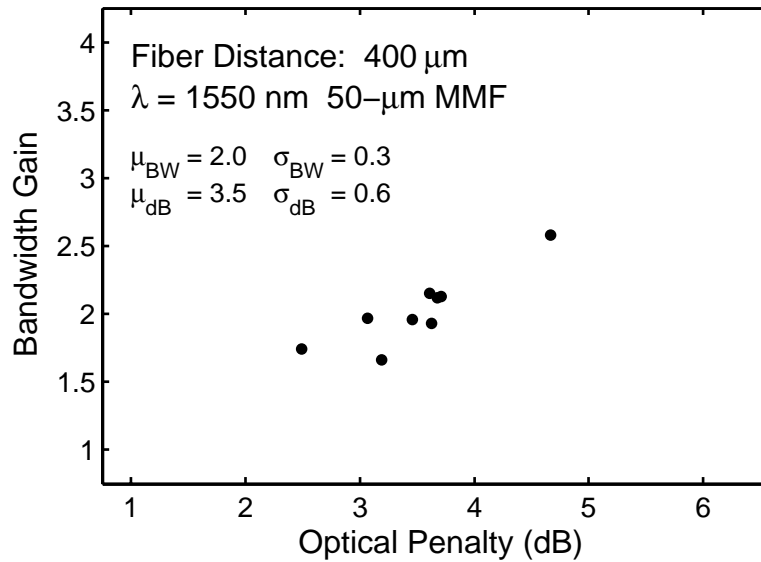


Figure 4.12: (a) Bandwidth gain versus optical loss via SRE enhancement for a 9 samples of 1.1-km, 50- μm core MMF tested at 1550-nm. Identical MSD configuration with no fiber specific optimization.

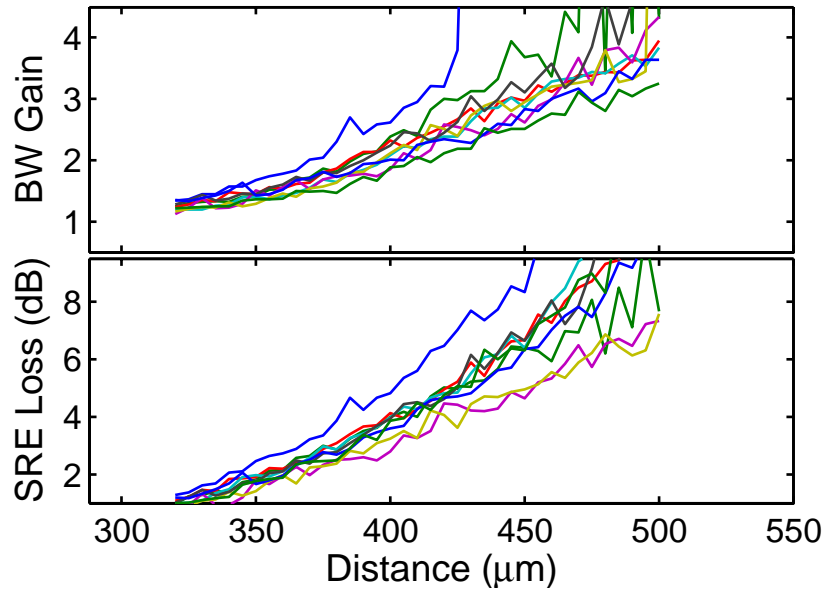


Figure 4.13: Measured link bandwidth gain and loss for 9 samples of 1.1-km, 50- μm MMF at 1550 nm. Measurements made with MSD at various distances from flat-cleaved fiber facet.

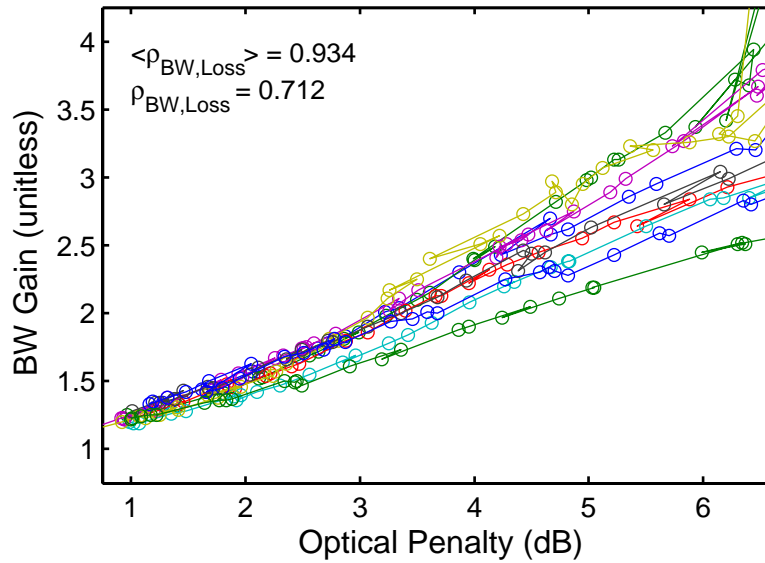


Figure 4.14: Correlation plot between optical penalty and bandwidth gain for 9 samples of 1.1-km, 50- μm MMF, measured at 1550-nm. $\langle \rho_{\text{BW, loss}} \rangle$ is the average of the correlation coefficient of individual curves; $\rho_{\text{BW, loss}}$ is the correlation coefficient of the average curve.

9 samples of 1.1-km graded-index MMF with 50- μm core are tested. Measurements are made at various distances from the fiber output. Shown in Fig. 4.11(a) is the measured fiber bandwidth, with and without SRE, with the MSD at 400 μm from the fiber output. Additionally, similar measurements are made with 9 samples of 62.5- μm fiber. Other than the necessary adjustment for the core size, no fiber specific optimization is performed. Shown in Fig. 4.11(a) is the measured fiber bandwidth, with and without SRE; however, the MSD is at 310 μm from the fiber output. Numerical models predicts that a 300- μm gap is required.

In each case, a nominal 2 \times bandwidth gain is achieved with 10% variation. These variations are examined in more detailed for the 50- μm fiber by comparing with the resulting optical loss, shown in Fig. 4.12. Clearly a correlation between BWG and optical loss is present, similar to that observed in simulation. This correlation is extended to the full sweep of the MSD-fiber distance for all 9 samples, shown in Fig. 4.13. The resulting correlation between BWG and loss is plotted in Fig. 4.14.

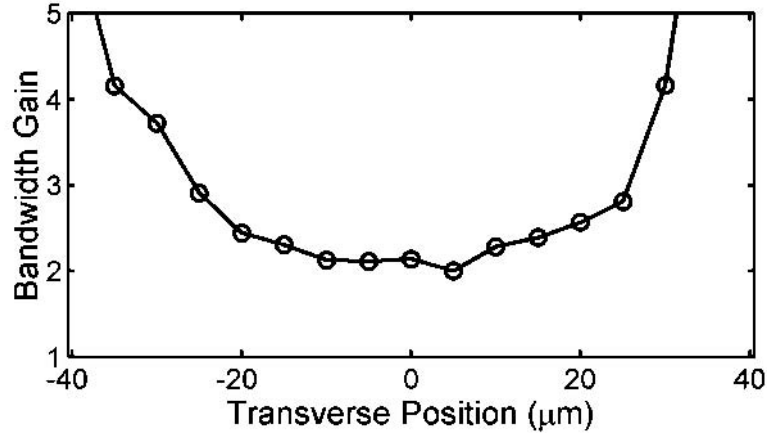


Figure 4.15: Bandwidth gain versus transverse misalignment

4.2.4 Experimental verification of alignment tolerance

As was done in simulation, the impact on enhancement by SRE as a function of device misalignment is studied. The purpose of this is to ensure alignment tolerance comparable to that of MMF. Impulse response is measured and change in bandwidth is determined for a range of MSD-fiber offset, shown in Fig. 4.15. As with the other measurements, the distance between fiber and MSD is maintained at $400\text{-}\mu\text{m}$. A alignment tolerance of $\pm 20\ \mu\text{m}$ is observed, nearly identical to that predicted in simulation. Of course, just as is in the simulation, the increasing of the bandwidth gain outside the optimal range comes with an increasing penalty to optical power.

The asymmetry in the data, shown in Fig. 4.15, may be attributed to tilt in the fiber axis relative the MSD surface normal. This tilt is deliberately used, solely for the purpose of visual alignment of the fiber to MSD via a overhead microscope, and is not required for proper use of spatially resolved equalization.

4.2.5 Measured equalization with restricted launch condition

As is discussed in the numerical model, the source coupling condition is has a significant impact on the link bandwidth. The "fiber bandwidth" is measured with many of the

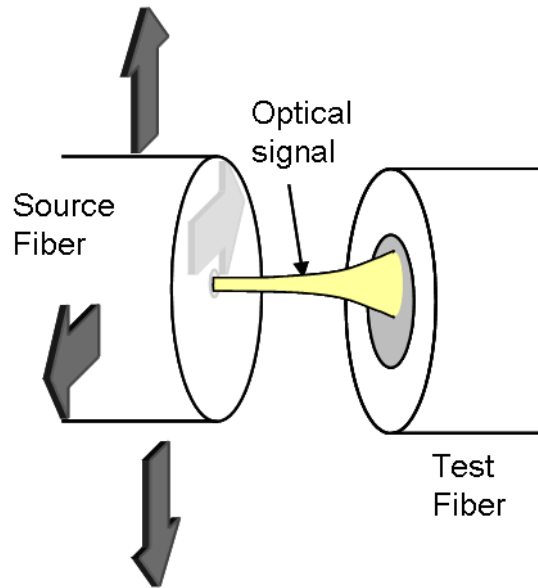


Figure 4.16: Method of controlling launch condition.

mode partially coupled with optical power, excited with a representative multimode VCSEL source. The use of a restrict mode launch (RML), where only a few modes are excited, can result in lower ISI in the link than is indicated by the fiber bandwidth.

A singlemode fiber, at 850-nm, is used to launch optical pulse into the fiber under test. The optical spot size at the output facet of the launch fiber is $4.5\text{-}\mu\text{m}$ -diameter; however, by allowing the beam to diverge, the spot size can be manipulated, shown in Fig. 4.16. Assuming a Gaussian beam profile of the optical signal out of the launch fiber, mode-field size is computed with the standard Gaussian beam propagation estimates and the applied fiber-fiber gap.

For each launch condition, the impulse response is measured with and without SRE enhancement. The bandwidth gain, on a launch-by-launch basis is plotted in Fig. 4.17; this BWG by SRE specific to the each launch condition. Shown in Fig. 4.18 is the combined bandwidth gain of SRE and RML compared to the overfilled launch with conventional detection.

Over the full range of launch conditions, significant enhancement in the link bandwidth

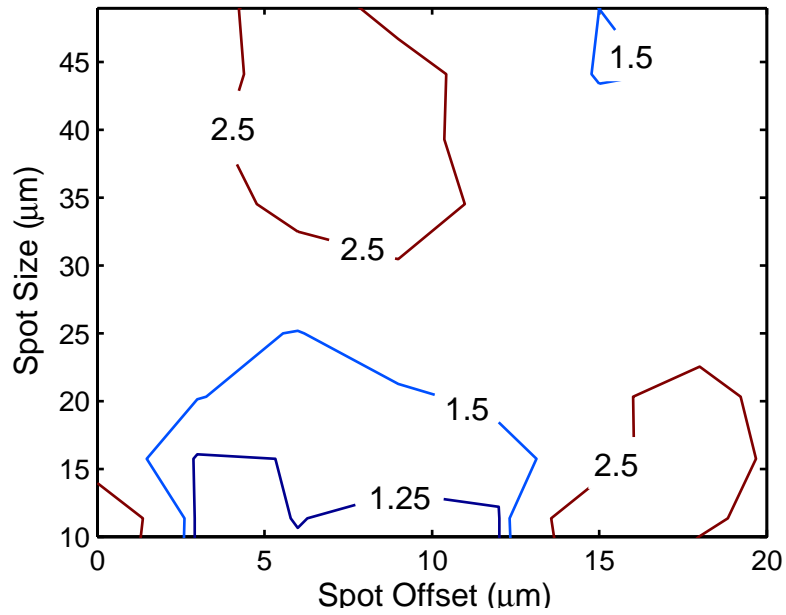


Figure 4.17: Enhancement of fiber bandwidth compared to standard detection for given launch condition.

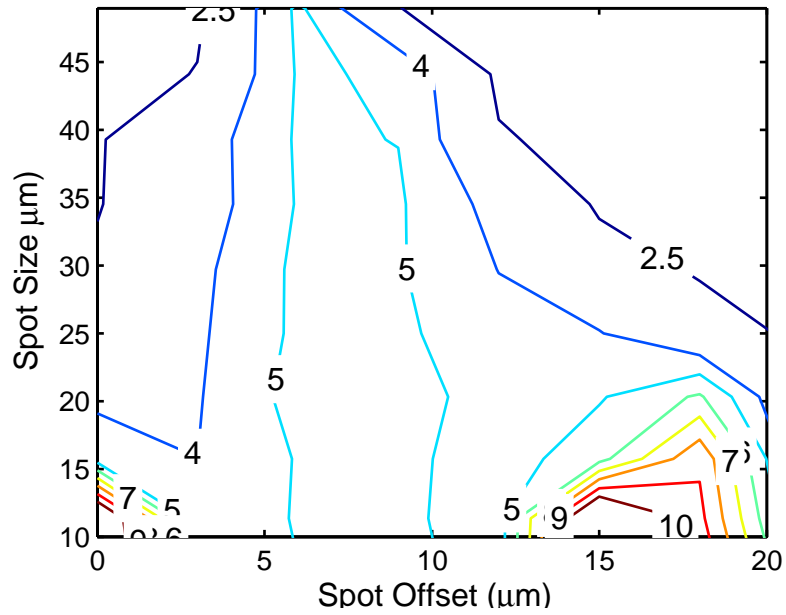


Figure 4.18: Enhancement of fiber bandwidth compared to standard detection with overflow launch condition (worst-case bandwidth).

is achieved just by spatially resolved equalization; the average BWG is $1.5 - 2.5\times$. This is similar to that predicted by simulation. Moreover, when including the bandwidth gain inherent to the launch condition, the overall fiber link bandwidth is nominally $4-5\times$ greater than the overfilled launch condition.

4.3 Bandwidth improvement by SRE variations

Finally, variants on the embodied SRE are considered. In actuality, the parameter space for variants on SRE may be included numbers of segments as well as scaling factor and group delay applied to each PD photocurrent. But two simple variants are studied. For a $55\text{-}\mu\text{m}$ MSD, tested at 1550-nm with a sample of 1.1-km, $50\text{-}\mu\text{m}$ core MMF, the impulse response is measured for a various fiber-MSD gaps. The measured impulse response of the inner and outer PD segment are used to simulate SRE by other means of photocurrent combination. The resulting impulse responses are compared to the bandwidth of the standard link with overfilled launch.

4.3.1 Single-segment mode filtering

While a two-segment MSD, where the photocurrents are subtracted from each other is achieved with relative simplicity, a single PD segment that partially detects irradiance can achieve further simplicity. To understand the benefits gained for the marginally added complexity by subtraction of the photocurrents, the bandwidth enhanced by SRE is compared to the case where only the inner PD photocurrent is used in signal detection. The distribution of the optical signal is managed by exploiting the divergence of the optical beam. The resulting bandwidth gain for varying fiber-MSD distance is shown in Fig. 4.19(a). A limited increase in bandwidth of only $1.2\times$ is achieved with use of just the inner PD signal, matching the simulation results. Clearly, full suppression of the HOM is not achieved without the use of the residual signal in the outer PD.

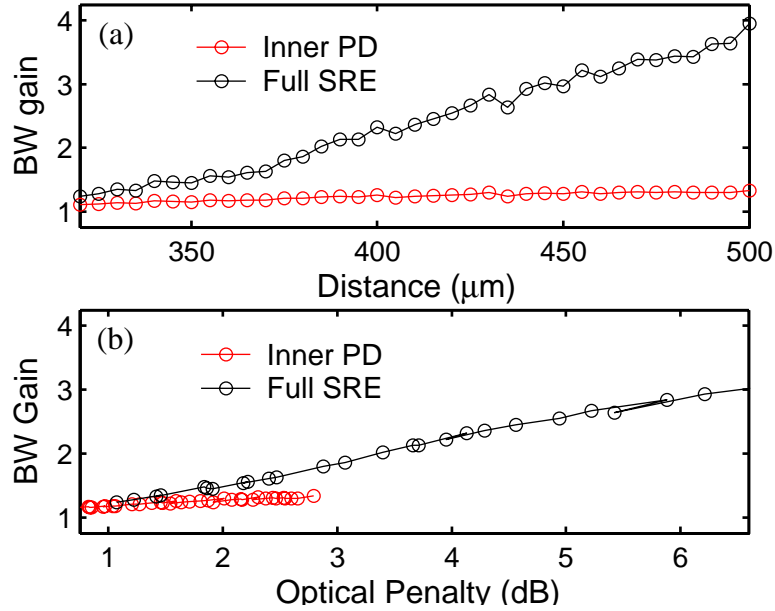


Figure 4.19: Comparison of bandwidth gain with high-ordered mode suppression with subtraction of the outer PD photocurrent (Full SRE) versus partial detection of optical power with a small PD segment (Inner PD). (a) Bandwidth gain versus fiber-PD gap.(b) Correlation between optical SNR penalty and bandwidth gain.

4.3.2 Mode retiming

It might be reasoned that with sufficient separation of high and low ordered modes between the two PD segments, recombining the signal with an appropriate delay can result in improved fiber impulse response. In which case, the summation of the two photocurrents, with appropriate relative group delay, would result in comparable bandwidth improvement but without the optical penalty. In effect, the relative mode-delay of the HOM are adjusted.

The results shown in Fig. 4.20 indicate that mode separation is far from ideal with the two-segment PD; while no penalty is incurred by suppression of the HOM energy, a maximum of $1.1\times$ bandwidth improvement is achieved by combining the segment photocurrent with a group delay adjustment. This should be expected, since mode separation is achieved by diversity in irradiance profile not field profile. A mere 10% gain in bandwidth cannot justify the added complexity of tuning the group delay adjustment based variation in intermodal dispersion.

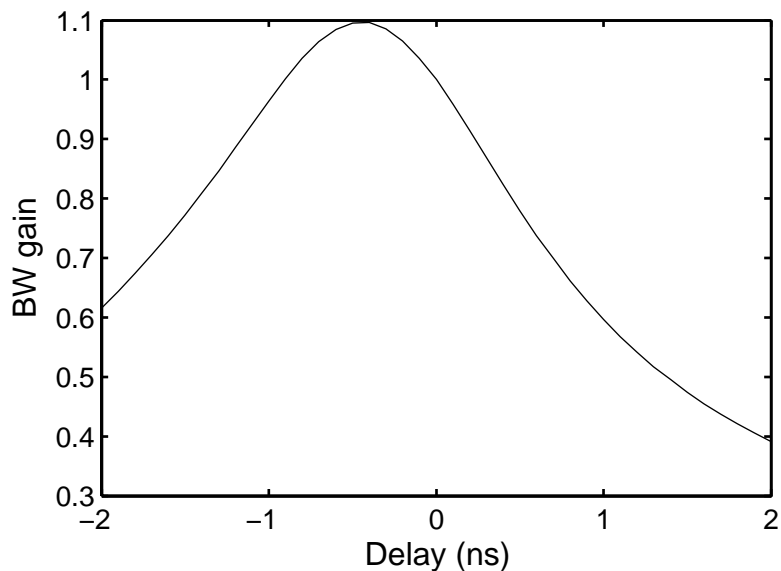


Figure 4.20: Computed bandwidth gain by addition of the two-segment photocurrents with adjustment of group delay for outer PD signal.

4.4 Full SRE receiver test with transmitted data

4.4.1 Hybrid SRE receiver

In addition to characterization of SRE by impulse response measurement, MMF-SRE link performance is evaluated by simulated and measured bit error rates and eye diagrams. A receiver is built with a fabricated MSD and an commercial 10-GHz transimpedance amplifier (TIA), Fig. 4.21. The MSD and TIA are linked by 0.6-mm length of 0.7- μm -diameter gold wire, and RF 50- Ω wafer probes are used to collect the amplified signal from the TIA. Just as with impulse response measurements, bit error rate and eye diagram measurements for both standard and SRE detection are made with the same receiver by appropriate selection of bias polarity.

4.4.2 Eye diagram measurements

In a 1.1-km long, 55- μm core, MMF, a fiber link is tested with spatially resolved equalization. The inherent bandwidth of the fiber supports roughly 600-Mb/s data transmission with little

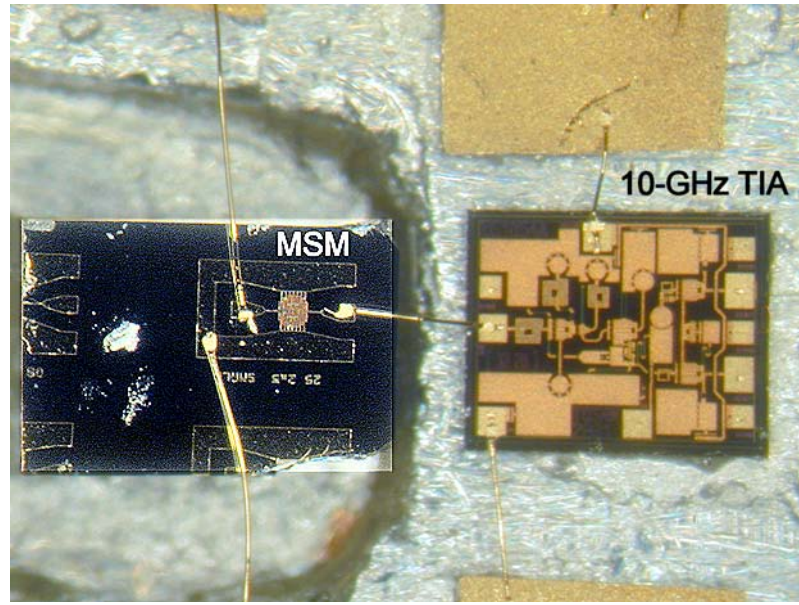


Figure 4.21: Fabricated hybrid SRE receiver with transimpedance pre-amplifier

intersymbol interference. To test the bandwidth enhancement capabilities of SRE, a non-return-to-zero optical pulse at a rate of 1.25 Gb/s is transmitted. An externally modulated, 1550-nm Fabry-Perot laser is chosen as the transmitter. To emulate a VCSEL illumination, the FP source is coupled to the MMF link via the step-index fiber mode-scrambler. A second link test is performed with the same fiber and MSD, but with a directly modulated 850-nm VCSEL source compliant with IEEE802.3ae standards. The measured eye diagram of the link with and without SRE at the is shown in Fig. 4.22 and Fig. 4.23.

A significant amount of eye closure in both the vertical and horizontal directions is observed for the 1550-nm link test. The ISI appears to be prohibitively high such that no increase in transmitted power can be used to attain error-free transmission. Such signal quality can make clock recovery difficult in real data links. With SRE, on the other hand, the ISI due to the fiber is reduced. A marked-improvement in the quality of the eye, both in the vertical opening and the reduction of jitter, shown in Fig. 4.22b, is observed allowing for both clock recovery as well as error-free data transmission. Likewise, eye quality is significantly improved in the link test at 850 nm.

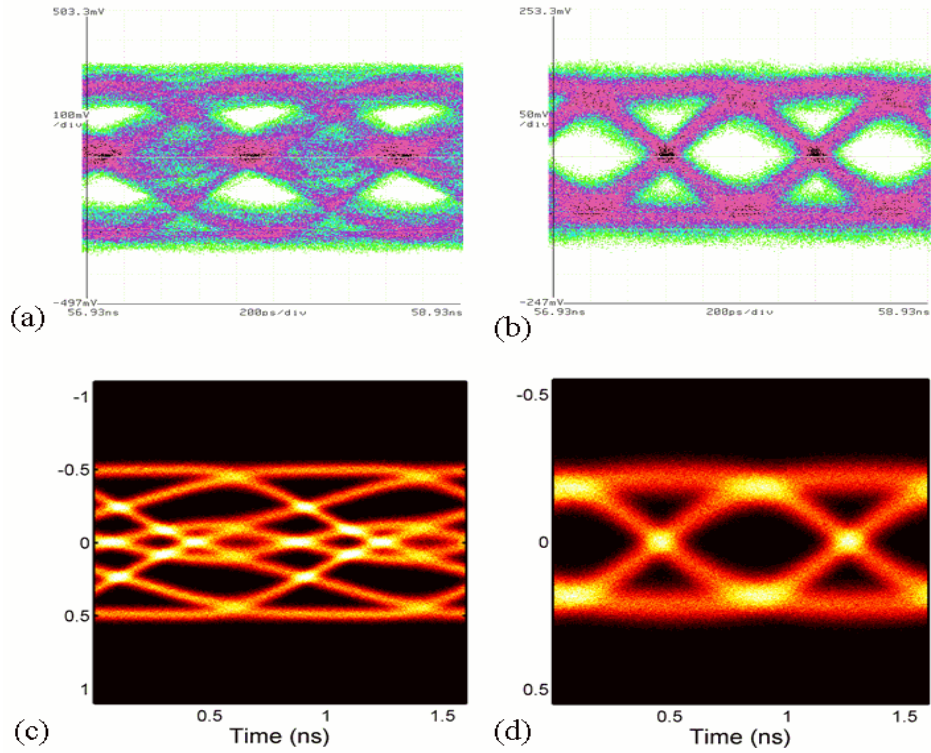


Figure 4.22: Eye diagram for 50- μm core, 1.1-km MMF link. FP laser, externally modulated FP laser at 1.25 Gb/s is coupled into fiber via step-index mode-scrambler(a) and (b) Measured eye diagram without and with SRE respectively. (c) and (d) Simulated eye diagram without and with SRE respectively, using measured impulse response of fiber

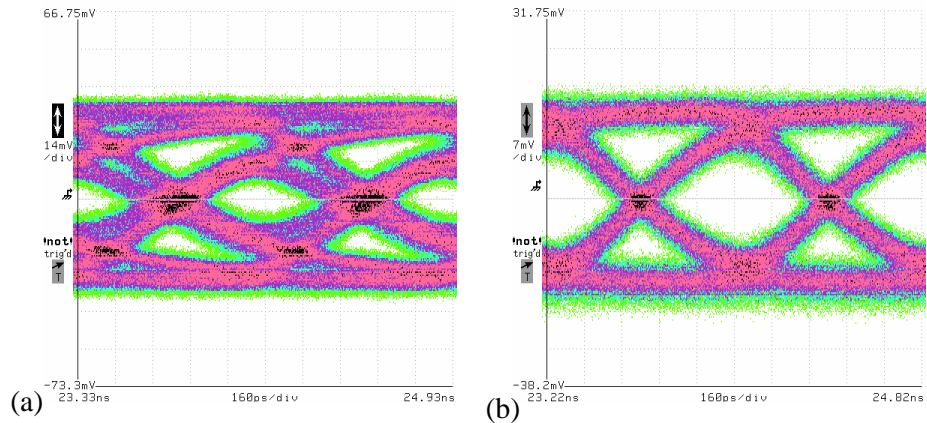


Figure 4.23: Eye diagram for 50- μm core, 1.1-km MMF link. Directly modulated VCSEL laser at 1.25 Gb/s coupled directly into MMF. Measured eye diagram (a) without and (b) with SRE.

For comparison, the experimental link is numerically modelled as well. Using the measured impulse response of the FUT, with and without SRE enhancement, the output signal to a transmitted non-return-to-zero pulse sequence is computed. The transmitted pulse in the simulated link are raised-cosine pulses of 800-ps width (*i.e.* inverse of data rate) and a rise-time that is 80% of the pulse width. For display, an arbitrary amount of noise is added to the output signal. In Fig. 4.22(c) and Fig. 4.22(d) are the computed eye diagram from the simulated optical link. Comparing only the quality in the eye-opening, both vertical and horizontal, a good match in signal quality is achieved between simulation and experiment. The comparable in both the standard and equalized link validates the use of measured impulse response in quantifying the fiber link response.

4.4.3 Bit error rate measurements

A bit error rate measurement is made with the hybrid-SRE receiver. An Anritsu MP1632A pattern generator and error detector is used to perform BER test on the equalized MMF link. The same optical link used with eye-diagram measurements is used, however, a 1-GHz noise filter and an additional limiting amplifier after the hybrid-SRE receiver is used to achieve the requisite signal levels for the error detector, shown in Fig. 4.24. In addition to BER on the real optical link, BER is estimated on a simulated optical link. The purpose of this simulation is to increase the confidence level of the conclusions drawn from measured impulse response.

A $2^{15} - 1$ pseudorandom bit sequence (PRBS), which is a sequence of varied 15-bit words, is transmitted optically in the test fiber at various power levels. The received electrical signal is monitored by the MP1632A error detector. The bit sequence is monitored, at a fixed power level, over a period of 20 mins, and the error rate is recorded. The resulting BER at different power levels are recorded and plotted in Fig. 4.25. Four tests are performed under two link conditions: a back-to-back link without any fiber, and one with the 1.1-km of 50- μm MMF. For each of these conditions, two tests are performed: one with and one without equalization by SRE.

Clearly, with MMF and conventional detection, the ISI is prohibitively high, preventing

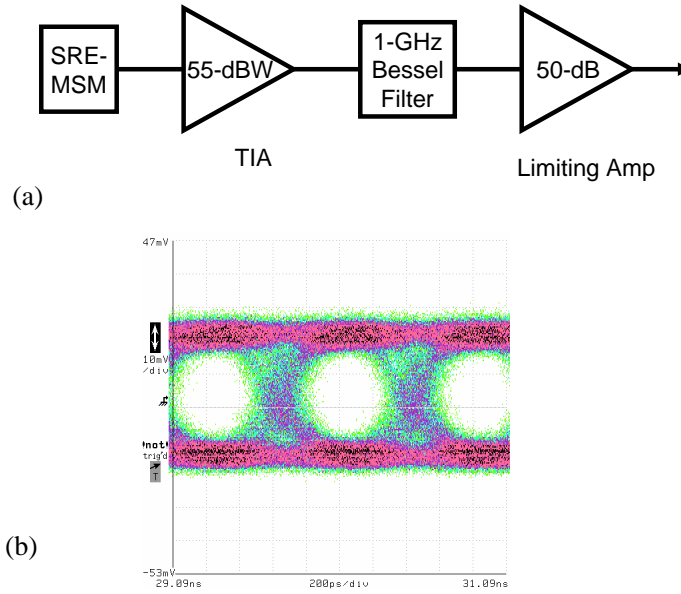


Figure 4.24: (a) Block diagram of SRE receiver with 1-GHz noise filter and limiting amplifier. (b) Output eye diagram of back-to-back (no fiber) link.

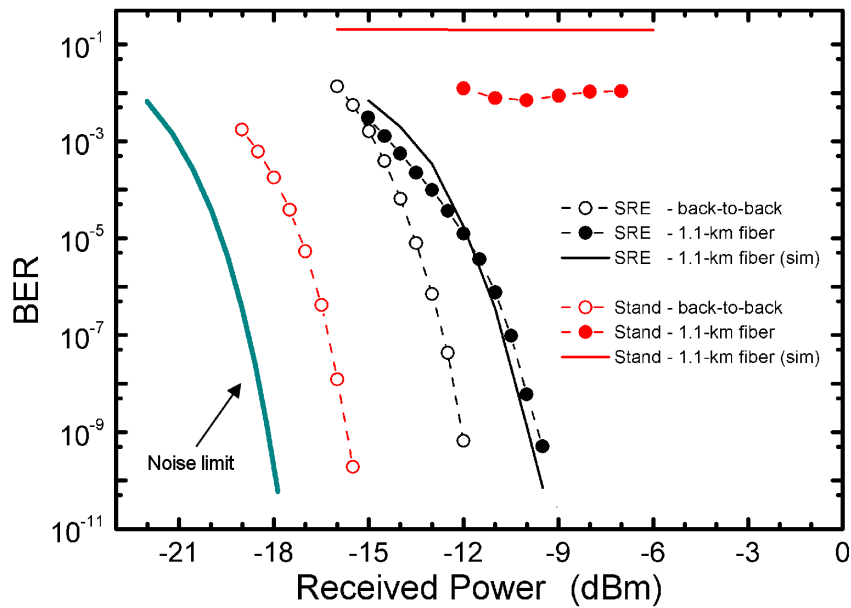


Figure 4.25: Measured bit error rate of four link configurations: two tests with the 1.1-km MMF and two without (back-to-back). For each link condition, two states of equalization: with and without equalization by SRE. Simulated BER experiments on the equalized channel are also plotted. Noise limit curve is the minimum achievable BER over ideal channel.

reasonable error rates. Error rates as high as 1 bit in every 100 is observed, without improvement with increasing power. This indicates a cross-over in the sampled signal; the intersymbol interference is excessively high such that the sampled voltage exceeds the threshold voltage.

With spatially resolved equalization of the fiber link, the ISI energy is substantially reduced. With increasing power, the bit error rate improves. Here the link is limited by noise rather than intersymbol interference. Transmission error rates of less than 1 in 10^9 is observed, with no indications of an error rate floor.

As was done for the numerical estimation of the eye diagram, the measured impulse response of the fiber is used as the numerical model of the communications channel. The transmitted signal is a random sequence of non-return-to-zero, raised-cosine pulses with a rise-time of the 80% of the pulse width. The noise power at the output of the real SRE receiver is measured without regards to source or spectrum, and an additive Gaussian white noise source of equal power is used in the simulation. Noise limited BER is computed based on this measured noise power. A BER experiment is performed on the numerical model of the measured link; the results are shown in solid curves plotted in Fig. 4.25. The numerical model predicts worse BER for the non-equalized link. This should not be unexpected since different sources are used for impulse response and BER measurements. Nevertheless, encouraging results are observed in the equalized link between simulation and measurement.

With the measured BER, we show that 10^{-9} bit error rate is achievable with -9 dBm of received optical power. On the other hand, commercially available receivers typically exhibit -21 dBm sensitivity. The discrepancy of 12 dB can be accounted for by several factors.

The system link, as implemented, exhibits more noise equivalent power (NEP) than is experienced by a optimal receiver designed for this data rate. Noise equivalent power is the equivalent optical power impinging on the receiver that would produce observed electrical noise measured at the receiver output. NEP of pre-amplifiers optimized for 1.25 Gb/s are inherent 1-2 dB better than that for the 10 Gb/s the amplifier used in the SRE receiver. Additional 2-3 dB improvement in the NEP can be attained in better receiver packaging;

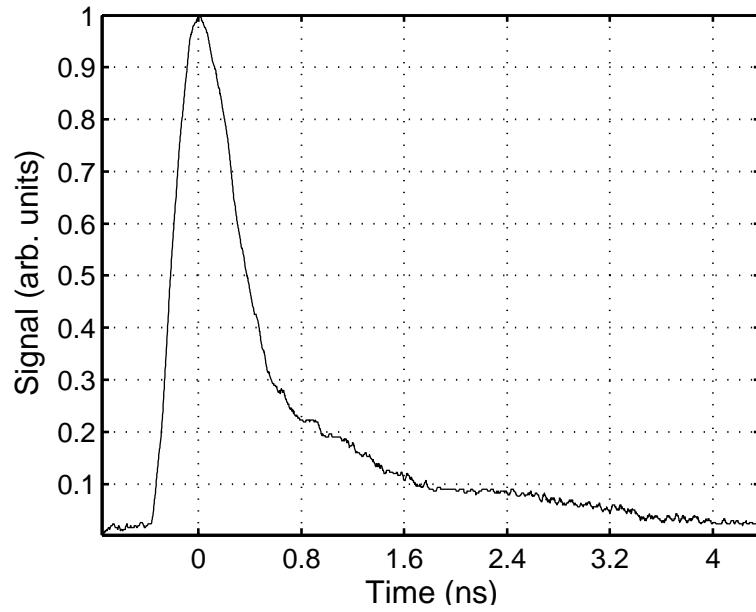


Figure 4.26: Impulse response of SRE receiver with 1-GHz noise filter.

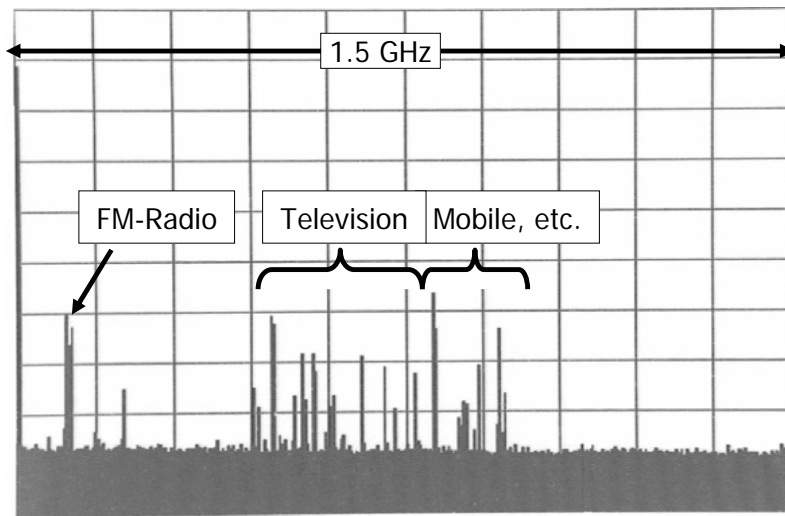


Figure 4.27: Spurious RF signal measured at the output of SRE receiver.

the open packing of the hybrid receiver permits injection of spurious signals from other sources such as TV and radio broadcast signal, mobile phone and point-to-point radios, shown in Fig. 4.27. For reduction of this "noise," device packaging or testing in an RF cleanroom must be considered. The net increase in NEP, from all the individual sources, is ~ 4 dB.

In addition to more noise, several factors, beside the 3 dB due to SRE itself, degrade the signal power. The lack of an anti-reflection coating on the detection surface results in 1.6-dB loss. Additionally, finger shadowing of the MSM electrodes results in 2-dB penalty that can be reduced with transparent electrodes or inverted-MSM structures [56], [70]. Finally 1.5-dB penalty is experienced by the ISI due to the long tail that appears in the impulse response of the MSM, shown in Fig. 4.26. These penalties to signal power is evident in the difference in BER between the noise limited and standard back-to-back link. The total degradation of the signal power is ~ 5 dB.

Accounting for the 5.5-dB loss in optical signal, and 4-dB excess NEP, the receiver can easily achieve a sensitivity of -18 dBm sensitivity, even with the 3-dB SRE penalty. This level of performance is compliant with receiver standards such as Gigabit Ethernet. However, these limits have hindered attempts of testing at higher data rates, including 2.5 and 10 Gb/s. The long tail of the receiver impulse response will significantly degrade the signal at the higher data rates. But also, fundamental relationship between bandwidth and thermal noise will degraded NEP by 1.5 and 5 dB for 2.5 and 10 Gb/s testing, respectively. Therefore, testing at higher rate can be made possible once the non-idealities of the fabricated receiver.

CHAPTER 5

OTHER SRE RELATED WORK

The use of spatially resolved equalization is only one of many forms of possible dispersion compensation. Merits of using decision feedback equalization (DFE) have been discussed in a previous section. Other channel impairment compensation techniques such as forward error correction (FEC), which employs parity check bits to allow erroneously detected bits to be automatically correct at the receiver end, are gaining favor in industry as well. And Viterbi decoders, which "unwraps" the distortion of a system, are also used in communication systems [71]. The versatility of these forms of electronic dispersion compensation (EDC) is difficult to deny. However, current bandwidth demands exceed the capability of practical implementation of electronic dispersion compensation in silicon CMOS technology. Yet, it is by virtue of the economy-of-scale, specifically of silicon CMOS technology, that is powerful motivation for the use of EDC. To close the gap between the data rates in optical systems with the limitation of silicon, the synergies of FEC, DFE and Viterbi decoder with the use of spatially resolved equalization is studied [72]–[75].

5.1 DFE with spatially resolved equalization

There is a great momentum towards the use of DFE in optical communication systems. Already, IC manufacturers have produced, in limited supplies, 10 Gb/s EDC components using DFE. Because of the limited silicon CMOS technology, these are simplified DFE structures primarily for SMF dispersion compensation, potential application to MMF link. Whereas chromatic dispersion in SMF results in a well-behaved distortion to the link impulse response, the random coupling of optical power from laser to fiber modes produce significant

”structure” in the frequency domain. In principle, an unlimited DFE structure can readily handle such variations; however, in practical implementation with limited DFE complexity, MMF may prove to be too difficult.

On the other hand, the use of SRE serves to allow for simplified DFE in multimode fiber link [72]. A numerical model of the fiber link, using measured fiber impulse response, is enhanced with an ideal DFE equalizer. For a given fiber response, a wide range in the number of forward (NF) and backward (NB) taps are considered. The weighting factors of the taps in each configuration are determined by the minimum mean-squared error estimator [18]. With the equalized channel, the output signal is computed for a random data sequence, and the necessary amplitude required for 10^{-12} BER is determined. The performance of the link is measured by the penalty to the receiver sensitivity P_{sense} , for the desired BER, in comparison to the back-to-back link, *i.e.* without fiber.

A number of measured fiber impulse responses are tested with DFE. The measurements are part of the IEEE 802.3z (Gigabit Ethernet) survey of fiber in installed MMF networks. [76]. A number of installed MMF were measured under various launch conditions.

A subset of data, corresponding to fiber illuminated with an overfilled launch at 850 nm, is tested in the DFE simulation. The fibers in the set are of different lengths, so the temporal response is normalized to 300 meters, assuming an inverse scaling of the time axis with fiber length.

Shown in Fig. 5.3 are computed P_{sens} as a function of NF and NB. The variability in the impulse response shape and bandwidth among the fibers results in highly disparate contour plots. Indeed, the minimum required NF, NB and even the minimum possible P_{sense} varies significantly from fiber to fiber. But plotting these parameters as a function of the fiber bandwidth clearly demonstrates the fundamental relationship between bandwidth and number of feedback taps, shown in Fig. 5.1.

The use of SRE to increase the fiber bandwidth can minimize the required complexity of the DFE, [72]. Simulation at 2.5 Gb/s test BER versus optical SNR for three cases of equalization, shown in Fig. 5.2: i) SRE alone, ii) SRE with NB=1 DFE, and iii) standard detection with NB=3 DFE. Note that error-free transmission at 2.5 Gb/s is not possible

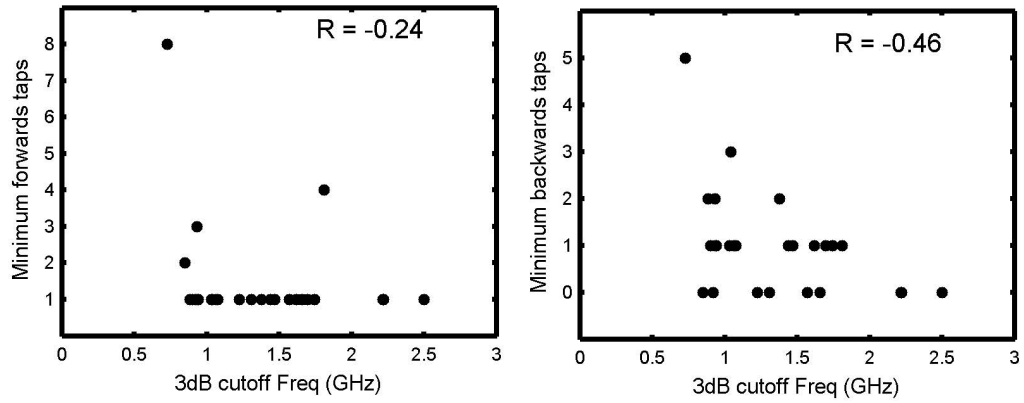


Figure 5.1: Correlation between minimum DFE taps and channel bandwidth.

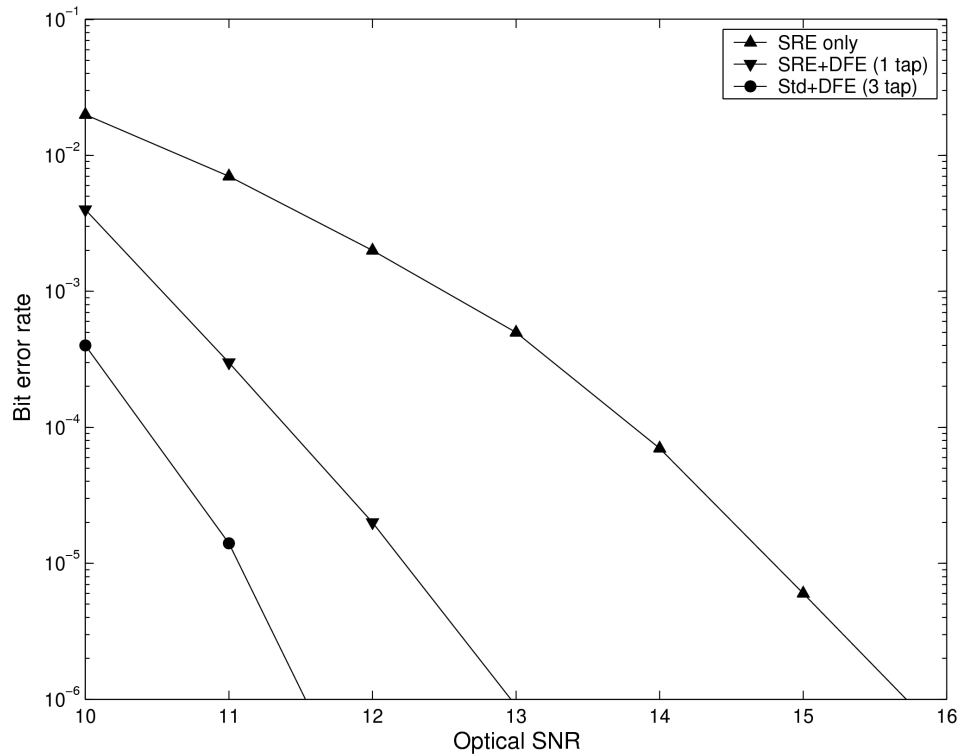


Figure 5.2: BER versus optical SNR at 2.5 Gb/s with different equalization [72].

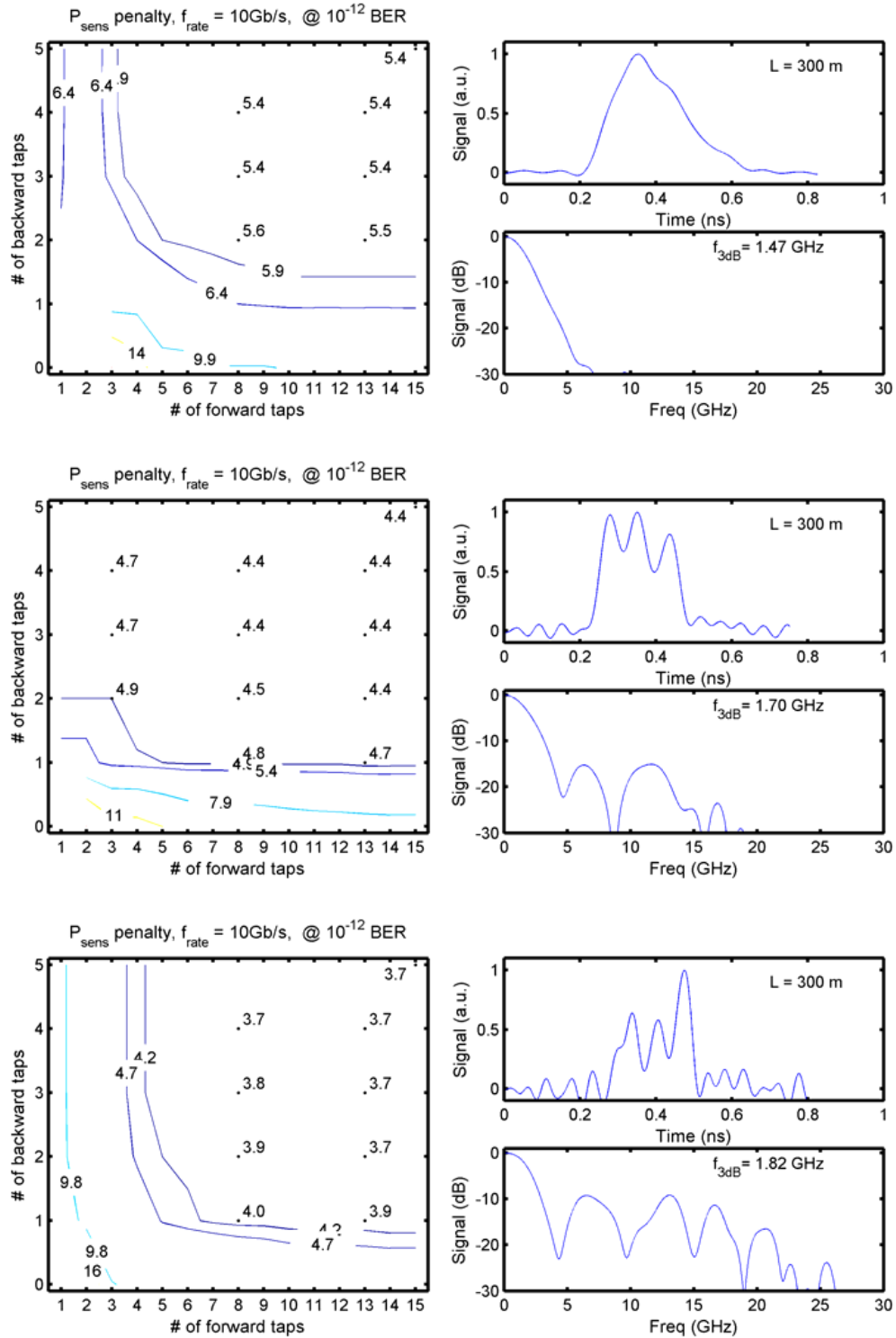


Figure 5.3: ISI penalty versus number of DFE taps (forward taps NF, and backward tap NB) for three samples of 300-m MMF [73].

without equalization.

Clearly, an improvement in sensitivity is observed when DFE is employed, with or without SRE. However, the complexity of the DFE is reduced significantly from 3 taps to 1 with the use of SRE. This simplification in DFE may be the difference between impossible and possible implementation of DFE at higher data rates such as 10 Gb/s.

5.2 Forward error correction

Forward error correction increase works by reserving some portion of the bandwidth for transmission of redundant data so that errors due to system degradation are corrected in real-time, increasing the capacity of the channel. FEC block codes, such as Reed-Solomon (RS) codes with hard-decision decoding [77], are now widely employed in most modern long-haul SMF links [78]. Hence, RS codes are the first type of codes we consider for an MMF link. The second type of FEC codes we suggest are the recently introduced turbo product codes (TPC) [79], which use soft-decision decoding [77].

Reed-Solomon (RS) codes are denoted as $RS(n,k,\delta)$, where n , k and δ are codelength, number of information symbols and minimum Hamming distance [77]. RS codes are non-binary linear block codes of length $n = q^m - 1$ with q^m -ary symbols. For a binary communication system, we have $q = 2$ and m bits are grouped together to form one 2^m -ary symbol. Of particular interest for optical communications is the $RS(255,239,17)$ code due to its low redundancy. With a code rate of $R_c = k/n = 239/255 = 0.93$, this code has only 7% overhead, and an error correcting capability of $t = 64$ bits. This means that at the transmitter side, the data stream is broken up into blocks of 1912 bits which are encoded to form codewords each of length of $255 \times 8 = 2040$ bits, [77].

Considering iterative soft-decision decoding algorithms, the implementation complexity of parallel concatenated convolutional turbo codes is high when compared to turbo product codes (TPC) [79], [80]. TPCs can achieve performances near the Shannon limit and are very suitable for high data rate applications, [77], [81]. A product code has parameters $(n_1n_2, k_1k_2, \delta_1\delta_2)$ and is obtained by placing the information symbols in a $k_1 \times k_2$ array and

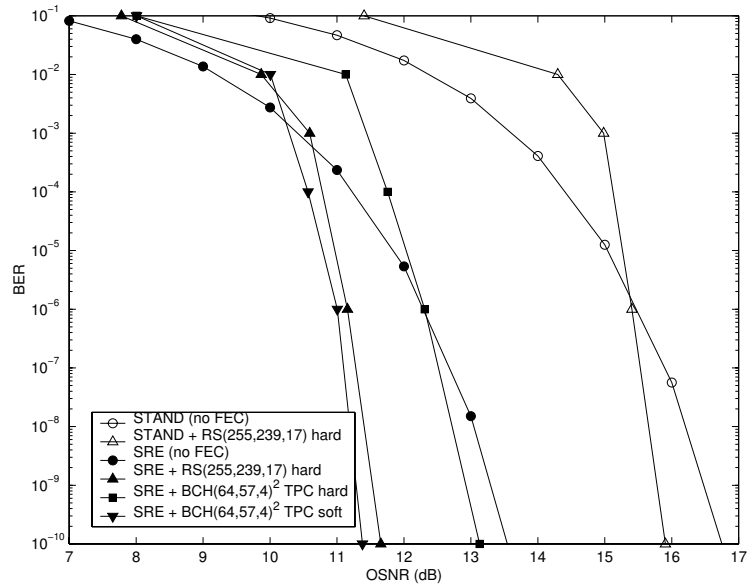


Figure 5.4: BER vs. optical SNR at 1.25 Gb/s (STAND denotes standard detection) [74].

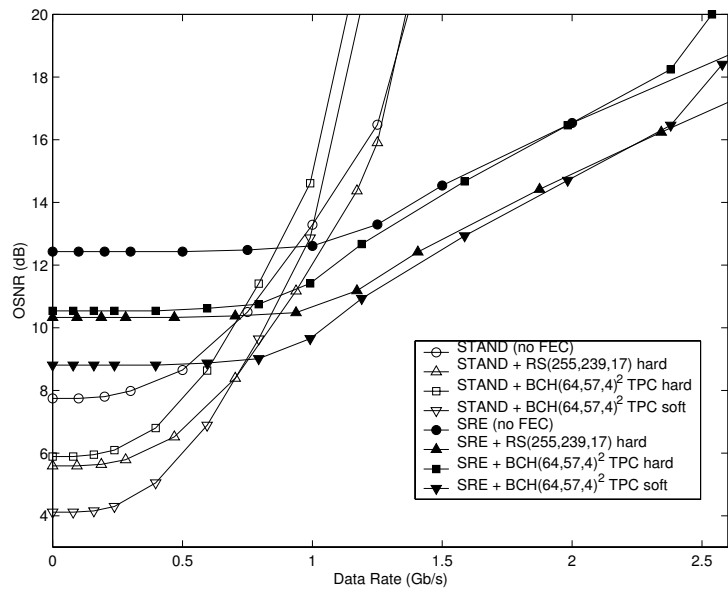


Figure 5.5: Required receiver sensitivity for 10^{-9} BER [74].

encoding the columns and rows with linear block codes $C_1(n_1, k_1, \delta_1)$ and $C_2(n_2, k_2, \delta_2)$, respectively. Codes C1 and C2 are called constituent or component codes. Due to their structure, product codes are efficient against both random and burst errors.

It is observed with simulation that the combination of soft-decision TPC and standard detection is optimum for low data rates below 0.4 Gb/s, where approximately 4-dB coding gain can be achieved if compared to uncoded standard detection, Fig. 5.5. At these low data rates, thermal noise is the main limiting factor at the receiver side. As the data rate exceeds 1 Gb/s, ISI starts to be dominant and SRE detection becomes advantageous. At high data rates, FEC alone is not efficient due to code redundancy. Standard detection becomes impossible at 1.5 Gb/s, whereas SRE enables data rates up to 3.25 Gb/s. Considering decoder complexity, SRE + RS(255,239,17) proves to be the best combination for MMF links at high data rates.

5.3 Improved diversity combining

We explore improved trade-off between bandwidth gain and loss with the use of a Viterbi decoder and a multisegmented photodetector [75]. The decoder unravels the distortion of a channel using information learned from mapping observed outputs of the unknown system to known inputs. With this mapping, the unknown input signal can then be decoded from measured output signal.

A Viterbi decoder may be used with a conventional MMF link. Although the Viterbi algorithm uses the optimum approach to compensate ISI, this implementation is not an easy task, especially since the number of states and the decoder depth of the Viterbi algorithm are extremely high at beyond 1 Gb/s. Therefore, an alternative attractive low-cost solution is an MSD and DFE combination. The individual photocurrents of the MSD are combined using an Viterbi optimized combiner, Fig. 5.6. Indeed, Viterbi decoders are similarly used for diversity combining in wireless links [82], [83]. The numerical fiber link model includes a Viterbi decoder. The DFE is implemented with ten feedforward and ten feedback taps. The Viterbi algorithm has 64 states and a decoder depth of 30 bits [18], [84].

Data transmission at 2.5 Gb/s is simulated with a properly coded Viterbi algorithm. The resulting bit-error rate (BER) versus electrical SNR curves for several receiver structures are shown in Fig. 5.7. At 2.5 Gb/s, standard single-segment detection fails; therefore, equalization by some combination of MSD and DFE is required at data rates exceeding 2.5 Gb/s. Considering all possible combinations, we observe that the MSD and Viterbi combination comes closest to the ISI-free performance bound and achieves about 13-dB gain for 10^{-6} BER, when compared to MSD-only detection. But equally importantly, comparison of standard and MSD detection with the use of Viterbi shows that, indeed, the diversity available with the MSD provide 3-dB improvement in SNR. Similar performance curves are observed when the simulations are run at 1.25, 5, and 10 Gb/s.

5.4 Summary

The preferred embodiment of SRE focuses on the use of multisegment photodetector with simple method of equalization by subtracting the two photocurrents. This is motivated by the need for cost-effective solutions in MMF networks. However, as silicon technology improves, it is inevitable EDC will be play an increasing role. It is well known that the ideal implementation of EDC are efficient in improving channel bandwidth, but the reality is that limitation in electronics will never allow such idealization. As electronics improve, the transmission rate will increase. We have shown, however, that the use of the MSD with the multimode fiber, as either pre-compensation or to provide additional information on the channel, can bridge the gap between the ideal and the attainable.

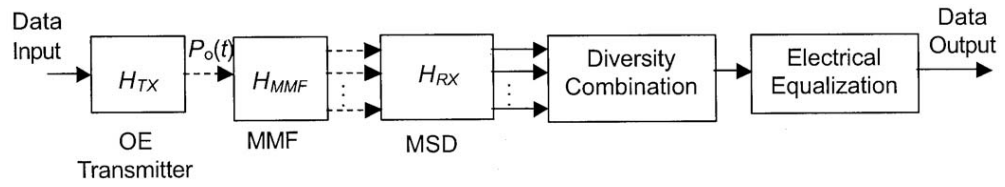


Figure 5.6: Block diagram of Viterbi-optimized, MSD-enhanced MMF link. [75]

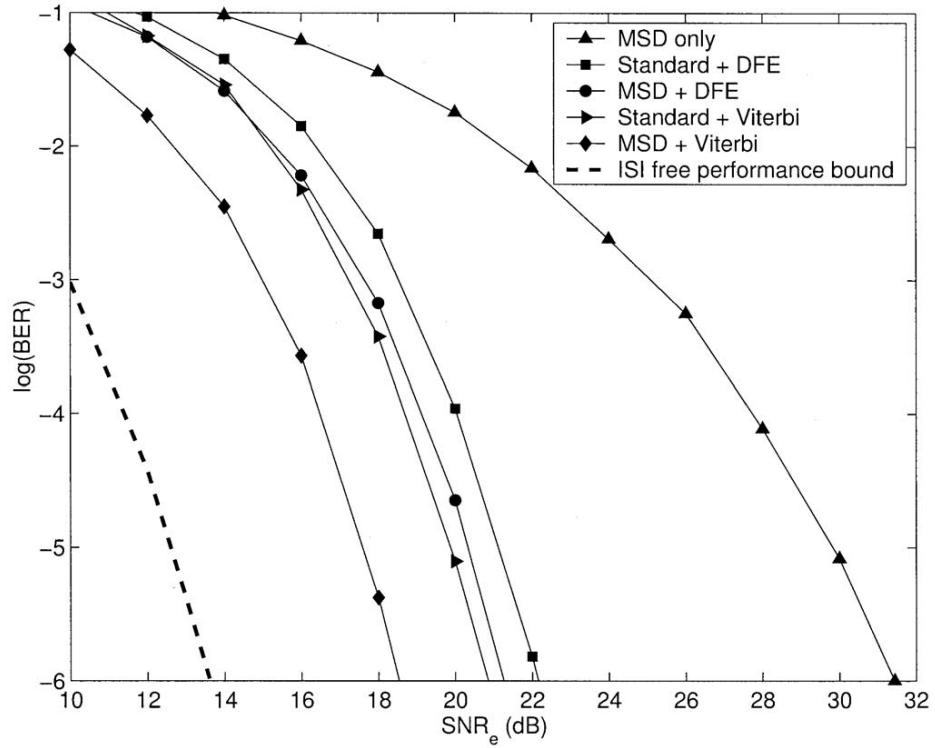


Figure 5.7: Bit error rate versus electrical SNR for various receiver configurations. [75]

CHAPTER 6

CONCLUSION

The driving factor for the use of multimode fiber is its ease-of-use. The demand for bandwidth in customer networks such as local area network and fiber-to-the-premises makes optical solutions attractive. But the burdens of ownership and installation, placed on the individual users, require an extremely simple and cost-effective solution. Multimode fiber provides these benefits; however, it comes at the cost of and limited bandwidth. We show that with a multi-segmented photodetector the limitation in bandwidth can be cut in half.

Whereas bandwidth limitation in copper co-axial cables is due mainly to frequency dependent attenuation, in multimode fiber the limitations are due to intermodal dispersion. The conflicting modes may be separated and compensated for with the use of a multisegment photodetector. This spatially resolved equalization is accomplished by partial separation of the modes with a simple two-segment square-law detector. The power in the high-ordered modes is suppressed by subtraction of the two photodetector signals. The intermodal dispersion can be reduced by a half.

A numerical model of the fiber and the communication link is presented. For the modes of a typical fused-silica graded-index multimode fiber, the computation clearly demonstrates a monotonic relationship between the size of the irradiance profile and the group delay. Moreover, useful mode separation with an MSD is shown to be possible.

Numerical modelling of the fiber link shows that a two-segment photodetector, where the photocurrents are subtracted, can indeed enhance mode selectivity. Even for a wide-ranging source-coupling conditions, a 2 \times gain in fiber bandwidth is achieved. Moreover, the results show that such performance can be achieved with a wide range of device configurations:

its size or its position with respect to the fiber. Even alignment tolerance comparable to the multimode fiber itself is maintained. Moreover, the subtraction of the residual outer PD signal is shown to be necessary to fully exploit the spatial diversity of the MMF signal. Some analysis of the noise shows that modal noise could be an issue, more so than with normal MMF link; however, this noise can be managed with the proper use of low coherence transmitter sources.

In addition to the numerical modelling, experimental measurements are made with fabricated MSD devices. A MSM type photodetector is fabricated on an InGaAs detection substrate. This allows for testing at wavelengths ranging from 850 to 1550 nm. The use of MSM technology also allows for simple comparison between conventional and MSD detection. By adjusting the bias polarity, the PD photocurrents may be added or subtracted.

Significant portions of the testing involve measurement of fiber link impulse response. Despite some simplification made to the simulation, experimental results confirm most of the conclusions drawn by numerical analysis. The measurement conflicted, to some extent, with the numerical modelling of the inherent MMF response; however, with regards to SRE, the numerical and empirical results matched well. The robustness of SRE to variation in fiber sample, launch condition, fiber type, wavelength, MSD geometry, and misalignment are demonstrated. Indeed, 2 \times gain in bandwidth can readily be achieved under these varied conditions with almost an arbitrary MSD design.

Some data link tests are performed with the fabricated device. Eye diagrams for 1550 and 850 nm link are measured at 1.25 Gb/s. Both vertical and horizontal eye openings are significantly improved with SRE. A bit error rate measurement at 1.25 Gb/s is made as well. A link with prohibitively high ISI results in a 10^{-2} BER floor, preventing error-free detection even with high input power levels. With SRE, however, the ISI limited link is made noise limited. Some limitations in the implementation prevents testing at high data rates such as 2.5 and 10 Gb/s. These factors, however, are not fundamentally related to SRE and can readily be circumvented with detailed attention to fabrication procedures.

CHAPTER 7

SUGGESTED FUTURE WORK

The dissertation addressed issues of spatial diversity in multimode fiber. The work presented here shows a useful diversity and by using a simple two-segment photodetector, any power in the high-ordered modes that cause ISI can be suppressed by simple subtracting the photocurrents of properly sized PD segments. However, some additional work can address some limitation in the current numerical model and experimental results.

7.1 Device fabrication

7.1.1 Improvements to bandwidth and quantum efficiency

Much of the testing has been done with measured impulse response. While this is widely accepted as a fair measure of the fiber bandwidth, ultimate measure of performance is the efficiency of data transmission, the error rate in the received signal. Some attempts have been made and presented here in verifying performance by transmission error rates but with limited success up to 1.25 Gb/s. Testing at increased data rates such as 2.5 and 10 Gb/s is highly desirable but were un-achievable due to issues related to fabrications limit the photodetector in terms of quantum efficiency and bandwidth. In neither case is the detector operating at the fundamental limits. Indeed, commercial manufacturers routinely produce high-quality detectors for use up to 10 Gb/s. To that end, and improved device fabrication, either in-house or by an external foundry, can lead to improved qualification of SRE.

7.1.2 Implementation of SRE with a *p-i-n* diode

The device used for experimental measurements were fabricated with MSM technology. This was chosen because of the simplicity in fabrication as well as flexibility MSM offer with respect to bias polarity. However, practical photodetectors are routinely made in *p-i-n* diode technology, for two main reasons. First, the Schottky junction contact are made of gold and titanium which obscure some of the optical signal resulting in a non-unity external quantum efficiency. With *p-i-n* diode, the contacts can be made to maximize quantum efficiency, thus the receiver sensitivity. Second issue with MSM is planar geometry resulting in high surface state density in the absorbing semiconductor. This results in slow hole transport which is apparent in a long tail in the temporal impulse response or low-frequency gain in the frequency response [85], [86]. This reduces the usable bandwidth of the MSM photodetector. SRE does not fundamentally restrict the PD technology and *p-i-n* diode do not exhibit these effects; however, others issues related to the technology might present difficulties. Namely, with *p-i-n*, capacitance per unit area can be significantly larger than with MSM. For high-speed data link, *p-i-n* diode are limited to 20–40 μm in diameter. In contrast, the MSM devices used in the work present here were 200 μm in diameter. With the MSM devices, the fiber core diameter restricted the inner PD segment to 30- μm in diameter, if used in the near-field. To maintain low capacitance, future efforts can look to the effect of an intermediate lens on the spatial diversity. Or alternatively, the use of a two-segment PD that only partially detects the optical signal can be studied. In this way low device capacitance can be maintained. Indeed, it may also be possible that comparable bandwidth gain can be achieved with less optical power penalty.

7.2 Improved diversity combination

Finally, improved methods of diversity combining can be studied. The results presented in this dissertation represent the simplest form of spatially resolved equalization. Only a single segment PD that partially detects the optical signal can be simpler, and we have been shown to be ineffective. Obviously, a more sophisticated method of combining PD photocurrents

can result in improved bandwidth performance and less optical loss. However, the added improvements must be measured against the added complexity. The results presented here should be used as a benchmark against which improved link enhancement should be measured with respect to added complexity. Some possible advances in SRE that should be considered include:

- Combination of the two-segment photocurrents with adjustable or discrete weighting factors.
- Decision-based photocurrent combination
- Partial detection of the high-ordered mode with a outer PD smaller than the full optical spot.
- Photocurrent subtraction with time adjustment.
- Segmentation of the PD beyond two segments.
- Simultaneous use of multiple wavelength and a multisegment photodetector.
- Simultaneous use of segmented transmitter and photodetector.

It is not the belief of this author that the experimental work presented in this dissertation is the final word in spatially resolved equalization. These results are merely first step that needed to be taken to exploiting spatial information available in multimode fiber.

APPENDIX A

FINITE DIFFERENCE METHOD FOR MODE SOLVING

The scalar wave equation is solved, numerically, by approximating the derivative of $f(r)$ with a finite difference between discrete positions r_i . That is,

$$\frac{d}{dr}f(r_i) \approx \frac{f(r_{i+1}) - f(r_{i-1}))}{r_{i+1} - r_{i-1}}, \quad (\text{A.1})$$

and

$$\frac{d^2}{dr^2}f(r_i) \approx \left[\frac{f(r_{i+1}) - f(r_i)}{r_{i+1} - r_i} - \frac{f(r_i) - f(r_{i-1}))}{r_i - r_{i-1}} \right] \frac{2}{r_{i+1} - r_{i-1}}, \quad (\text{A.2})$$

As a results, the differential equation,

$$\frac{d^2 R(r)}{dr^2} + \frac{1}{r} \frac{dR(r)}{dr} + \left(k_o^2 n^2(r) - \beta_m^2 - \frac{\nu^2}{r^2} \right) R(r) = 0, \quad (\text{A.3})$$

can be approximated as

$$a_{i,i-1}R_{i-1} + a_{i,i}R_i + a_{i,i+1}R_{i+1} = \beta^2 R_i, \quad (\text{A.4})$$

where

$$\begin{aligned} a_{i,i} &\equiv -\frac{2}{(r_i - r_{i-1})(r_{i+1} - r_i)} + k_o^2 n^2(r_i) - \frac{\nu^2}{r_i^2}, \\ a_{i,i-1} &\equiv \frac{2}{(r_i - r_{i-1})(r_{i+1} - r_{i-1})} - \frac{1}{r_i(r_{i+1} - r_{i-1})}, \\ a_{i,i+1} &\equiv \frac{2}{(r_{i+1} - r_i)(r_{i+1} - r_{i-1})} + \frac{1}{r_i(r_{i+1} - r_{i-1})}, \end{aligned}$$

and

$$R_i \equiv R(r_i).$$

The approximation can be recast as an eigenvalue problem that can be readily solved numerically:

$$\mathbf{A}\bar{R} = \beta^2\bar{R}, \quad (\text{A.5})$$

where \bar{R} and β^2 are the eigenvector and eigenvalue, respectively, of the matrix \mathbf{A} , which is a tridiagonal matrix. Of \mathbf{A} , the main diagonal elements are given by $a_{i,i}$, the left diagonal elements are given by $a_{i,i-1}$ and the right diagonal elements are given by $a_{i,i+1}$. All values of $n(r_i)$, k_o and ν are known. The eigenvalue of (A.5), is solved using a standard eigenvalue solver in MATLAB[©].

The domain of r over which the modes are computed is between $r > 0$ and $r = 3a$, where a is the core radius. Because of the discontinuity in ν^2/r^2 in (A.3), $r_i \neq 0$.

The solution of (A.5) are the eigenvalue and eigenvector of guided and unguided fiber modes. However, only the guided modes, where the solution satisfies

$$\min[n(r)k_o] < \beta_m < \max[n(r)k_o] \quad (\text{A.6})$$

are retained. The corresponding eigenvector is computed using the standard MATLAB routine. Only the value of $R(r_i)$ where $|r_i| \geq 0$ are kept.

APPENDIX B

SIMULATION CODE

B.1 Matlab code: RadialModeSolver.m

Matlab code to compute radial component of scalar wave equation (2.8). Compute mode for a give azimuthal mode number; returns both phase velocity and radial profile. This function calls `GenRadialDiffEqMesh.m`, which generates the mesh in radial domain for optimal mode solving. This function also calls `Alpha_n.m` which is the function describing the fiber core refractive index.

```
(001) % Author: Ketan M. Patel
(002) % Copyright: 2003
(003) % Ver: 1.2000
(004)
(005) function [beta,R,tau,A] = RadialModeSolver(fiber, dr_max, L, lambda)
(006)
(007) % compute solution to radial scalar wave equation
(008) %  $D^2 R(r) + 1/r D R(r) + [ (k_0 * n(r))^2 - (L/r)^2 ] R(r) = \text{beta}^2 R(r)$ 
(009) %
(010) % with the following approximations
(011) %
(012) % 
$$D R(r) = \frac{R(i+1) - R(i-1)}{r(i+1) - r(i-1)}$$

(013) %
(014) %
(015) % 
$$D^2 R(r) = \frac{\frac{R(i+1) - R(i)}{r(i+1) - r(i)} - \frac{R(i) - R(i-1)}{r(i) - r(i-1)}}{r(i+1) - r(i-1)}$$

(016) %
(017) %
(018) %
(019) %
(020) %
(021) %
(022) %
(023) %
(024) % thus turning into eigenvalue problem
(025) %
(026) % inputs:
(027) % fiber -> fiber parameters (see function stored in fiber.function)
(028) % fiber.function -> string storing function used for evaluation of
(029) % fiber index profile (required)
(030) %
(031) % dr_max -> maximum allowed step size for radial mesh
(032) % L -> azimuthal mode number: sin(L*phi); cos(L*phi)
(033) % lambda -> freespace wavelength
(034)
(035)
(036) options.disp = 0;
```

```

(037) options.maxit = 300;
(038) c = 299792458;
(039)
(040) % mesh radial coordinates
(041) r = GenRadialDiffEqMesh(fiber,dr_max,lambda,L);
(042) index = feval(fiber.function,r,fiber);
(043)
(044) % define delta's given that r can be arbitrary step sizes
(045) % delta_0 -> r(i) - r(i-1)
(046) % delta_1 -> r(i+1) - r(i)
(047) % delta_2 -> r(i+1) - r(i-1) = delta_0 + delta_1
(048)
(049) delta_0 = r(2:end) - r(1:end-1);
(050) delta_1 = r(3:end) - r(2:end-1);
(051) delta_1(end+1) = delta_1(end); % fix end point of delta_1
(052) delta_2 = delta_0 + delta_1;
(053)
(054) % remove r=0 point for subsequent computations
(055) r(1) = [];
(056) index(1) = [];
(057)
(058) % set slope of R at r=0
(059) dR0 = mod(L,2);
(060)
(061) % compute freespace wave vector
(062) k0 = 2*pi/lambda;
(063) N = length(r);
(064)
(065) % compute diagonals of scalar wave equation matrix
(066) %
(067) % [diagC digaR 0 ] * R = beta * R
(068) % [diagL diagC diagR]
(069) % [ 0 diagL diagC]
(070) %
(071) % i.e. R(i+1) * diagR(i) + R(i) diagC(i) + R(i-1) * diagL(i) = beta * R(i)
(072)
(073) K2 = (k0 * index).^2 - (L./r).^2;
(074)
(075) diagC = -2./(delta_1 .* delta_0) + K2; % center diagonal
(076) diagL = (2./delta_0 - 1./r) ./ delta_2; % left diagonal
(077) diagR = (2./delta_1 + 1./r) ./ delta_2; % right diagonal
(078)
(079) % for end points, the boundary value must be folded into elements of matrix
(080) % for i=0 (i.e. r(i=0) = 0) the slope is either 0 or 1
(081) % for slope of 1, R(i) = 0
(082) % for slope of 0, R(i) = R(i+1) = R(i-1)
(083) % thus eigen eq. is
(084) % R(i+1) * diagR(i) + R(i) diagC(i) + R(i) * diagL(i) = beta * R(i)
(085) % so for i=1, the diagL(i) term is folded into diagC(i) if R(i) can be non-zero
(086)
(087) diagC(1) = diagC(1) + ~dR0 * diagL(1);
(088)
(089) % similarly for i=end (last point), the boundary value must be folded into diagC
(090) % however, the slope of R(i) is forced to be 0 and R(i) = 0
(091) % thus eigen eq. is
(092) % 0 * diagR(i) + R(i) diagC(i) + R(i) * diagL(i) = beta * R(i)
(093) % and diagR(end) folds into diagC(end) trivially
(094)
(095) diagC(end) = diagC(end) + 0 * diagR(end);

```

```

(096)
(097) % create sparse matrix with diagonals
(098) A = spdiags(diagC',0,N,N);
(099) A = spdiags(diagL',1,A); % insert into right side but later transpose matrix
(100) A = spdiags(diagR',-1,A); % insert into left side but later transpose matrix
(101)
(102) A = A'; % transpose matrix
(103)
(104) % estimate number of solutions to wave equation
(105)
(106) beta_min = k0*index(end); % compute minimum possible beta
(107) kt = sqrt(K2-beta_min^2); % compute maximum tranverse wave number
(108) pos = find((r>0) & (kt.^2 > 0)); % find where kt is real
(109) dr = diff(r);
(110)
(111) % integrate kt to estimate # of nodes in highest order mode (i.e. mode number)
(112) % integrate only where kt^2 > 0 (and in r>0 domain)
(113)
(114) M = ceil( kt(pos) * dr(pos)' / pi);
(115) M = M+1; % padM to allow for error in estimate
(116)
(117) % find M eigenvalues (beta^2) closest to maximum possible of beta^2
(118)
(119) [R,beta2] = eigs(A,M,max(k0*index)^2,options);
(120) beta = diag(sqrt(real(beta2)));
(121)
(122) % sort for unique beta (remove degenerate values) and keep guiding modes (beta > k_min)
(123) idx = find(beta > beta_min);
(124) beta = beta(idx);
(125) R = R(:,idx);
(126)
(127) if isempty(beta)
(128) R = [];
(129) tau = [];
(130) return
(131) end
(132)
(133) [dmp,idx] = max(abs(R), [], 1);
(134) scale = diag(R(idx,1:length(idx)))';
(135) scale = repmat(scale,[size(R,1),1]);
(136) R = R ./ scale;
(137)
(138) % replace smallest value of r with 0
(139) r(1) = 0;
(140) if (L~=0)
(141) R(1,:) = 0;
(142) end
(143)
(144) if (nargout > 2)
(145)
(146) % compute group-delay (i.e. d_beta / d_omega) via pertubation method
(147)
(148) DeltaF = 1/2 * (1 - (index/fiber.n1).^2);
(149) P = (2 - DeltaF*(fiber.y + 4));
(150)
(151) for j = 1:length(beta)
(152) [RH_vec,dmp] = eigs(A',1,beta(j)^2,options);
(153) R_vec = R(:,j);
(154)

```

```

(155)     [dmp,idx] = max(abs(RH_vec), [], 1);
(156)     RH_vec   = RH_vec ./ RH_vec(idx);    % RH_vec is vector,
(157)     num     = RH_vec' .* P * R_vec;
(158)     den     = RH_vec' * R_vec;
(159)     tau(j)  = fiber.length * fiber.N1 / (2*c) * ...
(160)             (fiber.n1 * k0 / beta(j)) * num/den;
(161)     end
(162) end
(163)
(164) % optionally plot eigenfunction
(165) if (0)
(166)     clf; hold on;
(167)     iidx = round(linspace(1,length(r),101));
(168)     plot(r(iidx)/lambda,R(iidx,:), 'k.-');
(169)     pause(0.1);
(170) end
(171)
(172) % put radial position as first column of output matrix R
(173) R(:,2:end+1) = R;
(174) R(:,1)      = r';

```

B.2 Matlab code: GenRadialDiffEqMesh.m

Matlab code that generates the mesh in the radial domain for RadialModeSolver.m. This function calls Alpha_n.m which is the function describing the fiber core refractive index.

```
(001) % Author: Ketan M. Patel
(002) % Copyright: 2003
(003) % Ver: 1.0000
(004)
(005) function r_mesh = GenRadialDiffEqMesh(fiber,dr_max,lambda,L);
(006)
(007) % generate mesh for radial profile differential equation
(008) % compute solution to radial scalar wave equation
(009) %  $D^2 R(r) + 1/r D R(r) + [(k_0 * n(r))^2 - (L/r)^2 - \text{beta}^2] R(r) = 0$ 
(010) %
(011)
(012) % inputs:
(013) %   index_func   -> handle for function that describes index profile
(014) %                   e.g. @alpha_n
(015) %   fiber        -> struct store info describing fiber profile
(016) %                   i.e. structure necessary to evaluate @fiber.function
(017) %   dr_max       -> maximum step size for mesh
(018) %   lambda       -> wavelength of mode propagation
(019) %   L            -> azimuthal mode number assumed for diff. eq. solution
(020)
(021) N_divide = 250; % number of steps to divide transverse wave by
(022) TOL      = 0.05; % error tolerance of approx. made for exponential decay regions
(023) MAX_DIFF = 1000; % maximum differential step size for 1/r_mesh
(024)
(025) r_max = fiber.a; % radius at which R will be evanescent
(026)
(027) k0 = 2*pi/lambda;
(028) r_init = [fiber.a 0:lambda/10:3*r_max];
(029) r_init = unique(r_init);
(030) index = feval(fiber.function,r_init,fiber);
(031) k_max = k0 * max(index);
(032) k_min = k0 * min(index);
(033) beta_min = k_min; % minimum possible value of guided-mode wave number
(034) beta_max = k_max; % maximum possible value of guided-mode wave number
(035)
(036) if (nargin < 6)
(037)     L = 1;
(038) end
(039)
(040) % compute highest possible transverse wave number
(041) kt2 = (k0 * index).^2 - (L./(r_init+1e-99)).^2 - beta_min^2;
(042)
(043) mask = kt2 > 0; % mask where profile is oscillatory
(044)
(045) if isempty(find(mask))
(046)     r_mesh = [];
(047)     return
(048) end
(049)
(050) r1 = r_init(min(find(mask))); % lower boundary of guiding region
(051) r2 = r_init(max(find(mask))); % upper boundary of guiding region
(052) % r2 = fiber.a;
(053) % compute appropriate step size for shortest transverse wave (i.e. transverse sin wave)
(054) dr1 = 2*pi/sqrt(max(kt2)) / N_divide;
(055)
```

```

(056) dr1 = min(dr_max,dr1);
(057)
(058) % refine mesh outside guiding region, in cladding area
(059) % for exponention decay of rate A, step size of DX will result in error E
(060) % given by: exp(A*DX)*(1-A*DX) = 1 - |E| = (1+DX*A) * (1-DX*A)
(061) % optimal is given approximately by: DX = sqrt(|E|/2A^2)
(062)
(063) gamma = abs(sqrt(beta_max^2 - k_min^2));
(064) dr2 = sqrt(TOL / (2*gamma^2));
(065) dr2 = min(dr_max,dr2);
(066)
(067) % refine mesh inside guiding region, i.e. fiber center
(068) gamma = abs(sqrt(beta_max^2 - (k0*index(1))^2 - (L/((r1+1e-99)/2))^2));
(069) dr0 = sqrt(TOL / (2*gamma^2+1e-99));
(070) dr0 = min(dr_max,dr0);
(071)
(072) if r1==0
(073)     r1 = dr1;
(074) end
(075)
(076) r_mesh = [dr0/100 linspace(0,dr0,20) ...
(077)           (dr0:dr0:r1) (r1:dr1:r2) (r2:dr2:(3*fiber.a)) fiber.a];
(078) r_mesh = unique(r_mesh);
(079)

```

B.3 Matlab code: Alpha_n.m

Matlab code to describe the fiber core refractive index profile. Uses a **struct** type variable to store information about fiber.

```
(001) % Author: Ketan M. Patel
(002) % Copyright: 2003
(003) % Ver: 1.0000
(004)
(005) function n = alpha_n(r,fiber)
(006)
(007) % index profile
(008) %   inputs   r           -> radial positions for which n is desired
(009) %           fibers -> parameters of fiber
(010) %           fiber.n1   -> core index
(011) %           fiber.alpha -> fiber alpha
(012) %           fiber.a    -> fiber core radius
(013) %           fiber.delta -> fiber contrast
(014) %                               i.e. delta = ~(n_core-n_clad)/n_core
(015) %           fiber.function -> 'alpha_n'
(016) %
(017) %  $n^2 = n_c^2 * (1 - 2 * \delta * (r/a)^2)$ 
(018)
(019) % use default params if none is specified (use 50-um Corning MMF)
(020) if (nargin<2)
(021)     fiber.n1   = 1.499;
(022)     fiber.alpha = 2;
(023)     fiber.a    = 25e-6;
(024)     fiber.delta = 0.01;
(025)     fiber.function = 'alpha_n';
(026) end
(027)
(028) % if no arguments, return template for fiber (use 50-um Corning MMF)
(029)
(030) if (nargin==0)
(031)     n=fiber;
(032)     return
(033) end
(034)
(035) if (fiber.alpha < 1000)
(036)     r = abs(r);
(037)     r = min(r,fiber.a);           % for r larger than core radius,
(038)                                     % fix it to a so that proper value of n is returned
(039)     n = fiber.n1*sqrt(abs(1-2*fiber.delta*(r/fiber.a).^fiber.alpha));
(040) else
(041)     n = ones(size(r))*fiber.n1;
(042)     idx = find(abs(r) >= fiber.a);
(043)     n(idx) = fiber.n1 * sqrt(abs(1-2*fiber.delta));
(044) end
(045)
(046)
```

B.4 Matlab code: ComputeModeCoupling.m

Matlab code to compute mode coupling, by 2-dimension overlap integral, of incident electric field to fiber mode profile. The rotation degeneracy of the fiber modes can be accounted for by using complex field amplitude. The real part stores the $\cos(\nu\phi)$ while the imaginary part store the expression for $\sin(\nu\phi)$.

```
(001) % Author: Ketan M. Patel
(002) % Copyright: 2003
(003) % Ver: 1.0000
(004)
(005) function [Ceff] = ComputeModeCoupling(E,E_src)
(006)
(007) % USAGE: [Ceff] = ComputeModeCoupling(E,E_src)
(008) %
(009) % compute mode power coupling efficiency into mode with 2D profile E, from
(010) % illumination with 2D field profile given by E_src
(011) % this computation does not include Fresnel reflection coefficient due to
(012) % mismatch in incident wave numbers
(013) %
(014) % mode coupling is normalized by "power" of the field profiles
(015) %
(016) % input:
(017) % E      -> array of modal E-field profile (NxNxM)
(018) %         use complex E for rotational degeneracy (i.e. exp(-L*phi)
(019) % E_src   -> REAL, instantaneous transverse electric field at mode interface
(020) %
(021) % E and E_src are assumed to be same step size and span in x,y direction
(022) % only a 2-dimension (X by Y) source profile may be used
(023) % E may be 3-dimensional i.e. X by Y by N size array where N is the
(024) % number of fiber modes to consider
(025) % Ceff will be computed for each mode profile index by N
(026)
(027) E_src = real(E_src); % make sure only real e-field is used
(028) SRC_PWR = E_src(:)'*E_src(:); % compute power in Illuminaiton profile
(029)
(030) if SRC_PWR ~= 0
(031)
(032)     mat_size = size(E); % get size of E matrix to create mask
(033)     mat_size(1:2) = 1;
(034)
(035)     SRC_MAT = repmat(E_src,mat_size);
(036)     Mode_PWR = abs(squeeze(sum(sum(E.*real(E)))));
(037)     Mode_PWR(find(Mode_PWR == 0)) = 1e-99;
(038)
(039)     % compute E-field coupling efficiency by overlap integral
(040)     % real(Ceff) is coupling to R(r) cos(l*phi) mode
(041)     % imag(Ceff) is coupling to R(r) sin(l*phi) mode
(042)     % compute POWER coupling and normalize by mode and source "power"
(043)
(044)     Ceff = squeeze(sum(sum(E.*SRC_MAT))); % compute overlap integral
(045)     Ceff = abs(Ceff).^2 ./ Mode_PWR / SRC_PWR ; % square and normalize
(046)
(047) else
(048)     Ceff = ones(size(E,3),1); % if no source is specified,
(049) % assume unity coupling for each mode
(050) end
```

APPENDIX C

FABRICATION PROCEDURE

The following procedure is the recipe for the single-layer MSM device processing used to fabricate the SRE MSM. A representative device layout is shown in, Fig. C.1. The 1–1.5 μm layer of photoresist is spun onto a semiconductor substrate, Fig. 3.3. Through contact photolithography, the photoresist (PR) is patterned (negative pattern) with the structure for a metal lift-off process. A layer of 40 nm of titanium (Ti) followed by 200-300 nm of gold (Au). The photoresist is then washed away with acetone to leave behind a pattern of Ti/Au that produces a Schottky barrier with the GaAs or InGaAs substrate and is used directly as the MSM structure.

The substrates used are cleave rectangular pieces from a 2" or 3" wafers. Because of the sharp edges, edge beading becomes an issue, especially for interdigitated structure, where good contact lithography is required. To optimize the contact, the edge bead is removed, prior to mask patterning, by exposing the PR to UV and developing. This results in running the PR through the developer twice, but has only a slight impact on final PR pattern quality. If full wafer is used, skip steps 5 through 11.

1. Standard substrate cleansing procedure (e.g. Acetone, Methanol, Isopropanol, de-ionized water rinse).
2. De-hydrate sample at 120 ° C for 1-2 min. Allow sample to cool properly (place on stainless steel block for heat sinking).
3. Spin photoresist (AZ5214E) at 4000 RPM for 40 seconds.
4. Pre-bake substrate at 120 ° C for 1 min.
5. Place substrate, PR side up, on mask aligner chuck.
6. Remove photomask (i.e. leave sample open to direct UV exposure).
7. Place a clean, 100% opaque substrate of slightly smaller dimension (1 mm on all sides) on top of and centered with the PR substrate. Ensure that corners are exposed.
8. Mask-off center part of wafer sample with another wafer sample of similar shape by slightly smaller dimension. Ensure corner and edge of device substrate are open to UV exposure; ensure center portion of device substrate is obscured to UV exposure.
9. Expose substrate edge to 200-250 mJ of UV.

40 2x5 SMALL

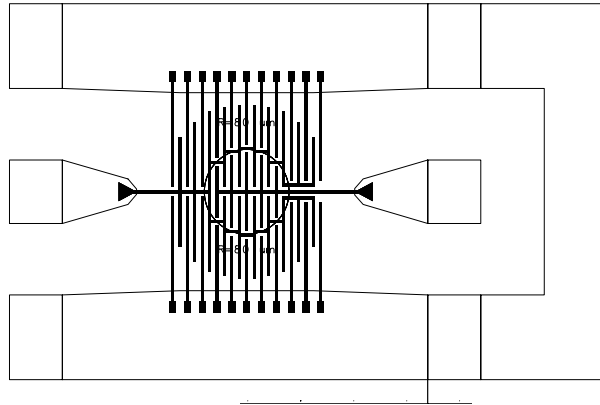


Figure C.1: Spatially resolved equalization MSM mask layout pattern. All structure on a single metal layer.

10. Immerse substrate in developer (AZ300, undiluted concentration) for 20-30 sec until edge bead is developed away. Gently agitate solution during development. To avoid debris contamination, use fresh solution.
11. Rinse with de-ionized (DI) water and gently blow dry with nitrogen.
12. Place substrate, PR side up, on mask aligner chuck. Optionally, place substrate samples of equal thickness along side of device substrate to ensure flat contact between photomask and substrate.
13. Insert photomask into mask aligner.
14. Bring photomask into contact with substrate. Good contact with substrate is critical to good interdigitated structure lift-off.
15. Expose to 75-90 mJ of UV.
16. Immerse substrate in developer (AZ300, undiluted concentration) for 15 sec, gently agitate solution during development.
17. Rinse in DI water and blow dry.
18. NO post bake, deposit metal 40 nm Ti followed by 200 nm of Au.
19. Soak and rinse substrate with Acetone.

REFERENCES

- [1] S. E. Miller, "Light propagation in generalized lens-like media," *Bell Syst. Tech. J.*, vol. 44, pp. 2017–2062, Nov 1965.
- [2] D. Marcus, "Theory of a tabular gradient gas lens," *IEEE Trans. Microwave Theory Tech.*, vol. MTT-13, Nov 1965.
- [3] D. Gloge and E. Marcatili, "Multimode theory of graded-core fibers," *Bell Syst. Tech. J.*, vol. 52, pp. 1563–1578, Nov 1973.
- [4] D. Gloge, "Impulse response of clad optical multimode fibers," *Bell Syst. Tech. J.*, vol. 52, pp. 801–816, July 1973.
- [5] C. N. Kurtz and W. Streifer, "Guided waves in inhomogeneous focusing media. I. Formulation, solution for quadratic inhomogeneity," *IEEE Transactions on Microwave Theory and Techniques*, vol. MTT-17, pp. 11–15, Jan 1969.
- [6] C. N. Kurtz and W. Streifer, "Guided waves in inhomogeneous focusing media. II. Asymptotic solution for general weak inhomogeneity," *IEEE Transactions on Microwave Theory and Techniques*, vol. MTT-17, pp. 250–253, May 1969.
- [7] D. Gloge, E. L. Chinnock, and K. Koizumi, "Study of pulse distortion in Selfoc fibres," *Electron. Lett.*, vol. 8, pp. 526–527, 19 Oct 1972.
- [8] R. Olshansky and D. B. Keck, "Pulse broadening in graded-index optical fibers," *Appl. Opt.*, vol. 15, pp. 483–491, Feb 1976.
- [9] M. Heinzl, "Broadband carriers are hunting for 'Killer Apps'," *The Wall Street Journal*, 14 June 2001.
- [10] D. Richman, "Future of TV may come to you through internet," *Seattle Post-Intelligencer*, Sept 1999.
- [11] J. G. Shinal A. Reinhart, "The worlds most glamorous cottage industry," *Business Week*, Oct 9 2000.
- [12] J. A. Tatum, J. K. Guenter, and R. H. Johnson, "Manufacturability of VCSEL components and VCSEL products," in *Proc. LEOS 1998*, 1998, vol. 2, pp. 409–410.
- [13] J. Tatum, "Packaging flexibility propels VCSELs beyond telecommunications," *Laser Focus World*, vol. 36, pp. 131–136, April 2000.
- [14] IEEE 802.3ae Cabling Survey Ad Hoc, "AT&T 1982 survey of 79 U.S. businesses, 10,000 measured link lengths from TO to BD," June 1999.
- [15] J. A. Tatum and, "The VCSELs are coming," in *Proceedings of the SPIE 2002*, 2002, vol. 4905, pp. 517–526.

- [16] Z. Haas and M. A. Santoro, "A mode-filtering scheme for improvement of the bandwidth-distance product in multimode fiber systems," *J. Lightwave Technol.*, vol. 11, pp. 1125–1131, July 1993.
- [17] W. C. Y. Lee, *Mobile Communications Engineering*, John Wiley & Sons, 1982.
- [18] J. G. Proakis, *Digital Communications*, McGraw–Hill, 1995.
- [19] B. Glance and L. J. Greenstein, "Frequency-selective fading effects in digital mobile radio with diversity combining," *IEEE Transactions on Communications*, vol. COM-31, pp. 1085–1094, Sept 1983.
- [20] S. N. Diggavi, "On achievable performance of spatial diversity fading channels," *IEEE Transactions on Information Theory*, vol. 47, pp. 308–325, Jan 2001.
- [21] R. G. Vaughan, "On optimum combining at the mobile," *IEEE Transactions on Vehicular Technology*, vol. 37, pp. 181–188, Novol 1988.
- [22] P. Balaban and J. Salz, "Optimum diversity combining, equalization in digital data transmission with applications to cellular mobile radio, Part I: Theoretical considerations," *IEEE Trans. Commun.*, vol. 40, pp. 885–894, May 1992.
- [23] S. D. Personick, "Baseband linearity, equalization in fiber optic digital communication systems," *Bell Syst. Tech. J.*, vol. 52, pp. 1175–1194, Sept 1973.
- [24] S. Ariyavisitakul and L. J. Greenstein, "Reduced-complexity equalization techniques for broadband wireless channels," *IEEE Journal on Selected Areas in Communications*, vol. 15, pp. 5–15, Jan 1997.
- [25] M. Abdulrahman, A. U. H. Sheikh, and D. D. Falconer, "Decision feedback equalization for CDMA in indoor wireless communications," *IEEE Journal on Selected Areas in Communications*, vol. 12, pp. 698–706, May 1994.
- [26] J. E. C. Brown, P. J. Hurst, and L. Der, "A 35 Mb/s mixed-signal decision-feedback equalizer for disk drives in 2- μ m CMOS," *IEEE Journal of Solid-State Circuits*, vol. 31, pp. 1258–1266, Sept 1996.
- [27] M. Q. Le, P. J. Hurst, and J. P. Keane, "An adaptive analog noise-predictive decision-feedback equalizer," *IEEE Journal of Solid-State Circuits*, vol. 37, pp. 105–113, Feb 2002.
- [28] J. Wang and J. M. Kahn, "Performance of electrical equalizers in optically amplified OOK and DPSK systems," *IEEE Photonics Technology Letters*, vol. 16, pp. 1397–1399, May 2004.
- [29] O. Agazzi, V. Gopinathan, K. Parhi, K. Kota, and A. Phanse, "DSP-based equalization for optical channels," Presented at IEEE 802.3ae Interim Meeting, 2000.
- [30] F. S. Choa, "10 Gb/s multimode fiber transmissions over any distance using adaptive equalization techniques," Presented at IEEE 802.3ae Interim Meeting, 2000.
- [31] D. C. Wei, D. Q. Sun, and A. A. Abidi, "A 300-MHz fixed-delay tree search-DFE analog CMOS disk-drive read channel," *IEEE Journal of Solid-State Circuits*, vol. 36, pp. 1795–1807, Nov. 2001.

- [32] Y. S. Sohn, S. J. Bae, H. J. Park, and S. I. Cho, "A 1.2 Gbps CMOS DFE receiver with the extended sampling time window for application to the SSTL channel," in *2002 Symposium on VLSI Circuits*, 2002, pp. 92–93.
- [33] J. Walko, "Phyworks starts sampling EDC optical chips," *CommsDesign.com*, 11 Feb 2004.
- [34] L. Raddatz, I. H. White, D. G. Cunningham, and M. C. Nowell, "An experimental and theoretical study of the offset launch technique for the enhancement of the bandwidth of multimode fiber links," *Journal of Lightwave Technology*, vol. 16, pp. 324–331, March 1998.
- [35] L. Raddatz, I. H. White, D. G. Cunningham, and M. C. Nowell, "Influence of restricted mode excitation on bandwidth of multimode fiber links," *IEEE Photon. Technol. Lett.*, vol. 10, pp. 534–536, April 1998.
- [36] M. Webster, L. Raddatz, I. H. White, and D. G. Cunningham, "A statistical analysis of conditioned launch for Gigabit Ethernet links using multimode fiber," *J. Lightwave Technol.*, vol. 17, pp. 1532–1541, Sept 1999.
- [37] G. Yabre, "Influence of core diameter on the 3-dB bandwidth of graded-index optical fibers," *J. Lightwave Technol.*, vol. 18, pp. 668–676, May 2000.
- [38] L. Raddatz, I. H. White, D. G. Cunningham, and M. C. Nowell, "Increasing the bandwidth-distance product of multimode fibre using offset launch," *Electron. Lett.*, vol. 33, pp. 232–233, 30 Jan 1997.
- [39] IEEE 802.3z, "Physical medium dependent (PMD) sublayer and baseband medium type 1000BASE-LX (long wavelength laser) and 1000BASE-SX (short wavelength laser clause 38)," 1998.
- [40] G. Yabre, "Comprehensive theory of dispersion in graded-index optical fibers," *J. Lightwave Technol.*, vol. 18, pp. 166–177, Feb 2000.
- [41] J. A. Buck, *Fundamentals of Optical Fibers*, John Wiley & Sons, 1995.
- [42] J. A. Arnaud, "Numerical evaluation of the impulse response of multimode optical fibers," *Fiber and Integrated Optics*, vol. 1, pp. 77–100, 1977.
- [43] J. E. Midwinter, *Optical Fibers for Transmission*, John Wiley & Sons, 1979.
- [44] J. C. Maxwell, *A Treatise on Electricity and Magnetism*, Dover, 1954.
- [45] C. Pollock, *Fundamentals of Optoelectronics*, Irwin, 1995.
- [46] D. Gloge, "Propagation effects in optical fiber," *IEEE Trans. Microwave Theory Tech.*, vol. 23, pp. 106–120, Jan 1975.
- [47] J. P. Gordon, "Optics of general guiding media," *Bell Sys. Tech. J.*, vol. 46, pp. 321, 1966.
- [48] Honeywell Inc., "Datasheet: HFE4092-341 850nm VCSEL," 2003.
- [49] Catalog PI359, "50/125 multimode fiber product information," July 2004.

- [50] D. Marcuse, *Theory of Dielectric Optical Waveguides*, Academic Press, 1991.
- [51] F. Tong, D. T. McInturff, Y. H. Kwark, S. E. Ralph, G. D. Pettit, and P. C. Wong, "Performance of $\text{In}_{0.47}\text{Ga}_{0.53}\text{As}$ metal-semiconductor-metal hybrid receiver at $1.55\ \mu\text{m}$," *Optical and Quantum Electronics*, vol. 25, pp. 699–703, Oct 1993.
- [52] S. E. Ralph, M. Hargis, and G. D. Pettit, "Large area, low voltage transit time limited InGaAs metal semiconductor metal photodetectors," *Appl. Phys. Lett.*, vol. 61, pp. 2222–2224, Nov 1992.
- [53] A. Yariv, *Optical electronics in modern communications*, Oxford University Press, 5th edition, 1997.
- [54] F. Tong, D. T. McInturff, S. E. Ralph, G. D. Pettit, and C. S. Li, "Performance of $\text{In}_{0.47}\text{Ga}_{0.53}\text{As}$ metal-semiconductor-metal photodetectors at $1.55\ \mu\text{m}$," in *Proc. LEOS 1992*, 1992, pp. 706–707.
- [55] W. Gao, P. R. Berger, G. J. Zyzdik, H. M. O'Bryan, D. L. Sivco, and A. Y. Cho, "In_{0.47}Ga_{0.53}As MSM photodiodes with transparent CTO schottky contacts and digital superlattice grading," *IEEE Transactions on Electron Devices*, vol. 44, pp. 2174–2179, Dec 1997.
- [56] O. Vendier, N. M. Jokerst, and R. P. Leavitt, "High efficiency thin-film GaAs-based MSM photodetectors," *Electron. Lett.*, vol. 32, pp. 394–395, 15 Feb 1996.
- [57] J. T. Verdeyen, *Laser Electronics*, Prentice Hall, 1995.
- [58] R. Dandliker, A. Bertholds, and F. Maysre, "How modal noise in multimode fibers depends on source spectrum, fiber dispersion," *J. Lightwave Technol.*, vol. LT-3, pp. 6–12, Feb 1985.
- [59] K. H. Hahn, M. R. Tan, Y.M. Hound, and S. Y. Wang, "Large area multitransverse-mode VCSELs for modal noise reduction in multimode fibre systems," *Electron. Lett.*, vol. 29, pp. 1482–1483, Aug 1993.
- [60] K. H. Hahn, M. R. Tan, and S. Y. Wang, "Intensity noise of large area, vertical cavity surface emitting lasers in multimode optical fibre links," *Electron. Lett.*, vol. 30, pp. 139–140, Jan 1994.
- [61] D. G. Cunningham, M. C. Nowell, P. Dowd, L. Raddatz, and I. H. White, "Modal noise penalties for data communication links employing large area VCSELs," *Electron. Lett.*, vol. 31, pp. 2147–2148, Nov 1995.
- [62] D. M. Kuchta and C. J. Mahon, "Mode selective loss penalties in VCSEL optical fiber transmission links," *IEEE Photonics Technology Letters*, vol. 6, pp. 288–290, Feb 1994.
- [63] M. Imai and T. Asakura, "Evaluation of the mode scrambler characteristics in terms of the speckle contrast," *Optics Comm.*, vol. 30, pp. 299–303, Sept 1979.
- [64] D. L. Franzen, G. W. Day, and R. L. Gallawa, "Standardizing test conditions for characterizing fibers," *Laser Focus*, vol. 17, pp. 103–105, Aug 1981.

- [65] Y. Koyamada and K. Yamashita, "Launching condition dependence of graded-index multimode fiber loss and bandwidth," *J. Lightwave Technol.*, vol. 6, pp. 1866–1871, Dec 1988.
- [66] M. Ikeda, "Basic properties of transmission characteristics in multimode optical fibers," *Review of the Electrical Communication Laboratories*, vol. 26, pp. 484–499, March-April 1978.
- [67] White paper: Corning WP4062, "Characterizing multimode fiber bandwidth for Gigabit Ethernet applications," 1999.
- [68] White paper: Corning MM19, "Measurement method: Modal bandwidth," 1999.
- [69] ANSI/TIA/EIA-455-204-2000 FOTP-204, "Measurement of bandwidth on multimode fiber," 2000.
- [70] W. F. Love, "Novel mode scrambler for use in optical-fiber bandwidth measurements," in *Proc. OFC 1979*, 1979, vol. Optical Fiber Communication, 1979.
- [71] G. D. Forney, "The Viterbi algorithm," *Proc. of the IEEE*, vol. 61, pp. 268–278, March 1973.
- [72] C. Argon, K. M. Patel, S. W. McLaughlin, and S. E. Ralph, "Spatially resolved equalization and decision feedback equalization for multimode fiber links," in *LEOS Summer Topical Meetings 2002 Tech. Digest*, 2002, pp. TuB3–1–TuB3–2.
- [73] S. E. Ralph, K. M. Patel, C. Argon, A. Polley, and S. W. McLaughlin, "Intelligent receivers for multimode fiber: optical and electronic equalization of differential modal delay," in *Proc. LEOS 2002*, 2002, vol. 1, pp. 295–296.
- [74] C. Argon, K. M. Patel, S. W. McLaughlin, and S. E. Ralph, "Spatially resolved equalization and forward error correction for multimode fiber links," in *Proc. ICC 2002*, 2002, vol. 3, pp. 1726–1730.
- [75] C. Argon, K. M. Patel, S. W. McLaughlin, and S. E. Ralph, "Exploiting diversity in multimode fiber communications links via multisegment detectors and equalization," *IEEE Communications Letters*, vol. 7, pp. 400–402, Aug 2003.
- [76] IEEE 802.3z, , " <http://grouper.ieee.org/groups/802/3/z/mbi/fieldstst.exe>, July 2004.
- [77] S. B. Wicker, *Error Control Systems for Digital Communication and Storage*, Prentice Hall, 1995.
- [78] O. Aitsab, "FEC techniques in submarine transmission systems," in *Proc. OFC 2001*, 2001, pp. TuF1–1–TuF1–3.
- [79] R. M. Pyndiah, "Near-optimum decoding of product codes: Block turbo codes," *IEEE Trans. Commun.*, vol. 46, pp. 1003–1010, Aug 1998.
- [80] C. Berrou and A. Glavieux, "Near optimum error correcting coding, decoding: Turbo-Codes," *IEEE Trans. Commun.*, vol. 44, pp. 1261–1271, Oct 1996.
- [81] C. E. Shannon and W. Weaver, *The Mathematical Theory of Communications*, Univ. Illinois Press, 1949.

- [82] W. Behm and N. J. Fliege, "A new suboptimum Viterbi receiver structure for digital communication systems," *European Transactions on Telecommunications*, vol. 6, pp. 311–319, May-June 1995.
- [83] T. Sakai, K. Kobayashi, S. Kubota, M. Morikura, and S. Kato, "Soft-decision Viterbi decoding with diversity combining for multi-beam mobile satellite communication systems," *IEEE Journal on Selected Areas in Communications*, vol. 13, pp. 285–290, Feb 1995.
- [84] H. L. Lou, "Implementing the Viterbi algorithm," *IEEE Signal Processing Magazine*, vol. 12, pp. 42–52, Sept 1995.
- [85] J. Burm and L.F. Eastman, "Low-frequency gain in MSM photodiodes due to charge accumulation and image force lowering," *IEEE Photon. Tech. Lett.*, vol. 8, no. 1, pp. 113–115, Jan 1996.
- [86] R.G. Decorby, R.I. MacDonald, M. Beaudoin, T. Pinnington, T. Tiedje, and Gouin F., "Elimination of low frequency gain in InAlAs/InGaAs metal-semiconductor-metal photodetectors by silicon nitride passivation," *Journal of Electronic Materials*, vol. 26, no. 12, pp. 125–127, 1997.

VITA

Ketan M. Patel was born in Pittsfield, Massachusetts in 1971. In 1993, he received a B.S. in electrical engineering from The University of Michigan in Ann Arbor. While at UM for his undergraduate degree, Ketan led the design, test and construction of the electrical, propulsion and telemetry systems on the Maize & Blue solar car team, which in 1993 very successfully raced in Sunrayce and the World Solar Challenge in Australia. In 1995, he received an M.S.E.E., also from The University of Michigan, specializing in optics and electromagnetics.

For the following three years, he worked in Dallas at Texas Instruments. While in the TI Defense and Systems Electronics Group GaAs facility (now TriQuint Semiconductor) he designed microwave integrated circuit (MMIC), which are currently being used for several communications systems including a various fiber optics and satellite systems. In 1998, Ketan came to the Georgia Institute of Technology to pursue his Ph.D. in E.E in the Ultrafast Optical Communications Group. His own research interests are in the integration of RF/microwave and optics components, including the development of spatially resolved detection for compensation of differential modal delay in multimode fiber links.

Ketan Patel is a member of the LEOS and MTT societies within the Institute of Electrical and Electronics Engineers. He is also a member of the Optical Society of America.